

# **Strain-phase relations in lead-free ferroelectric $K_xNa_{1-x}NbO_3$ epitaxial films for domain engineering**

vorgelegt von  
Master of Science  
Dorothee Braun  
geboren in Berlin

von der Fakultät II - Mathematik und Naturwissenschaften

der Technischen Universität Berlin

zur Erlangung des akademischen Grades

Doktor der Naturwissenschaften

Dr. rer. nat.

genehmigte Dissertation

Promotionsausschuss:

Vorsitzende: Prof. Dr. Marga Cornelia Lensen

Gutachter: Prof. Dr.-Ing. Matthias Bickermann

Gutachter: PD Dr. Martin Schmidbauer

Gutachter: Prof. Dr. Roger Wördenweber

Tag der wissenschaftlichen Aussprache: 17. Oktober 2017

Berlin 2017

---

---

## **Abstract**

The aim of this thesis is to demonstrate the potential of thin films for technical applications by tuning the ferroelectric film properties on the basis of the strain-phase diagram. For this purpose, a fundamental understanding of the relation between incorporated lattice strain by epitaxial growth of thin films and the evolution of ferroelectric phases has been pointed out. As an exemplary lead-free material, potassium sodium niobate ( $\text{K}_x\text{Na}_{1-x}\text{NbO}_3$ ) is considered. This material is of high technological interest due to its large coupling constant [1] and Curie temperature [2]. Furthermore, calculations predict the appearance of monoclinic phases under anisotropic epitaxial lattice strain [3]. They are attractive due to their inherent flexibility for the arrangement of the electrical polarization vector yielding e.g. huge piezoelectric responses [4] and flexible domain wall formation [5]. However so far, thin films have rarely been investigated and the influence of lattice strain on ferroelectric properties has not been studied systematically. In this work, thin films were grown by metal-organic chemical vapor deposition technique (MOCVD) on different oxide single-crystalline substrates.

For a targeted choice of appropriate film-substrate combinations, theoretical considerations with regard to film orientation and phase symmetry are essential. To predict the energetically most favorable film unit cell orientation on a substrate, linear elasticity theory was used in this thesis. For engineering the domain structure, a misfit strain-misfit strain phase diagram was calculated for potassium niobate by means of the Landau-Ginzburg-Devonshire (LDG) theory with major accuracy compared to existing predictions [3]. The result manifests a diversity of different, mainly monoclinic phases for  $\text{KNbO}_3$ .

By means of the calculated misfit strain-phase diagram, particular  $\text{K}_x\text{Na}_{1-x}\text{NbO}_3$  compositions were epitaxially grown by MOCVD with nearly perfect structural ordering and stoichiometry. Use of different  $0.1^\circ$  off-oriented (001)  $\text{SrTiO}_3$ , (110)  $\text{DyScO}_3$ , (110)  $\text{TbScO}_3$ , (110)  $\text{GdScO}_3$  and (110)  $\text{NdScO}_3$  single-crystalline substrates provides an experimental verification of the calculated strain-phase diagram. This was realized for the first time for the promising  $\text{K}_x\text{Na}_{1-x}\text{NbO}_3$  material system.

As a proof of concept, two different film-substrate combinations have been investigated in detail mainly with the piezoresponse force microscope (PFM). Together with elaborated x-ray diffraction measurements a detailed analysis of the ferroelectric domain structure inherently coupled to the crystal symmetry was possible. First,  $\text{K}_{0.75}\text{Na}_{0.25}\text{NbO}_3$  on  $\text{TbScO}_3$  with nearly uniaxial, medium compressive lattice strain

leads to periodically ordered, monoclinic  $M_A$  stripe domains. A second  $90^\circ$  rotated variant occurs only to a minor fraction which is attributed to the small strain energy density difference of both  $(001)_{pc}$  orientations. Second,  $K_{0.90}Na_{0.10}NbO_3$  deposited on  $NdScO_3$  displays a combination with degenerated strain energy densities for the  $(100)_{pc}$  and  $(001)_{pc}$  orientation. The result is a nested ferroelectric herringbone pattern with alternating, monoclinic  $a_1a_2/M_c$  domains. The longitudinal piezoelectric coefficient  $d'_{33}$  was locally determined in the system  $K_{0.90}Na_{0.10}NbO_3/SrRuO_3/NdScO_3$  to  $d'_{33} = 29 \frac{pm}{V}$  which is promising in comparison to established lead-based ferroelectrics [[6], [7], [8], [9], [10]]. Moreover, the domain wall inclination angle differs significantly from those of other symmetries and was discussed as a function of potassium concentration  $x$  in the framework of a model established by Bokov and Ye [5] yielding a first experimental proof. Furthermore, the composition  $x = 0.90$  on  $NdScO_3$  enabled the first investigation of the hierarchy and scaling behavior of complex, monoclinic multi-rank pattern.

## Zusammenfassung

Das Ziel dieser Arbeit ist das Potential dünner Filme für technische Anwendungen zu zeigen, wenn deren ferroelektrische Eigenschaften auf der Grundlage eines Verspannungs-Phasen Diagrammes gezielt eingestellt wurden. Zu diesem Zweck muss ein grundlegendes Verständnis für die Beziehung von eingebrachter Gitterverspannung mittels epitaktischem Wachstum dünner Filme und der Entstehung ferroelektrischer Phasen gewonnen werden. Als beispielhaftes bleifreies Material wurden Kaliumnatriumniobat ( $K_xNa_{1-x}NbO_3$ ) betrachtet. Dieses ist von großer technologischer Relevanz auf Grund seiner hohen Kopplungskonstante [1] und Curietemperatur [2].

Zudem sagen theoretische Betrachtungen unter anisotroper Gitterverspannung das Auftreten monokliner Phasen für epitaktische Filme vorher [3]. Diese sind begehrt, da sie eine inhärente Flexibilität für die Ausrichtung des Polarisationsvektors besitzen, was zu sehr hohen piezoelektrischen Auslenkungen [4] und flexibler Ausrichtung von Domänenwänden [5] führen kann. Jedoch wurden dünne Kaliumnatriumniobatfilme bisher wenig untersucht und ebenso wenig der Einfluss von Gitterverspannung auf die ferroelektrischen Eigenschaften. In der vorliegenden Arbeit wurden Dünnschichten mittels metallorganischer Gasphasendeposition (MOCVD) auf verschiedenen einkristallinen Oxidsubstraten abgeschieden.

Für eine zielgerichtete Wahl interessanter Substrat-Filmzusammensetzungen bedarf es theoretischer Betrachtungen zur Filmorientierung und Phasensymmetrie. Zur Vorhersage der energetisch günstigsten Orientierung der Filmeinheit zelle auf einem Substrat wurde die lineare Elastizitätstheorie in dieser Arbeit angewandt. Zum Zweck des "domain engineering", wurde ein Verspannungs-Phasen Diagramm für Kaliumniobat auf der Grundlage der Landau-Ginzburg-Devonshire-Theorie mit höherer Genauigkeit als bereits existierende Daten [3] berechnet. Das Ergebnis bestätigt eine Vielzahl verschiedener, hauptsächlich monokliner Domänenarten für  $KNbO_3$ .

Auf der Basis dieser Berechnungen wurden zielgerichtet  $K_xNa_{1-x}NbO_3$  Zusammensetzungen epitaktisch mittels MOCVD gewachsen. Die Verwendung verschiedener  $0.1^\circ$  fehlorientierter (001)  $SrTiO_3$ , (110)  $DyScO_3$ , (110)  $TbScO_3$ , (110)  $GdScO_3$  und (110)  $NdScO_3$  Substrate ermöglicht die experimentelle Überprüfung der theoretischen Ergebnisse. Diese Untersuchung wurde erstmals für das vielversprechende  $K_xNa_{1-x}NbO_3$ -System durchgeführt.

Um die Gültigkeit des Phasendiagramms zu testen, wurden im Detail zwei Film-Substratkombinationen mit dem Piezoresponse Force Mikroskop untersucht. Zusam-

men mit komplexen Röntgenbeugungsexperimenten war so eine detaillierte Analyse der ferroelektrischen Domänenstruktur als Folge der Kristallstruktur möglich. Im ersten Beispiel werden  $\text{K}_{0.75}\text{Na}_{0.25}\text{NbO}_3$  Filme auf  $\text{TbScO}_3$  mit nahezu uniaxialer, mittlerer kompressiver Gitterverspannung gezeigt, die periodisch angeordnete, monokline  $M_A$  Streifendomänen aufweisen. Eine zweite, um  $90^\circ$  rotierte Variante tritt mit geringerer Häufigkeit auf, was auf den eher geringen Verspannungsenergiedichteunterschied beider  $(001)_{\text{pc}}$  Orientierungen zurückgeführt werden kann. Das zweiten Beispiel,  $\text{K}_{0.90}\text{Na}_{0.10}\text{NbO}_3$  auf  $\text{NdScO}_3$ , zeigt eine Kombination entarteter Energiedichten beider pseudokubischen Orientierungen. Das Ergebnis ist ein verschachteltes, ferroelektrisches Fischgrätenmuster aus alternierend angeordneten, monoklinen  $a_1a_2/M_c$  Domänen. Der longitudinale piezoelektrische Koeffizient  $d'_{33}$  wurde lokal im Schichtsystem  $\text{K}_{0.90}\text{Na}_{0.10}\text{NbO}_3/\text{SrRuO}_3/\text{NdScO}_3$  zu  $d'_{33} = 29 \frac{\text{pm}}{\text{V}}$  bestimmt. Dieses Ergebnis ist vielversprechend im Vergleich zu existierenden bleibasierten Ferroelektrika [[6], [7], [8], [9], [10]]. Darüber hinaus unterscheidet sich der Neigungswinkel der Domänenwände signifikant vom dem anderer Symmetrien und wurde erstmals experimentell als Funktion des Kaliumgehaltes  $x$  im Rahmen des Modelles von Bokov und Ye [5] diskutiert. Abschließend wurden zum ersten Mal die Domänenhierarchie sowie das Skalierungsverhalten dieser komplexen, monoklinen Fischgrätenmuster untersucht.

## Publications in international refereed journals

1. D. Braun, M. Schmidbauer, M. Hanke and J. Schwarzkopf, "Hierarchy and scaling behaviour of ferroelectric multi-rank domain patterns in strained  $\text{K}_{0.9}\text{Na}_{0.1}\text{NbO}_3$  epitaxial films", submitted to *Nanotechnology*, 2017
2. D. Braun, M. Schmidbauer, M. Hanke, A. Kwasniewski and J. Schwarzkopf, "Tunable ferroelectric domain wall alignment in strained monoclinic  $\text{K}_x\text{Na}_{1-x}\text{NbO}_3$  epitaxial films", *Appl. Phys. Lett.* **110**, 232903 (2017)
3. J. Schwarzkopf, D. Braun, M. Hanke, R. Uecker and M. Schmidbauer, "Strain engineering of ferroelectric domains in  $\text{K}_x\text{Na}_{1-x}\text{NbO}_3$  epitaxial layers", *Frontiers* **4**, 26 (2017)
4. M. Schmidbauer, D. Braun, T. Markurt, M. Hanke, and J. Schwarzkopf, "Strain Engineering of Monoclinic Domains in  $\text{K}_x\text{Na}_{1-x}\text{NbO}_3$  Epitaxial Layers: A Pathway to Enhanced Piezoelectric Properties", *Nanotechnology* **28**, 24LT02 (2017)
5. M. Schmidbauer, M. Hanke, A. Kwasniewski, D. Braun, L. von Helden, Ch. Feldt, S. J. Leake and J. Schwarzkopf, "Scanning X-Ray Nanodiffraction from Ferroelectric Domains in Strained  $\text{K}_{0.75}\text{Na}_{0.25}\text{NbO}_3$  Epitaxial Films Grown on (110)  $\text{TbScO}_3$ ", *J. Appl. Cryst.* **50**, 519 – 524 (2017).
6. B. Cai, J. Schwarzkopf, E. Hollmann, D. Braun, M. Schmidbauer, T. Grellmann, and R. Wördenweber, "Electronic characterization of polar nanoregions in relaxor-type ferroelectric  $\text{NaNbO}_3$  films", *Phys. Rev. B* **93**, 224107 (2016)
7. J. Schwarzkopf, D. Braun, M. Hanke, A. Kwasniewski, J. Sellmann and M. Schmidbauer, "Monoclinic  $M_A$  domains in anisotropically strained ferroelectric  $\text{K}_{0.75}\text{Na}_{0.25}\text{NbO}_3$  films on (110)  $\text{TbScO}_3$  grown by MOCVD", *J. Appl. Cryst.* **49**, 375–384 (2016).
8. J. Schwarzkopf, D. Braun, M. Schmidbauer, A. Duk, and R. Wördenweber, "Ferroelectric domain structure of anisotropically strained  $\text{NaNbO}_3$  epitaxial thin films", *J. Appl. Phys.* **115**, 204105 (2014)
9. M. Schmidbauer, J. Sellmann, D. Braun, A. Kwasniewski, A. Duk, and J. Schwarzkopf, "Ferroelectric domain structure of  $\text{NaNbO}_3$  epitaxial thin films grown on (110)  $\text{DyScO}_3$  substrates", *Phys. Stat. Sol. RRL* **8**, 522 – 526 (2014)

10. J. Sellmann, J. Schwarzkopf, A. Kwasniewski, M. Schmidbauer, D. Braun and A. Duk, "Strained ferroelectric NaNbO<sub>3</sub> thin films: Impact of pulsed laser deposition growth conditions on structural properties", *Thin Solid Films* **570**, 107-113 (2014)

## Conference presentations

1. D. Braun, M. Schmidbauer, M. Hanke, C. Feldt and J. Schwarzkopf, "Coexistence of monoclinic domains in K<sub>x</sub>Na<sub>1-x</sub>NbO<sub>3</sub> on NdScO<sub>3</sub> grown by MOCVD", (oral), Joint IEEE International Symposium on the Applications of Ferroelectrics, European Conference on Applications of Polar Dielectrics & Workshop on Piezoresponse Force Microscopy (ISAF/ECAPD/PFM), Darmstadt, Germany, August 22-25, 2016
2. D. Braun, M. Schmidbauer, M. Hanke, C. Feldt and J. Schwarzkopf, "Alternating monoclinic domains in K<sub>0.9</sub>Na<sub>0.1</sub>NbO<sub>3</sub> thin films grown on NdScO<sub>3</sub> by MOCVD", (poster), Joint IEEE International Symposium on the Applications of Ferroelectrics, European Conference on Applications of Polar Dielectrics & Workshop on Piezoresponse Force Microscopy (ISAF/ECAPD/PFM), Darmstadt, Germany, August 22-25, 2016
3. D. Braun, M. Schmidbauer, A. Kwasniewski, P. Müller, J. Sellmann, M. Hanke, H. Renevier, and J. Schwarzkopf, "Formation and switching behavior of monoclinic domains in strained K<sub>0.90</sub>Na<sub>0.10</sub>NbO<sub>3</sub> epitaxial thin films on NdScO<sub>3</sub>", (oral), 13<sup>th</sup> European Meeting on Ferroelectricity (EMF), Porto, Portugal, June 28 - July 3, 2015
4. D. Braun, M. Schmidbauer, P. Müller and J. Schwarzkopf, "Domain structure in anisotropically strained K<sub>0.75</sub>Na<sub>0.25</sub>NbO<sub>3</sub> thin films on TbScO<sub>3</sub>", (oral), Deutsche Physikalische Gesellschaft (DPG), Frühjahrstagung, Berlin, Germany, March 15-20, 2015

# Contents

<b>Abstract</b>	<b>i</b>
<b>List of Abbreviations</b>	<b>ix</b>
<b>Introduction</b>	<b>1</b>
<b>I. Ferroelectricity &amp; Materials</b>	<b>5</b>
<b>1. Fundamentals of Piezo- and Ferroelectrics</b>	<b>5</b>
1.1. Crystal symmetry . . . . .	5
1.2. Phase transitions . . . . .	6
1.3. Ferroelectric domains . . . . .	8
1.4. Ferroelectric switching . . . . .	10
1.5. Piezoelectric coefficient . . . . .	12
<b>2. Ferroelectric thin films</b>	<b>14</b>
2.1. Perovskite structure . . . . .	14
2.2. Introduction to Linear elasticity theory . . . . .	15
2.3. Strain engineering in perovskite materials . . . . .	16
2.4. Potassium sodium niobate $K_xNa_{1-x}NbO_3$ . . . . .	20
2.5. Enhancement of piezoelectric responses . . . . .	22
<b>II. Growth &amp; Characterization methods</b>	<b>27</b>
<b>3. Thin film deposition</b>	<b>27</b>
<b>4. Atomic Force Microscopy</b>	<b>28</b>
<b>5. Piezoresponse Force Microscopy</b>	<b>30</b>
5.1. Contributions of a PFM signal . . . . .	32
5.2. Experimentally influencing the PFM signal . . . . .	34
5.3. Resonance enhancement of PFM signal . . . . .	36
5.4. Evaluation of the local piezoelectric coefficient $d'_{33}$ . . . . .	37

<b>6. X-ray diffraction</b>	<b>39</b>
6.1. High-resolution x-ray diffraction (HRXRD) . . . . .	39
6.2. Grazing incidence x-ray diffraction (GIXD) . . . . .	42
<b>III. Results &amp; Discussion</b>	<b>44</b>
<b>7. Theoretical Considerations</b>	<b>44</b>
7.1. Calculating lattice parameter from Vegard's law . . . . .	44
7.2. Calculation of the strain energy density $F(\varepsilon)(x)$ . . . . .	45
7.3. Calculation of the strained vertical lattice parameter $d_{\perp}^{\text{strained}}$ . . . . .	46
7.4. Calculation of the misfit strain-misfit strain phase diagram for $\text{KNbO}_3$	47
<b>8. Uniaxial strain: <math>\text{K}_{0.75}\text{Na}_{0.25}\text{NbO}_3</math> films on (110) <math>\text{TbScO}_3</math></b>	<b>51</b>
<b>9. Energy density degeneration for <math>(100)_{\text{pc}}</math> and <math>(001)_{\text{pc}}</math> orientation: <math>\text{K}_{0.90}\text{Na}_{0.10}\text{NbO}_3</math> films on (110) <math>\text{NdScO}_3</math></b>	<b>64</b>
<b>10. Tunable ferroelectric domain wall alignment in monoclinic systems</b>	<b>80</b>
<b>11. Hierarchy and scaling behavior of herringbone domain patterns in strained <math>\text{K}_{0.90}\text{Na}_{0.10}\text{NbO}_3</math> ferroelectric epitaxial films</b>	<b>86</b>
<b>IV. Summary</b>	<b>96</b>
<b>V. Outlook</b>	<b>98</b>
<b>References</b>	<b>99</b>
<b>Acknowledgement</b>	<b>113</b>
<b>Selbstständigkeitserklärung</b>	<b>115</b>

## List of Abbreviations

<b>1D</b>	One Dimensional
<b>2D-FFT</b>	Two Dimensional Fast Fourier Transformation
<b>ac</b>	Alternating Current
<b>AFM</b>	Atomic Force Microscopy
<b>c</b>	Cubic
<b>DART</b>	Dual AC Resonance Tracking
<b>dc</b>	Direct Current
<b>DHO</b>	Damped Harmonic Oscillator
<b>DRAM</b>	Dynamic Random Access Memory
<b>ESRF</b>	European Synchrotron Radiation Facility
<b>FeRAM</b>	Ferroelectric Random Access Memory
<b>GIXD</b>	Grazing Incidence X-Ray Diffraction
<b>(hkl)</b>	Miller Indices
<b>HRXRD</b>	High Resolution X-Ray Diffraction
<b>InvOLS</b>	Inverse Optical Lever Sensibility
<b>LPFM</b>	Lateral Piezoresponse Force Microscopy
<b>MOCVD</b>	Metal Organic Chemical Vapor Deposition
<b>MPB</b>	Morphotropic Phase Boundary
<b>NSO</b>	Neodymium Scandate
<b>o</b>	Orthorhombic
<b>pc</b>	Pseudocubic
<b>PFM</b>	Piezoresponse Force Microscopy
<b>PLD</b>	Pulsed Laser Deposition
<b>PR</b>	Piezoresponse
<b>PSD</b>	Position Sensitive (Photo-)Detector
<b>PZT</b>	Lead Zirconium Titanate
<b>RSM</b>	Reciprocal Space Map
<b>SEM</b>	Scanning Electron Microscopy
<b>STEM</b>	Scanning Transmission Electron Microscopy
<b>TEM</b>	Transmission Electron Microscopy
<b>TSO</b>	Terbium Scandate
<b>VPFM</b>	Vertical Piezoresponse Force Microscopy
<b>XRD</b>	X-ray Diffraction

## Introduction

In times of a technological revolution where applications can be tailor-made for every single part in daily life, functional materials are needed in huge quantity and perfect quality. Consequently, in the past two decades major effort was put into the research on materials with piezo - and ferroelectric properties and their defect-free synthesis [11]. Oxides with perovskite-like structure represents a class of materials with huge variety of possible compositions yielding a multitude of functional properties ranging from di-, piezo- and ferroelectric to optical or even multiferroics. As a result, they can apply for e.g. in non-volatile memory applications (FeRAM), as high-k materials in random-access memory devices (DRAM) or as optical waveguides to name only a few [[12],[13]]. Yet, most commonly used for such applications are lead-based materials due to their outstanding electric properties combined with excellent coupling coefficients [14]. However, they suffer from degradation and fatigue effects limiting the life time that seem not to be overcome [[15],[16]]. An additional problem is the toxic effect of lead itself [17]. Since it poses a serious environmental hazard, the European Union has restricted the use of lead (ratified 2003) in electronic devices. However, the search for alternative, lead-free materials that could compete with lead-based ferroics turns out to be difficult.

One promising lead-free alternative in this context is  $K_xNa_{1-x}NbO_3$ . In common to other alkaline-based oxides, potassium sodium niobate has been investigated as single crystal or as ceramic. Already in bulk form, the versatile and outstanding properties could be proved. However, the ongoing trend of device miniaturization requires the growth of high crystal quality thin films.

Additionally, the functional properties of thin layers can be tailored due to the incorporated lattice strain by epitaxial growth. Consequently, novel, artificial and enhanced features can be generated that differ significantly compared to their bulk counterparts. One focus point is thereby the introduction of a monoclinic symmetry because these phases have revealed protruding properties like giant piezoelectric responses when they were discovered at the morphotropic phase boundary (MPB) in lead zirconium titanate [[18],[19],[20]]. Theoretical predictions revealed the possibility to overcome the absence of such a MPB in many lead-free materials by using anisotropic lattice strain for the purpose of monoclinicity. This procedure to modify material's properties by applying epitaxial lattice strain is denoted as strain or domain engineering [21].

Mandatory for engineering the ferroelectric properties is a detailed understanding of

strain provoked phase changes and the evolving ferroelectric ordering. Because domains are formed in order to neutralize charge or to reduce lattice strain, they dictate the macroscopic and microscopic properties of a material. In particular, the domain wall periodicity scales with the film thickness yielding a much higher domain wall density in thin films compared to bulk crystals. Therefore, calculations are essential that reveal the strain-phase relationship for a distinct material system. Different approaches exist to describe a ferroelectric material as density-functional theory [22], time-dependent Ginzburg-Landau theory [23] or most commonly the modified Landau-Ginzburg-Devonshire theory [24]. In the framework of the latter, Bai and Ma calculated a strain-phase diagram for  $\text{KNbO}_3$  [3].

However, detailed investigations of the promising material system  $\text{K}_x\text{Na}_{1-x}\text{NbO}_3$  in thin film form are still missing. Especially, the approach to reveal structure-phase relationships in nearly perfect films grown by the industrial compatible metal-organic chemical vapor deposition technique (MOCVD) method is novel, since  $\text{K}_x\text{Na}_{1-x}\text{NbO}_3$  films are rarely studied yet. This method provides low defect concentrations and smooth and sharp interfaces, due to the growth close to the thermodynamic equilibrium, as well as uniform and homogeneous depositions on large scale. However, oxide film deposition by MOCVD is still challenging yet due to the stability and availability of suitable metal organic precursors.

For material research not only a sophisticated deposition techniques is necessary, rather also adequate characterization methods for thin film properties on a nanoscale are indispensable. In terms of thin film characterization, new methods for detecting local piezo- and ferroelectric properties on sub-micron scale are needed. Hereby, several properties are of special interest. The local piezoelectric responses have to be determined precisely. Likewise the ferroelectric domain structure as well as the local polarization switching behavior are mandatory to be investigated in terms of prospective application in high-density non-volatile memories. Several techniques at the nanoscale exist such as scanning electron microscopy (SEM), transmission electron microscopy (TEM) or various etching methods [[25],[26],[27]]. But most of these methods are either destructive, need sophisticated sample preparation or suffer from low lateral resolution. Indeed, non of them yield information about the local piezoelectric response or ferroelectric switching. Therefore, the upgrade of an atomic force microscope (AFM) with a piezoresponse force module (PFM) was the breakthrough in thin ferroelectric film research [28]. It has become the primary tool for imaging of domains and spectroscopy of piezo- and ferroelectric materials with high lateral resolution and without any spe-

cific sample preparation needed beforehand [[29],[30],[31],[32]].

Within the framework of this thesis, the liquid-delivery MOCVD technique was applied to grow high quality, ferroelectric  $K_xNa_{1-x}NbO_3$  epitaxial thin films on  $0.1^\circ$  off-oriented (001)  $SrTiO_3$ , (110)  $DyScO_3$ , (110)  $TbScO_3$ , (110)  $GdScO_3$  and (110)  $NdScO_3$  single-crystalline substrates. The aim was to get a fundamental understanding of the impact of anisotropic strain on ferroelectric domain formation. For that purpose, detailed PFM measurements were performed and correlated to structural data gained from elaborated XRD measurements. The experimental data agree with the predictions drawn from theoretical considerations of strain-phase relations and linear elasticity theory.

This thesis is divided into five parts.

**Part I** takes a look into the world of crystal symmetries and introduces their crucial impact on ferroelectric properties. Furthermore, the concept of strain engineering in perovskite thin films is described in general and how it is performed in particular for the case of potassium sodium niobate. Moreover, a brief discussion of how to enhance the piezoelectric response is given.

**Part II** explains the growth and characterization methods. The liquid delivery metal organic chemical vapor deposition technique is briefly illustrated. Since PFM represents the main characterization method, challenges and advantages of piezoresponse force microscopy are discussed in more detail. Moreover a basic introduction into x-ray diffraction is given.

**Part III** begins with theoretical considerations. As starting point, the linear elasticity theory is introduced to illustrate a theoretical concept for strain-dependent predictions of the energy density and thus the preferred film unit cell orientation. Moreover, a misfit strain - misfit strain phase diagram was calculated on the basis of Landau-Ginzburg-Devonshire theory for potassium niobate because the existing literature data [3] were calculated with insufficient increment. On the basis of this diagram, the impact of substrate stress on the structural properties of a lattice mismatched, thin film and thus on the ferroelectric phase is analyzed in detail for two selected examples. The experimental results for strained  $K_xNa_{1-x}NbO_3$  thin films grown by liquid-delivery MOCVD on (110)  $TbScO_3$  and (110)  $NdScO_3$  substrates are discussed and compared to the theoretical predictions. Furthermore, the dependence of the domain wall inclination angle from the

potassium concentration  $x$  was evaluated for the herringbone arrangement evolving for  $\text{K}_x\text{Na}_{1-x}\text{NbO}_3$  on  $\text{NdScO}_3$ . Eventually, the thickness dependent evolution of such a monoclinic herringbone pattern is described in the exemplary system  $\text{K}_{0.90}\text{Na}_{0.10}\text{NbO}_3$  on (110)  $\text{NdScO}_3$  revealing novel stable domain configurations and a multistage relaxation process.

**Part IV** summarizes the general conclusions of the experimental results.

**Part V** presents some ideas in form of an outlook for further work.

# Part I.

## Ferroelectricity & Materials

### 1. Fundamentals of Piezo- and Ferroelectrics

The basis of this thesis is an effect that has been observed by Pierre and Jacques Curie nearly 200 years ago in tourmaline crystals [33]. They showed that this material responds to a mechanical deformation with an accumulation of electric charges on the surface, whereby the amount is directly proportional to the applied stress. A few years later, also the reverse effect was discovered and was then named direct and indirect piezoelectric effect, respectively.

In 1920 J. Valasek demonstrated that Rochelle salt shows the same hysteresis behavior as it was known from ferromagnetics - but now under an electrical voltage applied [34]. As a result, this group of materials got the name ferroelectrics although they have nonessentially something to do with iron.

What should be shown later, these piezoelectric and ferroelectric properties are directly related to the crystal structure. Therefore, at this point a brief insight into the crystallography shall be given.

#### 1.1. Crystal symmetry

Based on symmetry considerations 32 crystallographic point groups can be distinguished that can not be further converted into each other by translation, mirroring or rotation [35]. The first classification can be made using the symmetry element of inversion. It turns out that eleven of 32 crystal groups have an inversion center and may be characterized as non-polar. Whereas the remaining 21 crystal classes have no centrosymmetry and are therefore referred to as polar. From the last group 20 lattices show a linear behavior between the applied electric voltage and mechanical deformation (or vice versa) and are therefore considered to be piezoelectric according to the experiments of the Curie brothers from 1880. Within the latter, one half exhibits a single, unique polar axis. This circumstance leads to the emergence of a temperature-dependent (in the absence of a mechanical stress) polarization in these crystals, referred as pyroelectric effect. In some of these materials, the polarization can moreover be switched reversibly by an applied external electric voltage between - at

least - two equilibrium states. This group is named ferroelectrics and is the lynchpin of this thesis.

## 1.2. Phase transitions

Behind the classification of materials into a symmetry class stands the dependence on intensive variables such as temperature and pressure, since the formation of a crystal lattice always obeys energetic boundary conditions.

The transformation of crystal lattices under the mentioned variables is known as phase transition according to Ehrenfest's theorem. Generally, the system is described by a thermodynamic potential  $G$ . Changing the environment parameters, the system reacts - either continuously or discontinuously - with a revised potential landscape and thus novel energy minima. The order of the phase transition is named after the level of the lowest derivative of  $G$  for a chosen intensive parameters for whom this transition expires discontinuously. Physically relevant are usually only phase transitions of 1<sup>st</sup> and 2<sup>nd</sup> order. The Landau theory is used here to differentiate. The key of this theory is to introduce an order parameter whose non-zero value characterizes the low temperature phase while it is zero in the high temperature phase [36]. Mathematically, it is based on a Taylor expansion of the Gibbs free energy  $G$  as a function of the order parameter. In the case of the paraelectric-to-ferroelectric phase transition, this order parameter is the polarization  $\mathbf{P}$ . Due to the fact that the ferroelectric phase is non-polar, the energy of a polarization and its opposite must be equal, so that the odd parameters must equal zero and drop out the equation [37].

$$\Delta G(P) = G_0 + \frac{a}{2} \frac{\partial^2 G}{\partial P^2} P^2 + \frac{b}{4} \frac{\partial^4 G}{\partial P^4} P^4 + \dots \quad (1)$$

Landau-Ginzburg-Devonshire relate the coefficients to ferroelectric properties through an expansion of the Taylor series to 6<sup>th</sup> order [38]:

$$\begin{aligned} \Delta G = & \alpha_1(P_1^2 + P_2^2 + P_3^2) + \alpha_{11}(P_1^4 + P_2^4 + P_3^4) + \alpha_{12}(P_1^2 P_2^2 + P_2^2 P_3^2 + P_3^2 P_1^2) \\ & + \alpha_{111}(P_1^6 + P_2^6 + P_3^6) + \alpha_{112}[P_1^4(P_2^2 + P_3^2) + P_2^4(P_1^2 + P_3^2) + P_3^4(P_2^2 + P_1^2)] \\ & + \alpha_{123}(P_1^2 P_2^2 P_3^2) - \frac{1}{2} s_{11}^D(\sigma_1^2 + \sigma_2^2 + \sigma_3^2) - s_{12}^D(\sigma_1 \sigma_2 + \sigma_2 \sigma_3 + \sigma_1 \sigma_3) \\ & - \frac{1}{2} s_{44}^D(\sigma_4^2 + \sigma_5^2 + \sigma_6^2) - E_1 P_1 - E_2 P_2 - E_3 P_3 \\ & - Q_{11}(\sigma_1 P_1^2 + \sigma_2 P_2^2 + \sigma_3 P_3^2) - Q_{12}[\sigma_1(P_2^2 + P_3^2) + \sigma_2(P_1^2 + P_3^2) + \sigma_3(P_2^2 + P_1^2)] \\ & - Q_{44}(\sigma_4 P_2 P_3 + \sigma_5 P_1 P_3 + \sigma_6 P_1 P_2) \end{aligned} \quad (2)$$

where  $\alpha$ 's are the dielectric stiffnesses,  $Q_{ij}$  the electrostrictive constants,  $s_{ij}^D$  the elastic compliances,  $\sigma_i$  the stress components,  $P_m$  is the polarization and  $E_m$  is the electric field.

In order to facilitate the understanding of eq. 2, the physical meaning of these coefficients shall be explained in more detail.

First, the dielectric stiffness displays the maximum electric field that a material can withstand without breaking down. Within the latter, bound electrons become free due to the incorporated energy of the electric field yielding conductive paths through the material.

The electrostrictive constant  $Q_{ij}$  describes the deformation of a dielectric material in dependence of the applied electric field. In contrast to the piezoelectric effect that reflects the linear mechanic response under an electric field,  $Q_{ij}$  considers only the part independent of the direction of the electric field and thus the part proportional to  $E^2$ . The third term, the elastic compliances  $s_{ij}^D$ , classify the resistance a material opposes its mechanical deformation. Hereby, only a reversible deformation is taken into account. Last, the stress tensor  $\sigma$  is a tensor of second rank, describing the mechanic deformation of material in reference to the initial ground state.

It should be noted that the tensors in eq. 2 and in the following are written in Voigt notation as exemplary shown in eq. 3.

$$[c_{\alpha\beta}]^V = \begin{pmatrix} c_{11} & c_{12} & c_{13} & c_{14} & c_{15} & c_{16} \\ c_{21} & c_{22} & c_{23} & c_{24} & c_{25} & c_{26} \\ c_{31} & c_{32} & c_{33} & c_{34} & c_{35} & c_{36} \\ c_{41} & c_{42} & c_{43} & c_{44} & c_{45} & c_{46} \\ c_{51} & c_{52} & c_{53} & c_{54} & c_{55} & c_{56} \\ c_{61} & c_{62} & c_{63} & c_{64} & c_{65} & c_{66} \end{pmatrix}^V := \begin{pmatrix} c_{1111} & c_{1122} & c_{1133} & c_{1123} & c_{1113} & c_{1112} \\ c_{2211} & c_{2222} & c_{2233} & c_{3311} & c_{2213} & c_{2212} \\ c_{3311} & c_{3322} & c_{3333} & c_{3311} & c_{3313} & c_{3312} \\ c_{2311} & c_{2322} & c_{2333} & c_{3311} & c_{2313} & c_{2312} \\ c_{1311} & c_{1322} & c_{1333} & c_{3311} & c_{1313} & c_{1312} \\ c_{1211} & c_{1222} & c_{1233} & c_{3311} & c_{1213} & c_{1212} \end{pmatrix} \quad (3)$$

When  $\Delta G$  is plotted as a function of the polarization, the temperature dependent minima can be extracted. As an example, I calculated the energy landscape of  $\text{Pb}(\text{Zr}_{0.40}\text{Ti}_{0.60})\text{O}_3$  at room temperature revealing only one stable phase which can be related to the tetragonal phases as illustrated in fig. 1.

To link these theoretical predictions to the experiment it can be described as followed: Phenomenologically, at a 1<sup>st</sup> order phase transition the polarization changes discontinuously or abruptly and the permittivity of the ferroelectric has a finite maximum in the intersection between the phases. In contrast, the phase transition of 2<sup>nd</sup>

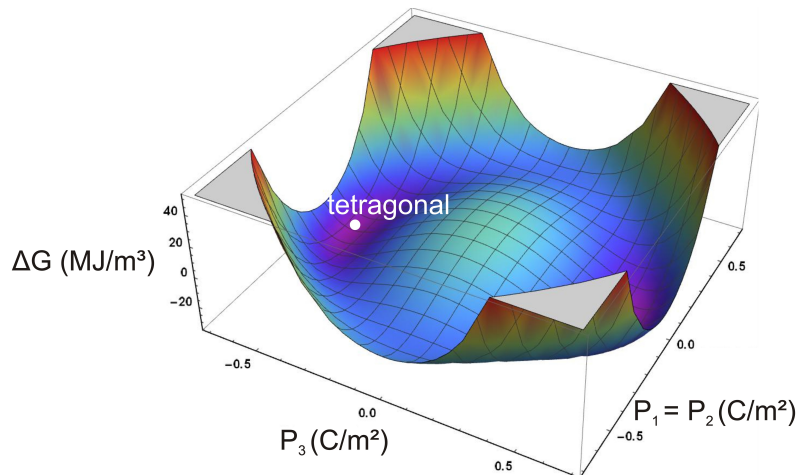


Figure 1: Gibbs free energy  $\Delta G$  plotted as a function of the polarization  $P_i$  for the tetragonal phase of  $\text{Pb}(\text{Zr}_{0.40}\text{Ti}_{0.60})\text{O}_3$  at room temperature. No strain or electric field is applied.

order is characterized by a continuous change in the polarization and a break of permittivity. Examples include  $\text{BaTiO}_3$  and  $\text{LiTiO}_3$  showing a 1<sup>st</sup> and 2<sup>nd</sup> order phase transition, respectively.

### 1.3. Ferroelectric domains

These transitions are usually accompanied by a structural transformation. Especially evident is this phenomenon for perovskites  $\text{ABO}_3$ , as they are studied in this work (for more details see chapter 2.1). An example to be discussed at this point is barium titanate. At high temperatures, the perovskite unit cell is arranged as a face-centered cubic one. The titanium ion forms the inversion center and is coordinated by eight barium ions in the cube corners and six oxygen ions in the cube faces. This phase is non-polar and is classified as paraelectric. If the temperature decreases, the system undergoes from a temperature  $T$  on, which is equal to the so-called Curie temperature  $T_c$  ( $T = T_c$ ), a structural transition with breaking the symmetry. The unit cell is slightly stretched in one direction and loses the former cubic symmetry under manifestation of a tetragonal structure. Consequently, the titanium ion is shifted from the central position and a local electric dipole moment develops. The entirety of these dipoles is referred to as crystal spontaneous polarization  $P_s$ .

With the formation of a spontaneous polarization the process has not been completed in terms of energy minimization. A uniform orientation of all local dipole moments would result in charged surfaces (and interfaces). Therefore, as a counter-force a depolarization field is formed. A balance of both forces is only able if the spontaneous

polarization is equally distributed. This process is called formation of ferroelectric domains.

In the case of the discussed barium titanate with its tetragonal structure below the Curie temperature two opposite polarization direction along the long axis may occur. This configuration is called  $180^\circ$  - or c-domains.

In other crystal classes, for example, in orthorhombic or rhombohedral lattices, the spontaneous polarization can be aligned along the two perpendicular in-plane lattice vectors, which is then described as  $90^\circ$  - or  $a_1$  (or  $a_2$ ) domains. Likewise a lateral domain is formed, when the polarization vector is along the in-plane face diagonal referred as  $a_1a_2$  formation. Moreover, ferroelectric phases appear that have both a vertical and a lateral polarization component. These inclined arrangements are known as  $a_1c$ ,  $a_2c$  and r domains.

Due to the fact, that the nomenclature arose from tetragonal systems, these domain types got sometimes different notations in other symmetries. For example, the latter ones are usually depicted as  $M_c$  and  $M_A$  phases in monoclinic crystals.

Basically, there are also cases in which different structures so-called multidomain arrangement as e.g. a/c pattern.

Additionally, in all these cases the urge for electrical neutrality has to be considered. This means that the cost of a separating domain wall is only efficient if two positive (or negative) charges are isolated. This boundary condition can be fulfilled when the electric polarization vectors are arranged in a "head-to-tail" configuration. This formation is illustrated for different domain structures in fig. 2.

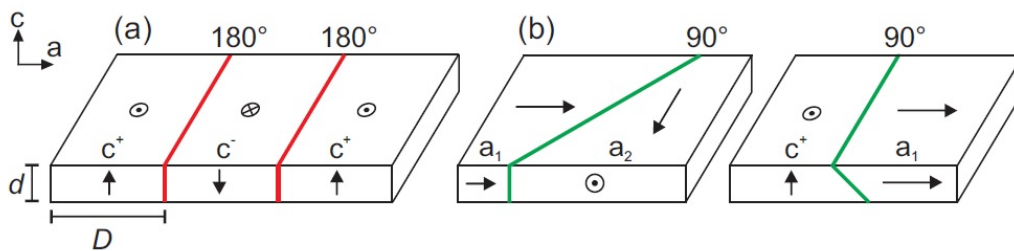


Figure 2: Schematic illustration of the domain wall formation by means of (a)  $180^\circ$  domain walls in e.g.  $c^+/c^-$  domain structures and (b)  $90^\circ$  walls in pure lateral  $a_1/a_2$  and alternating  $a/c$  domain structures in "head-to-tail" configuration ( $d$ : crystal thickness,  $D$ : domain width). Taken from [39].

The question which domain width screens effectively the charge and is economically to be build up can be answered only theoretically from energetic considerations. In order to solve the equations analytically, the configuration has to be restricted to two opposing domains.

On one side of the energy balance is the expenditure for the construction of the domain wall  $E_{\text{wall}}$ . On the other side stands the energy gain by minimizing the depolarization field  $E_{\text{field}}$ . The two opponents can be written as followed [40]:

$$E_{\text{wall}} = \frac{\sigma V}{D} \quad (4)$$

$$E_{\text{field}} = \frac{\varepsilon D V P_0^2}{t} \quad (5)$$

whereby  $\sigma$  is the energy of the domain wall per unit cell,  $D$  the domain width,  $P_0$  the polarization,  $\varepsilon$  is the dielectric constant of the material,  $V$  denote the crystal volume and  $t$  expresses the film thickness. Under equilibrium conditions,  $E_{\text{wall}} = E_{\text{field}}$  applies and in the following a description for the domain width  $D$  can be calculated [40]:

$$D = \sqrt{\left(\frac{t\sigma}{\varepsilon P_0^2}\right)} \quad (6)$$

This root dependency  $D \propto \sqrt{t}$  was former predicted by Kittel [41] for ferromagnets and could be confirmed experimentally.

In a real crystal structure, additional factors such as defects, tension or free charge carriers occur that will affect the domain formation (and thus the periodicity) and will moreover complicate the structure. As one example, herringbone pattern are discussed in detail in chapter 11.

## 1.4. Ferroelectric switching

The switching behavior of the electric polarization  $\mathbf{P}$  as a function of the applied electric field  $\mathbf{E}$  is shown schematically in fig. 3. First, the application of an electrical voltage leads to an alignment of the local dipoles along the electric field vector. Finally, all the dipoles are oriented and a saturation is reached. This condition is referred to as ferroelectric poling. The fascinating thing about ferroelectrics is that with decreasing of voltage, the initial state can never be achieved because some dipoles remain in their switched position. Thus, even when the applied electric field is zero a polarization is still measurable. This effect is called remnant polarization  $P_R$ . When the material-specific coercivity is reached, the distribution of dipoles is identical. The experimental

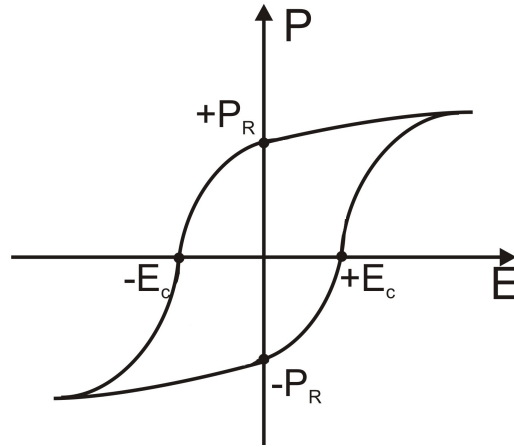


Figure 3: Polarization in dependence of the electric field for a ferroelectric material. A typical hysteresis shape develops for ideal ferroelectrics.

course in counter-rotating applied field looks the same and closes the curve in the P-E-diagram to a hysteresis.

What happens microscopically during this process in the crystal is shown in a model-like sequence in fig. 4. Based on an idealized monodomain state between a top and

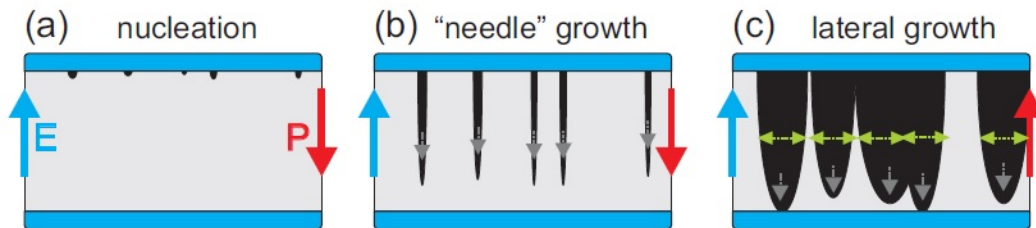


Figure 4: Ideal ferroelectric domain switching process in a sandwich structure shaped as electrode/ferroelectric/electrode structure. (a) First step is the nucleation of small domains with polarizations opposite to the surrounding material at the ferroelectric interface. (b) In the following, the domains grow needle-like towards the reverse electrode. (c) During the last step, the lateral domain expansion affiliates yielding complete reversion of the initial macroscopic polarization. Taken from [39].

a bottom electrode, applying an electric voltage leads to nucleation of domains with opposite polarization. Thereby, nucleation is preferred especially on defects due to the presence of kink positions. In the next step, the domains grow needle-like through the film to the mutual electrode. Due to the narrow lateral extension, the macroscopic polarization change is not significant. After reaching the backside of the crystal, the horizontal movement of the domain walls starts with rapid growth in lateral domain size. Finally, adjacent domains unite to a complete reversal of the crystal. This process

can take nanoseconds to microseconds for ferroelectric oxides.

## 1.5. Piezoelectric coefficient

A piezoelectric material can theoretically be distorted mechanically in all three dimensions  $x_i$  with  $i = 1, 2, 3$  by applying an electrical voltage. Since this is a multi-dimensional problem, the mathematical description of this process needs the use of tensor geometries. The charge density  $D_i$  as a result of stress  $\sigma_{jk}$  can be written as follows:

$$D_i = d_{ijk} \cdot \sigma_{jk} \quad (7)$$

where the indices  $i, j, k$  correspond to the three spatial directions.  $d_{ijk}$  is a third-rank tensor and reflects the system's symmetry reducing the unknown parameter immensely.

Furthermore, the tensor elements in Voigt notation are quite descriptive: if a voltage is applied perpendicular to the film in the  $z=3$ -direction and the mechanical stress in the same direction is of interest, the tensor entry  $d_{33}$  has to be calculated. That is exactly the situation later in the PFM experiment.

Since the coordinate system in the film does not have to match the laboratory system, in addition a coordinate transformation is necessary to evaluate the correct  $d'_{33}$ .

$$d'_{ijk} = A \cdot d_{ijk} \cdot N^T \quad (8)$$

The matrix  $A$  rotates the system along all three coordinate axes [6]:

$$A = \begin{pmatrix} a_{11} & a_{12} & a_{13} \\ a_{21} & a_{22} & a_{23} \\ a_{31} & a_{32} & a_{33} \end{pmatrix} \quad (9)$$

$$A = \begin{pmatrix} \cos \varphi \cos \phi - \cos \theta \sin \varphi \sin \phi & \cos \varphi \sin \phi + \cos \theta \sin \varphi \cos \phi & \sin \theta \sin \varphi \\ -\sin \varphi \cos \phi + \cos \theta \cos \varphi \sin \phi & -\sin \varphi \sin \phi + \cos \theta \cos \varphi \cos \phi & \cos \varphi \sin \theta \\ \sin \theta \sin \phi & -\sin \theta \cos \phi & \cos \theta \end{pmatrix} \quad (10)$$

and  $N^T$  is calculated from the matrix entries of  $A$  according to [42]:

$$N^T = \begin{pmatrix} a_{11}^2 & a_{21}^2 & a_{31}^2 & 2a_{21}a_{31} & 2a_{31}a_{11} & 2a_{11}a_{21} \\ a_{12}^2 & a_{22}^2 & a_{32}^2 & 2a_{22}a_{32} & 2a_{32}a_{12} & 2a_{12}a_{22} \\ a_{13}^2 & a_{23}^2 & a_{33}^2 & 2a_{23}a_{33} & 2a_{33}a_{13} & 2a_{13}a_{23} \\ a_{12}a_{13} & a_{22}a_{23} & a_{32}a_{33} & a_{22}a_{33} + a_{32}a_{23} & a_{12}a_{33} + a_{32}a_{13} & a_{22}a_{13} + a_{12}a_{23} \\ a_{13}a_{11} & a_{23}a_{21} & a_{33}a_{31} & a_{21}a_{33} + a_{31}a_{23} & a_{31}a_{13} + a_{11}a_{33} & a_{11}a_{23} + a_{21}a_{13} \\ a_{11}a_{12} & a_{21}a_{22} & a_{31}a_{32} & a_{21}a_{32} + a_{31}a_{22} & a_{31}a_{12} + a_{11}a_{32} & a_{11}a_{22} + a_{21}a_{12} \end{pmatrix}$$

In case of an orthorhombic symmetry, the coefficient  $d'_{33}$  can be estimated as follows:

$$d'_{33} = \cos \theta [\sin^2 \theta \sin^2 \phi^2 (d_{24} + d_{32}) + \sin^2 \theta \cos^2 \phi^2 (d_{15} + d_{31}) + d_{33} \cos^2 \theta] \quad (12)$$

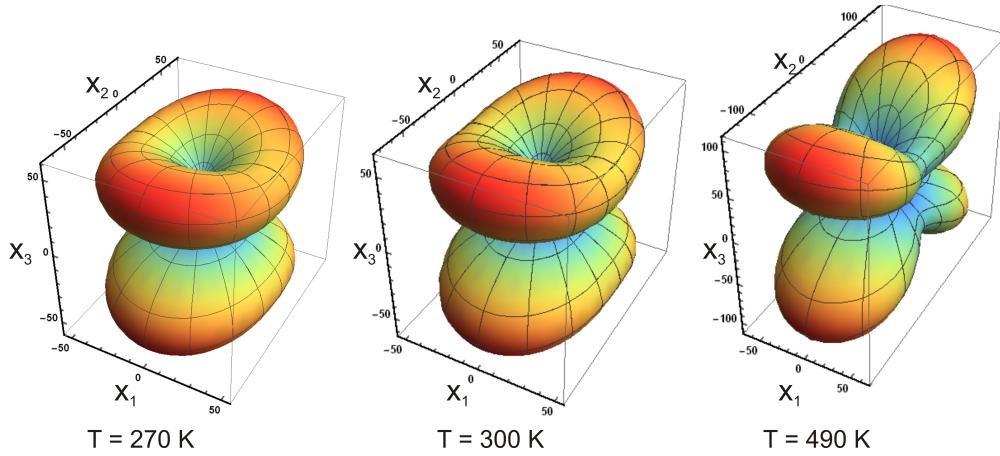


Figure 5: Angular dependency of the longitudinal piezoelectric coefficient  $d'_{33}$  for the orthorhombic  $\text{KNbO}_3$  crystal without any strain or electric field applied in a temperature range between  $T = 270 - 490$  K. Calculated on the basis of eq. 12 and the material constants taken from [38].

As a result from these calculations, the measured vertical piezoelectric coefficient  $d'_{33}$  is significantly influenced by shear components.

I plotted the angular and temperature-dependent  $d'_{33}$  for  $\text{KNbO}_3$  as depicted in fig. 5. Herefrom, the direction of the maximal response can directly be read. As a result, information can be gained if the maximal longitudinal response can be expected along the polar axis or tilted away in a non-polar direction.

The piezoelectric coefficients have the unit  $\frac{\text{m}}{\text{V}}$  and are therefore directly suitable for classifying the piezoelectric response in dependence of the applied field in the respective spatial direction.

## 2. Ferroelectric thin films

### 2.1. Perovskite structure

Perovskite is the name for  $\text{CaTiO}_3$ , denoted after the Russian mineralogist Lew Alexejewitsch Perowski. However, the structure is inherent in a wide range of oxides (e.g. all used compositions in this work). Consequently, perovskite became a generic term for oxides crystallizing in the general composition formula  $\text{ABO}_3$  structure with A and B being mono- to trivalent and tri- to pentavalent cations, respectively [43]. The ion formation within the unit cell can be schematically illustrated as shown in fig. 6.

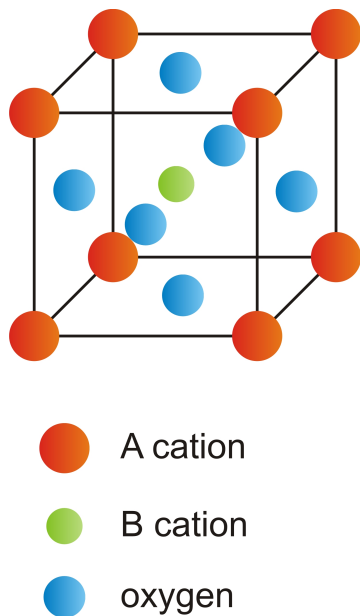


Figure 6: The perovskite unit cell for the general composition  $\text{ABO}_3$  in the case of a cubic symmetry.

Depending on chemical composition and external parameter as pressure and temperature, the crystal structure exhibits cubic, tetragonal, orthorhombic or rhombohedral symmetry. In reality, the distortion is limited and can be estimated by Goldschmidt's factor  $\kappa$  which constitutes a dimensionless quantity that describes the ratio of cation radii -  $r_A$  and  $r_B$  - to the anion radius  $r_O$  [44]:

$$\kappa = \frac{r_A + r_O}{\sqrt{2}(r_B + r_O)} \quad (13)$$

Hereby, the parameter  $\kappa$  can only take values between  $0.71 \leq \kappa \leq 1$  for a perovskite material [45]. For the crystal lattice, the changing Goldschmidt factor ultimately leads to a variation of the crystal symmetry from cubic to orthorhombic to rhombohedral.

The end member  $\kappa = 1$  means cubic structure as built in strontium titanate. However, fascinating regarding eq. 13 is that different physical properties like ferroelectricity or magnetism can arise depending on the material composition, but all perovskites have similar lattice parameters. This circumstance allows the sequential deposition of different perovskite materials without large lattice mismatch and eventually the combination of different functional layers.

## 2.2. Introduction to Linear elasticity theory

Under an external force, the atoms within the crystal lattice are displaced from their equilibrium position by the vector  $\mathbf{u}(\mathbf{r})$ . In order to determine the relationship between  $\mathbf{u}(\mathbf{r})$  and the elasticity tensor  $\varepsilon_{lm}$ , the displacement between two points within an infinitely small volume has to be considered. Mathematically, the position of two points shifted relatively to one another can be solved for each direction individually by means of a Taylor expansion [[46],[47]]. Due to the small volume under investigation, the calculation is truncated after the linear part. Consequently, the theory is named as "linear" elasticity theory.

Summarizing the distortion for the three dimensional, atomistic arrangement in tensor notation yields eq. 14:

$$\mathbf{u}(\mathbf{r}) = \begin{pmatrix} \frac{\partial u_x}{\partial x} & \frac{1}{2} \left( \frac{\partial u_x}{\partial y} + \frac{\partial u_y}{\partial x} \right) & \frac{1}{2} \left( \frac{\partial u_x}{\partial z} + \frac{\partial u_z}{\partial x} \right) \\ \frac{1}{2} \left( \frac{\partial u_y}{\partial x} + \frac{\partial u_x}{\partial y} \right) & \frac{\partial u_y}{\partial y} & \frac{1}{2} \left( \frac{\partial u_y}{\partial z} + \frac{\partial u_z}{\partial y} \right) \\ \frac{1}{2} \left( \frac{\partial u_z}{\partial x} + \frac{\partial u_x}{\partial z} \right) & \frac{1}{2} \left( \frac{\partial u_z}{\partial y} + \frac{\partial u_y}{\partial z} \right) & \frac{\partial u_z}{\partial z} \end{pmatrix} \begin{pmatrix} x \\ y \\ z \end{pmatrix} \quad (14)$$

$$\mathbf{u}(\mathbf{r}) = \begin{pmatrix} \varepsilon_{xx} & \varepsilon_{xy} & \varepsilon_{xz} \\ \varepsilon_{yx} & \varepsilon_{yy} & \varepsilon_{yz} \\ \varepsilon_{zx} & \varepsilon_{zy} & \varepsilon_{zz} \end{pmatrix} \mathbf{r} \quad (15)$$

Eqs. 14 and 15 describe the relationship between displacement  $u_i$  and strain  $\varepsilon_{lm}$ . As a result, the respective strain components can be written as follows:

$$\varepsilon_{lm} = \frac{1}{2} \left( \frac{\partial u_l}{\partial x_m} + \frac{\partial u_m}{\partial x_l} \right) \quad l, m = x, y, z = 1, 2, 3 \quad (16)$$

Experimentally, if the strain should be calculated for an epitaxial film along the substrate directions, thus for identical  $l = m$ , eq. 16 can be simplified. For the in-plane lattice parameter of the film  $a_{film}$  and substrate  $a_{substrate}$ , eq. 16 can be written as:

$$\varepsilon_{ll} = \frac{a_{substrate} - a_{film}}{a_{film}} \quad (17)$$

In conclusion, the application of an external force as e.g. epitaxial stress on a material leads to the displacement of the unit cell atoms from their equilibrium position. In consequence, the inherent symmetry of the material can be artificially modified. Essential for this symmetry transformation is the direction of the executed force. Hence, in the example of epitaxial growth the difference in lattice parameter and if relevant the discrepancy between substrate and film symmetry.

A special but important aspect is the application of anisotropic stress. This way, a lowering of the symmetry can be achieved which may enhance the piezoelectric properties as it should be presented in more detail in the following chapters.

### 2.3. Strain engineering in perovskite materials

During epitaxial growth, the film adapts first to the in-plane lattice parameter of the substrate. This process takes as long as the critical film thickness is not exceeded. The adoption of the "foreign" lattice parameter of the substrate stresses the lattice artificially. This process is schematically illustrated in fig. 7a for a perovskite unit cell without the oxygen ions for a better visibility of the strain effect.

As can be seen in fig. 7a, the incorporated strain can be either compressive or tensile nature. In the former one, the film lattice has to adopt onto smaller in-plane substrate lattice parameter compared to the initial film in-plane lattice values. In consequence, the film is elongated perpendicularly to the film-substrate interface.

In the case of tensile strain, the film lattice has to be stretched to fit onto the larger in-plane lattice parameter of the substrate yielding a parallel elongation of the unit cells in respect to the film-substrate interface.

In any case, the result is a distorted lattice structure that can undergo hereby a structural phase transition. In the case of perovskites, especially the  $\text{BO}_6$  octahedra are likely to be tilted which may lead to enormous changes in film properties such as Curie temperature or piezoelectric properties. In addition, properties which are not apparent for the bulk crystal can be introduced into thin films via lattice-mismatched growth. This process is called "strain engineering".

A popular example is the artificially introduced ferroelectricity in strained strontium titanate. The respective misfit strain-temperature phase diagram is illustrated in fig. 7b. In the unstressed case,  $\text{SrTiO}_3$  has a cubic symmetry at room temperature and thus a paraelectric behavior. But, if the material is grown heteroepitaxially on a substrate,

SrTiO<sub>3</sub> can be stressed this way that a paraelectric-to-ferroelectric phase transition is achieved as it is shown in fig. 7b.

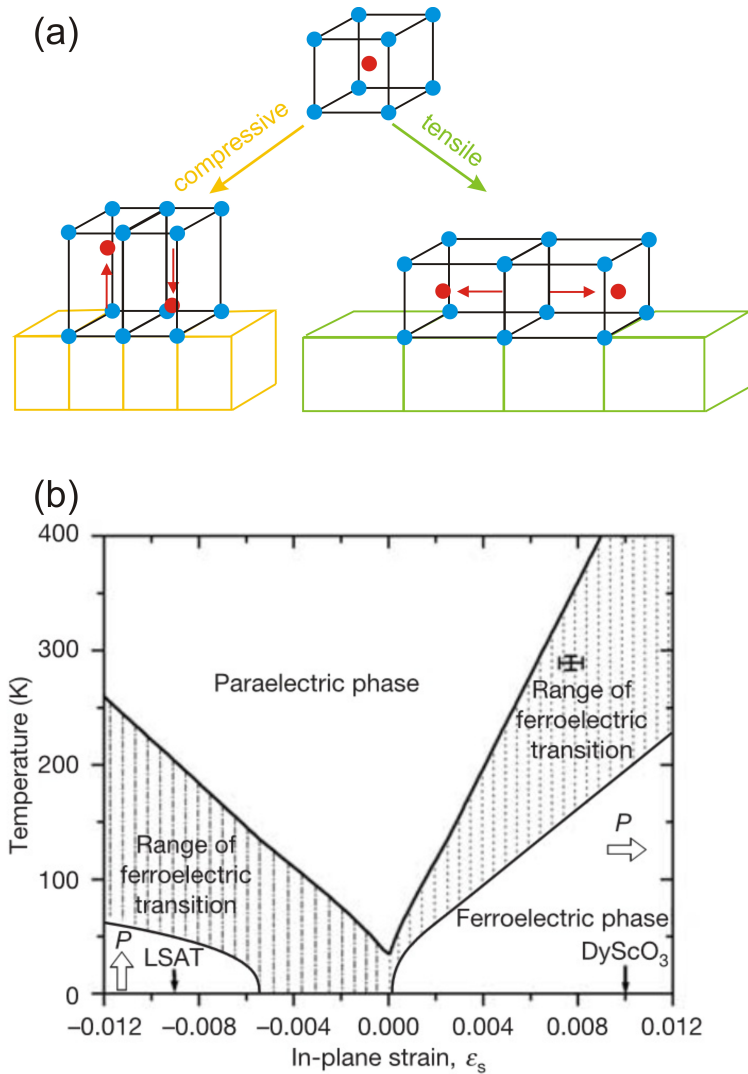


Figure 7: (a) Influence of lattice mismatched growth on a perovskite unit cell. For a better visibility of the strain effect, the perovskite unit cell is drawn without the oxygen ions. (b) Misfit strain-temperature phase diagram for SrTiO<sub>3</sub>. Taken from [48].

In the Leibniz Institute for Crystal Growth the unique possibility exists to have access to a huge variety of different substrate materials and thus in-plane lattice parameter. Most of them have orthorhombic symmetry. Due to the oftentimes huge orthorhombic unit cells, the calculation of appropriate substrate-film combinations is impeded. For that reason, usually a transfer into the pseudocubic notation is made to describe only one perovskite unit. In order to simplify the calculations, octahedral tilts are neglected. The conversion between orthorhombic "o" and pseudocubic "pc" lattice parameters is

executed in accordance to the equations of Vailionis [49]:

$$a_{pc} = \frac{c_o}{2} \quad (18)$$

$$b_{pc} = \frac{\sqrt{a_o^2 + b_o^2 - 2a_o b_o \cos \gamma_0}}{2} \quad (19)$$

$$c_{pc} = \sqrt{\frac{a_o^2 + b_o^2 - 2b_{pc}^2}{2}} \quad (20)$$

$$\alpha_{pc} = \arccos\left(\frac{b_{pc}^2 + c_{pc}^2 - a_o^2}{2b_{pc}c_{pc}}\right) \quad (21)$$

If  $\gamma_0 = 90^\circ$  is chosen, eqs. 18-21 can be simplified to:

$$a_{pc} = \frac{c_o}{2} \quad (22)$$

$$b_{pc} = \frac{\sqrt{a_o^2 + b_o^2}}{2} = c_{pc} \quad (23)$$

$$\alpha_{pc} = \arccos\left(1 - \frac{a_o^2}{2b_{pc}^2}\right) \quad (24)$$

Hereby, fig. 8 serves for a better illustration of the relationship between orthorhombic and pseudocubic notation.

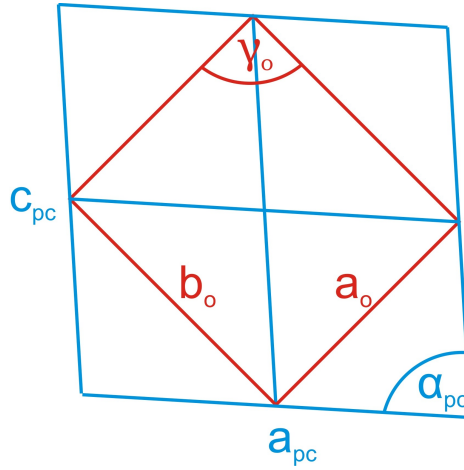


Figure 8: The relationship between orthorhombic and pseudocubic notation for the case of  $\gamma_0 = 90^\circ$ .

Due to the fact, that the orthorhombic lattice parameter are not equal ( $a_o \neq b_o$ ), the pseudocubic unit cell is actually monoclinically distorted. Therefore, the angle  $\alpha_{pc}$  corresponds to the monoclinic distortion angle  $\beta$  via:

$$\beta = 90^\circ - \alpha_{pc} \quad (25)$$

Using eqs. 22-24, the pseudocubic lattice parameters for the  $(110)_o$  growth plane of different, available substrates can be calculated and are depicted in tab. 1. The values in tab. 1 clarify that most substrates have anisotropic in-plane lattice parameter, potentially yielding biaxial anisotropic strain.

Table 1: Orthorhombic and pseudocubic in-plane lattice parameter of different substrates for the  $(110)_o$  growth plane.

Substrate	$a_o$	$b_o$	$c_o$	[Ref.]	$a_{pc}$	$b_{pc}$
NdGaO <sub>3</sub>	5.428	5.498	7.708	[50]	3.854	3.863
SrTiO <sub>3</sub> (cubic)	3.905	-	-	[50]	3.905	3.905
DyScO <sub>3</sub>	5.442	5.719	7.904	[51]	3.952	3.947
TbScO <sub>3</sub>	5.466	5.731	7.917	[51]	3.959	3.960
GdScO <sub>3</sub>	5.480	5.746	7.932	[51]	3.966	3.970
SmScO <sub>3</sub>	5.527	5.758	7.965	[51]	3.991	3.983
NdScO <sub>3</sub>	5.575	5.776	8.003	[51]	4.014	4.002

The availability of these substrates leads to the central question: Which material is interesting both from a technological point of view as well as a fundamental study of ferroelectricity? Hereby, two aspects have to be satisfied. The material should (i) be lead-free and (ii) should yield high piezoelectric coefficients. One candidate will be presented in chapter 2.4.

## 2.4. Potassium sodium niobate $K_xNa_{1-x}NbO_3$

Lead-free potassium sodium niobate was grown as bulk crystal first in 1954 [52]. The most promising piezoelectric properties have been found for the composition  $x = 0.5$ . Here, a sort of morphotropic phase boundary exists whereby the symmetry changes from orthorhombic ( $Pm$ ) to orthorhombic ( $Amm2$ ) via an oxygen octahedral tilt [[53],[54]].

This concentration is characterized by a relatively high Curie temperature of  $T_c = 415^\circ\text{C}$  [2] and a high coupling coefficient  $k_p = 0.51$  [1]. Moreover, the longitudinal piezoelectric coefficient amounts  $d_{33} = 80\text{pC/N}$  [1].

Quite similar to other known perovskites,  $K_xNa_{1-x}NbO_3$  with  $x \geq 0.5$  passes the polymorphic phase sequence cubic ( $T > 690\text{ K}$ ), tetragonal ( $T$  between  $690 - 465\text{ K}$ ), orthorhombic ( $T$  between  $465 - 123\text{ K}$ ) and rhombohedral ( $T < 123\text{ K}$ ) [55]. Thus,  $K_xNa_{1-x}NbO_3$  ( $x \geq 0.5$ ) crystallizes in the orthorhombic symmetry at room temperature. Below  $x = 0.5$ , the crystal symmetries and phase transitions are more complicated, especially for  $x = 0$  ( $NaNbO_3$ ). Therefore, they are not considered here.

Potassium sodium niobate is studied as bulk single crystal [[56],[57]] or as ceramic [[58],[59]], but rather less is known about the fabrication and electrical properties in thin film form [[60],[61]]. Typically,  $K_xNa_{1-x}NbO_3$  thin films have been grown by physical methods like sputtering [[62],[63]] or pulsed laser deposition [[64],[65]]. Few papers report growth by chemical sol-gel techniques [[66],[67]]. All of these films exhibit low crystalline quality. Only MOCVD films grown by Schwarzkopf et al. [68] have been shown to be single crystalline and almost stoichiometric.

Comparing the in-plane lattice parameter in the pseudocubic notation of  $K_xNa_{1-x}NbO_3$  to those of the substrates depicted in tab. 1 yields fig. 9. It can be seen that the strain can be tailored from compressive to tensile in small steps by changing either the potassium concentration  $x$  or the substrate, especially the rare-earth scandates.

The evolving ferroelectric phase as a consequence of changing epitaxial strain can be read from a misfit strain-misfit strain phase diagram as it was calculated by Bai and Ma [3] for  $KNbO_3$  (see fig. 10). As can be seen in fig. 10, under biaxial anisotropic strain monoclinic phases (like  $r'$ ,  $ac$ ,  $a_1a_2$ ) can be provoked in  $KNbO_3$ . This result is novel and only possible by extending the Gibbs free energy function to 8<sup>th</sup> order. Indeed, such an anisotropy can be incorporated with the use of orthorhombic substrates as they are depicted in tab. 1. A similar strain-phase relation is expected for  $K_xNa_{1-x}NbO_3$  with  $x \geq 0.5$ .

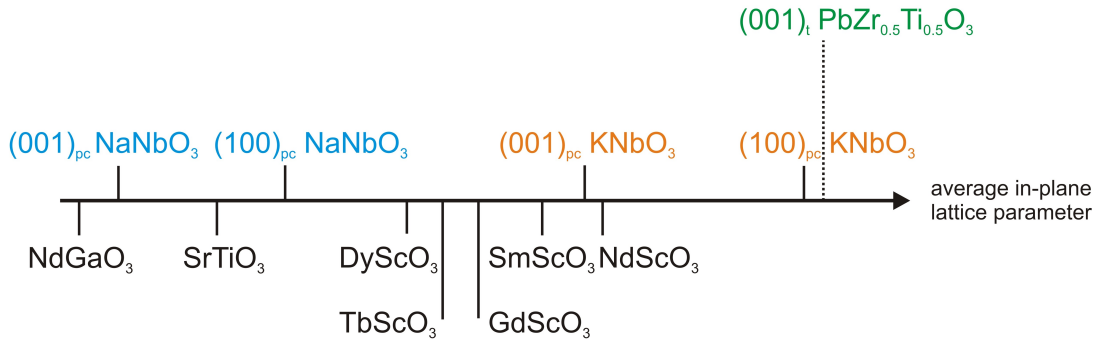


Figure 9: Number line of the average in-plane lattice parameter for: on the top, the end members of the solid solution  $K_xNa_{1-x}NbO_3$ , on the bottom, the substrates depicted in tab. 1. In addition, the position of in-plane lattice parameters of  $PbZr_{0.5}Ti_{0.5}O_3$  according to [69].

The material mostly used for electronic application is lead zirconium titanate ( $PbZr_xTi_{1-x}O_3$ ). At about 50% zirconium concentration, a MPB separates the rhombohedral and tetragonal phase symmetry. In between, a small composition range exists where a monoclinic symmetry evolves that is accompanied by giant piezoelectric responses. In detail, excellent piezoelectric properties as a high longitudinal piezoelectric coefficient  $d_{33} = 413$  pm/V and a coupling constant  $k_p = 0.68$  [70] have been measured. However, it is difficult to obtain exclusively this monoclinic phase [71]. The phase transition point between tetragonal-to-monoclinic-to-rhombohedral exists at room temperature, whereby the tetragonal phase seems to be the most stable one. Here, the lattice parameters are  $a_t = 4.037$  Å and  $c_t = 4.138$  Å [69]. As it can be seen in fig. 9, these values are extremely large in comparison to the depicted rare-earth scandate substrates. Thus, epitaxial growth of fully strained thin films on commonly used substrates is only possible for very thin films. In addition, strain engineering of a tetragonal system is predicted to be rather inefficient in regard of the enhancement of the piezoelectric response as it will be denoted in chapter 2.5 [[38],[72],[73]].

In conclusion,  $K_xNa_{1-x}NbO_3$  is lead-free, non-toxic, has a Curie temperature far above room temperature and a comparable coupling coefficient to lead zirconium titanate. Moreover, monoclinic phases can be introduced via anisotropic lattice strain. This factor enables to enhance the piezoelectric coefficient as it will be discussed in chapter 2.5 in order to be an alternative to lead zirconium titanate.

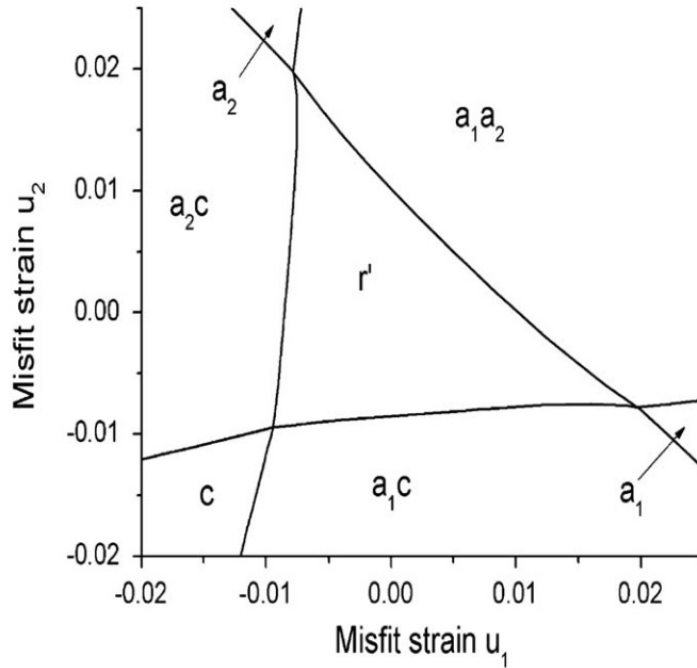


Figure 10: Misfit strain - misfit strain phase diagram calculated by Bai and Ma [3] for  $\text{KNbO}_3$  at room temperature. Taken from [3].

How the piezoelectric response can be enhanced, should be discussed in a general manner in chapter 2.5.

## 2.5. Enhancement of piezoelectric responses

Giant piezoelectric responses were observed first in monoclinic systems at the morphotropic phase boundary in ferroelectric lead zirconium titanate (PZT)-based solid solutions [[69],[74],[75],[76]]. There, the crystal symmetry changes from rhombohedral to tetragonal via a monoclinic bridging phase.

The question why this monoclinicity is related to enhanced piezoelectric amplitudes has been debated for a long time and should be discussed at this point.

The most popular picture of piezoelectricity is a field applied along the polar axis and the subsequent expansion or shrinking of the material in the same direction. This behavior can be described mathematically.

The spontaneous strain  $S_{ij} = Q_{ijkl}P_kP_l$ , or maybe more schematically the piezoelectric

response, changes as a result of an electric field by  $\Delta S_{ij}$ :

$$S_{ij} + \Delta S_{ij} = Q_{ijkl}(P_k P_l + \Delta P_k \Delta P_l) \quad (26)$$

$$\Delta S_{ij} \approx Q_{ijkl}(\Delta P_k P_l + P_k \Delta P_l) = E_p d_{pij} \quad (27)$$

For a polarization distribution  $\mathbf{P} = (0, 0, P_3)$ , an electric field  $\mathbf{E} = (0, 0, E_3)$  leads to:

$$\Delta S_{33} = 2Q_{3333}\Delta P_3 P_3 = E_3 d_{333} \quad (28)$$

$$\Leftrightarrow \Delta P_3 = \frac{E_3 d_{333}}{2Q_{3333} P_3} \quad (29)$$

$$\Leftrightarrow \frac{\Delta P_3}{P_3} = \frac{E_3 d_{333}}{2Q_{3333} P_3^2} = \frac{E_3 \varepsilon_0 \chi_{33}}{P_3} \quad (30)$$

$$(31)$$

Consequently, the response depends on the piezoelectric coefficient  $d_{333} = d_{33}$  and thus on the dielectric susceptibility  $\chi_{33}$ . Such a behavior is called an "Extender".

In the next step, the case of a lateral applied electric field  $\mathbf{E} = (E_1, 0, 0)$  should be considered:

$$\Delta S_{13} = 2Q_{1313}\Delta P_1 P_3 = E_1 d_{113} \quad (32)$$

$$\Leftrightarrow \Delta P_1 = \frac{E_1 d_{113}}{2Q_{1313} P_3} \quad (33)$$

$$\Leftrightarrow \frac{\Delta P_1}{P_3} = \frac{E_1 d_{113}}{2Q_{1313} P_3^2} = \frac{E_1 \varepsilon_0 \chi_{11}}{P_3} = \tan \theta \quad (34)$$

As a result, the polarization vector rotates away from the former polar axis and the response depends on the piezoelectric coefficient  $d_{113} = d_{15}$  and thereby from  $\chi_{11}$ . This means, the response can be higher along a non-polar axis compared to the polar one for a material whose  $\chi_{11} > \chi_{33}$ . This behavior was something completely unexpected. These materials are named "Rotators".

Within the aforesaid model, enhanced piezoelectric responses known from phase transition points can be understood: the lattice softens when approaching the phase transition which is accompanied or expressed in extremely large susceptibilities  $\chi_{ij}$  yielding enhanced piezoelectric properties.

It can be divided immediately between these two species on the basis of polfigures like fig. 5 or energy landscapes like fig. 1. For the former one, barium titanate is an impressive example. It is tetragonal between  $T = 279 - 365$  K, so the polar axis is along

[001], but the maximal  $d'_{33}$  response can be far away from the polar axis namely when the phase transition is near (see fig. 11). The reason is a large dielectric susceptibility  $\chi_{11}$ . Then the maximal piezoelectric response can be expected  $51.6^\circ$  (at  $T = 279$  K)

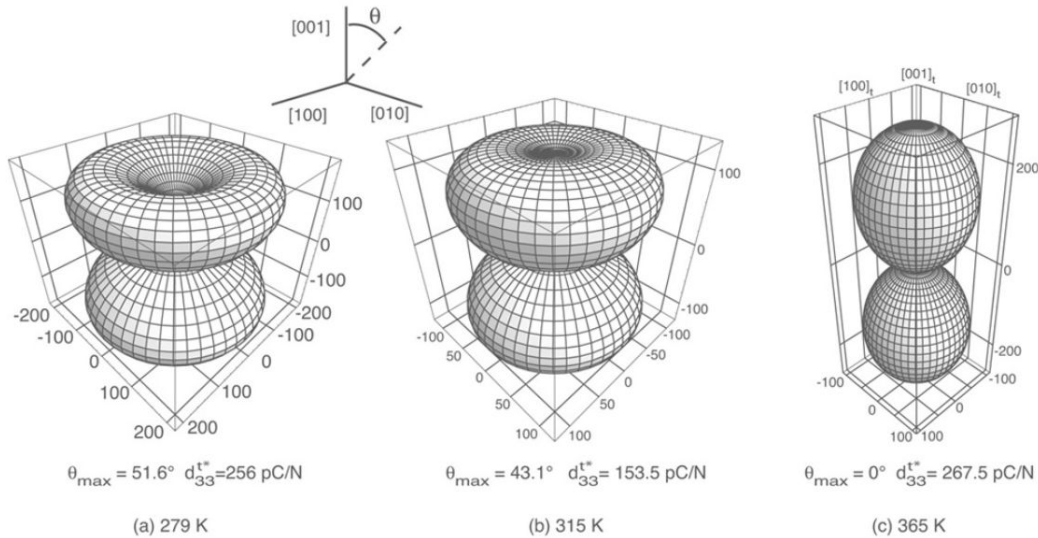


Figure 11: Angular dependency of the longitudinal piezoelectric coefficient  $d'_{33}$  for the tetragonal phase of  $\text{BaTiO}_3$  without any strain or electric field applied in a temperature range between  $T = 279 - 365$  K. Taken from [38].

or  $43.1^\circ$  (at  $T = 315$  K) tilted away from the polar axis.

Rotators can be identified likewise when the Gibbs free energy is plotted as a function of polarization. As an example, I depicted  $\text{Pb}(\text{Zr}_{1-x}\text{Ti}_x)\text{O}_3$  at room temperature for different compositions  $x$  in fig. 12. In the rhombohedral phase in fig. 12a, the four  $\langle 111 \rangle$  directions are energetically preferred, whereas in the tetragonal phase in fig. 12c, the both c-domain states have the lowest energy. In between, when the composition approaches the morphotropic phase boundary at  $x = 0.5$  a clear propensity for a polarization rotation can be seen where the transition pathways along the monoclinic mirror planes are extremely flat.

So, indeed, the Gibbs free energy instability is the thermodynamic origin of the enhanced piezoelectric response. This flat energy landscape can be achieved only in monoclinic symmetries. In contrast to high symmetric point groups, here, the prior symmetry element is no axis but the monoclinic mirror plane. Consequently, the polarization vector is able to rotate continuously within this plane. That discussion explains the observed giant piezoelectric responses at the morphotropic phase boundary in  $\text{Pb}(\text{Zr}, \text{Ti})\text{O}_3$  where the material crystallizes in the monoclinic orientation.

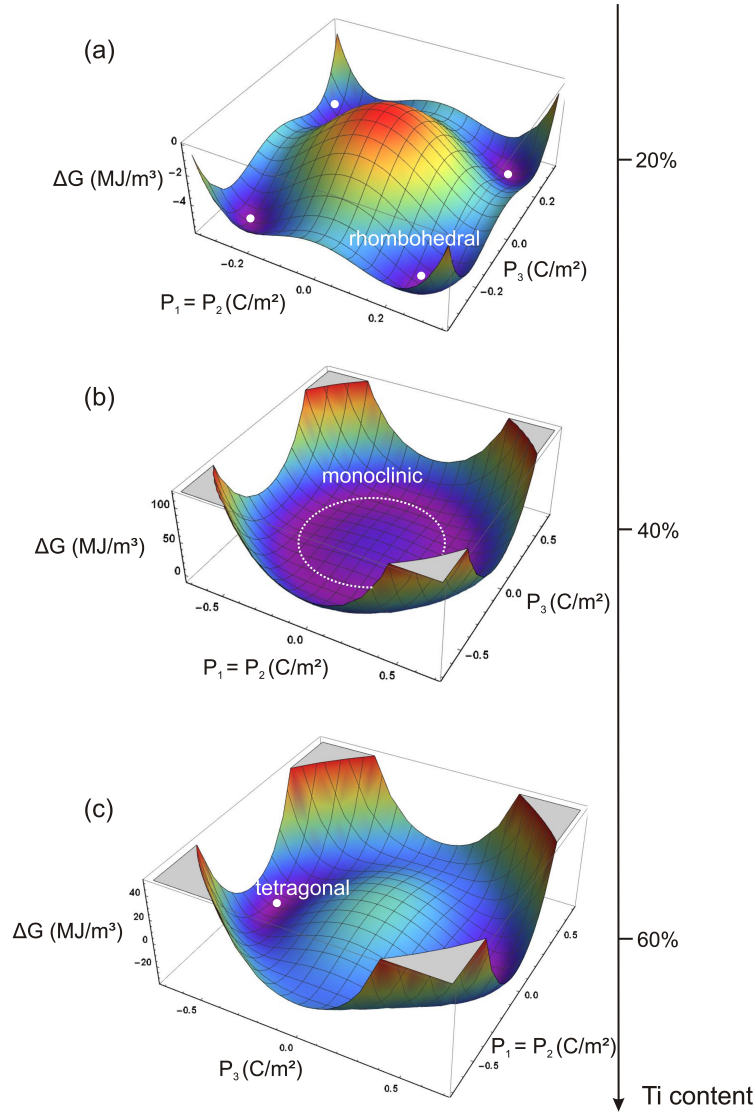


Figure 12: Gibbs free energy in dependence of the polarization  $P_i$  for (a)  $x = 0.2$ , (b)  $x = 0.4$  and (c)  $x = 0.6$ . Calculated according to the material constants [77].

It should be noted, to calculate the same energy surface as in fig. 12 for monoclinic phases would need (i) an expansion of eq. 2 to the 8<sup>th</sup> order and (ii) the required material specific constants. Due to the lack of the latter, it can not be presented here.

If a material will behave like an extender or rotator can not only be estimated from the aforementioned polfigures or energy landscapes but can be calculated. Mathematically, the turning point has to be evaluated:

$$\frac{\partial d'_{33}}{\partial \theta} = 0 \quad (35)$$

The solution is approximately the same for all crystal symmetries. A material behave

like a rotator when:

$$\frac{d_{15}}{d_{33}} \geq \frac{3}{2} - \frac{Q_{1313}}{Q_{3333}} \approx \frac{3}{2} \quad (36)$$

To have an impression which material is suited, the ratio 36 is calculated for some examples in tab. 2 according to the piezoelectric coefficients depicted in [73]:

Table 2: Ratio of the shear and longitudinal piezoelectric coefficient  $d_{15}$  and  $d_{33}$ , respectively, for different materials [73].

	PbTiO <sub>3</sub>	BaTiO <sub>3</sub>	KNbO <sub>3</sub>	PMN – 33PT
$\frac{d_{15}}{d_{33}}$	0.7	6.0	7.0	22.0

It has to be noted, that PMN – 33PT is a relaxor material and is therefore not suitable for classical domain engineering. In consequence, potassium niobate is a perfect rotator candidate and hence a good combination of the two aspects lead-free and expected high piezoelectric responses.

## Part II.

# Growth & Characterization methods

### 3. Thin film deposition

The metal organic chemical vapor deposition technique (MOCVD) is a coating method related to the group of chemical deposition processes. The central point is the growth of a single layer from the vapor phase. The latter consists of a chemical compound of a metal-organic precursor and the material to be deposited. The film stoichiometry can be controlled by the composition in the gas phase. Thus, it is possible to produce films with high crystalline quality and precise stoichiometry.

Until now, this method has not been applied for potassium sodium niobate due to both the low availability of suitable MO precursor as well as to the high volatility of the alkali components. Challenging is that the source material exists oftentimes only in the solid state and has high vapor pressures. So a slightly modified variant of the typical MOCVD is applied as illustrated in fig. 13.

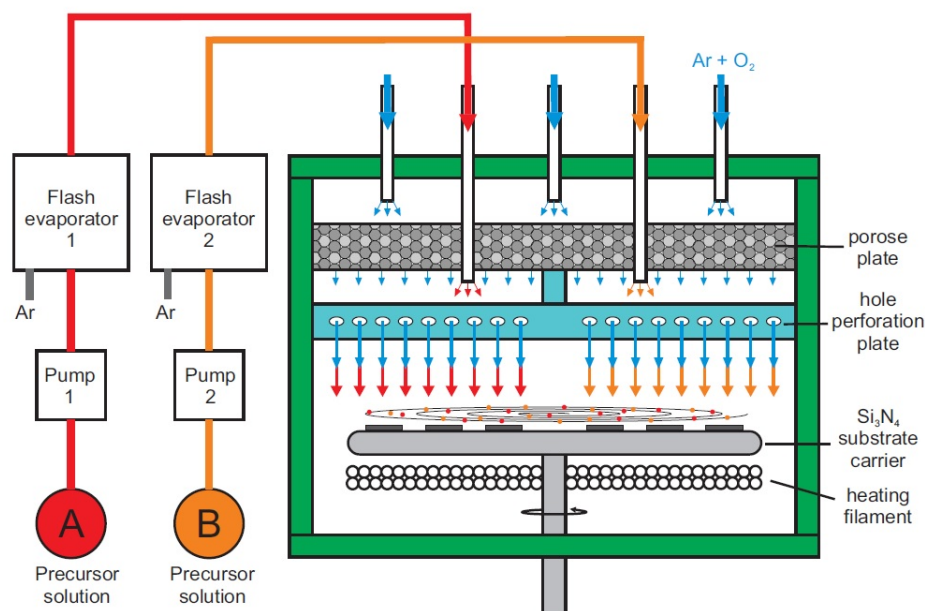


Figure 13: Schematic sketch of the MOCVD system. For details see text. Taken from [39].

In the liquid-delivery MOCVD, the metal-organic precursor is previously dissolved in an organic solution. For the deposition of potassium sodium niobate,  $K(\text{thd})$  and  $\text{Na}(\text{thd})$  ((thd) = 2,2,6,6-tetramethyl-3,5-heptanedione) and  $\text{Nb}(\text{EtO})_5$  were dissolved

in dry toluene and the flash evaporators were heated up to 180° or 190°, respectively. Via two peristaltic pumps the fluid is conveyed into independent flash evaporators and is dropped onto a hot plate for vaporizing. In the next step, the gaseous components were directed by means of an inert carrier gas, in this case argon, into the reaction chamber. Simultaneously, pure oxygen was introduced in the same chamber. The gas mixture now passed a shower head whose core is a combination of a porous - and a hole plate to ensure uniform distribution of oxygen (see fig. 13). On an underlying carrier made of silicon nitride the substrates are fixed with silver glue and heated up by a rear filament. This carrier is put in continuous rotation and swirled the gas mixture of MO precursor, argon and oxygen and thereby ensured a homogeneous composition. Common parameters for film deposition were a gas pressure in the reaction chamber of 2.6 kPa and a ratio of gases  $O_2/Ar = 0.63$ . Furthermore, the carrier was operated with 560 revolutions per minute and the depositions were performed at 700°C.

All substrates used have an intentional off-orientation of 0.1° towards the  $[1\bar{1}0]_o$  direction and are first cleaned with acetone and 2-propanol. The subsequent annealing in pure oxygen for one hour at  $T = (1050 - 1150)^\circ\text{C}$  leads to the formation of a regular step-terrace surface structure with atomic steps ( $\approx 4\text{\AA}$ ) and terraces of about 200 nm in width. This structure favors the nucleation and results in an increased growth rate. Another advantage of annealing is that a single surface termination remains. For more details, see [68].

## 4. Atomic Force Microscopy

The atomic force microscope (AFM) is a scanning probe method, which was developed in 1985 by Gerd Binnig, Calvin Quate and Christoph Gerber [78]. It becomes one of the most important tools in surface science for mechanical scanning of surfaces. By measuring atomic forces, characteristic properties of materials can be investigated on the nanometer scale. So, in regard of the achievable resolution it represents a bridging technique between the light - and electron microscopy.

A schematic sketch of an atomic force microscope is shown in fig. 14a.

The main components are either a white light-emitting diode or a laser (depending on the design), the photodetector and the probing tip. The latter forms the core of the machine and consists mostly of a rectangular cantilever beam with dimensions (length x width) of  $(100 - 200)\mu\text{m} \times (10 - 40)\mu\text{m}$ . An ultra-sharp tip is mounted at one end

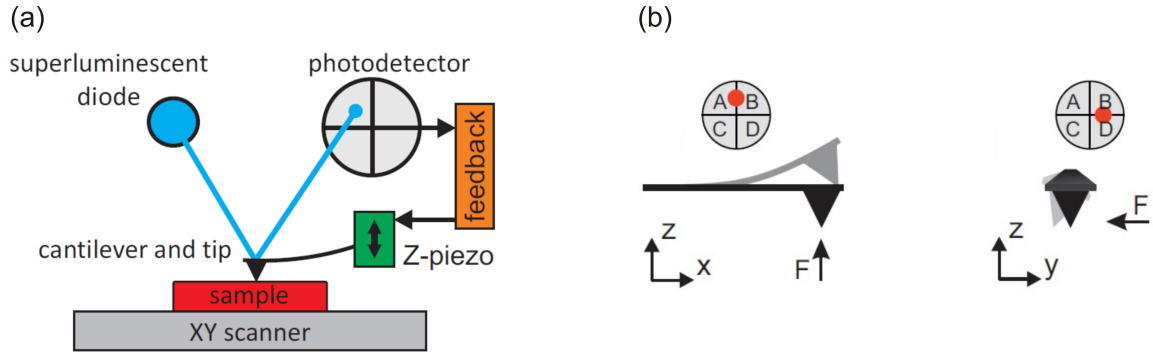


Figure 14: (a) Scheme of a typical AFM setup. For a detailed description see text. (b) left: deflection and right: torsion of the cantilever caused by forces acting on the tip from different directions. The resulting reflected cantilever beam into the detector is marked by red dots. Adapted from [39].

of the beam with a diameter of typically (10 – 20)nm. To manufacture these probes usually silicon or silicon nitride are used. Depending on the force to be detected, the cantilever can be additionally coated, eg with conductive metals. This entire beam is characterized by the spring constant  $k$  with a typical range of  $k = (0.01 – 40)\text{Nm}^{-1}$ .

The sample is placed on a scanning stage which can be moved in x-y direction manually or by piezo stack actuators. Next, a probing tip is brought into contact with the surface.

During the measurement, the nanoscopic needle is scanned line by line in a defined grid over the sample surface. As a result of the changing morphology, the beam is differently deflected. Via the reflection of the laser spot on the backside of the cantilever, this deflection is recorded on the detector as depicted in fig. 14b. The latter consists of four segments A-D in combination with a differential amplifier and is basically a diode. The task is to convert the incident light signal into a voltage pulse in order to scale the topography in meters.

The changing light intensity between the upper two sections  $A + B$  and the lower ones  $C + D$  yields information on the vertical deflection of the cantilever whereas the difference between the areas of  $A + C$  and  $B + D$  reflects the torsional forces. In sum, the measurement method plots a three-dimensional map of the surface.

In order to ensure a resolution on the nanometer scale, the measuring system must be shielded against external influences. For this purpose, the AFM is positioned on an active, vibration damping table (in our lab an Accurion Halcyonics micro 40) for

absorption of mechanical vibrations, e.g. subsonic noise. On the other hand, the entire setup is enclosed in an acoustic hood made of steel for shielding of acoustic vibrations.

## 5. Piezoresponse Force Microscopy

Basically, the piezoresponse force microscopy (PFM) is a special mode of the AFM as it is shown in fig. 15. The imaging in PFM mode is based on the inverse piezoelectric

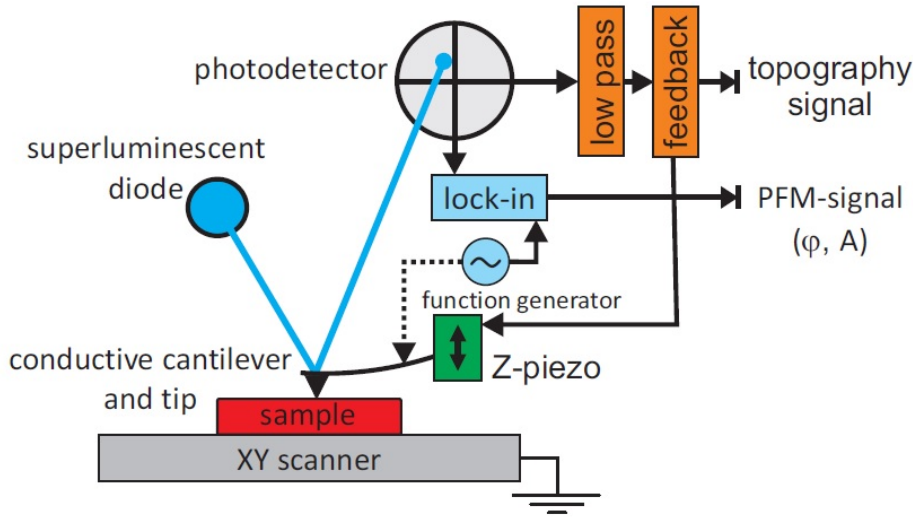


Figure 15: Model of the PFM mode as complement to the basic AFM setup shown in fig. 14a.

Taken from [39].

effect. As discussed in chapter 1, the application of an electrical voltage leads to a mechanical deformation in piezoelectric materials. In the PFM, the bias is applied via a conductive tip which is in contact with the surface. For that purpose, an alternating electric field is used stimulating an oscillation in the material underneath, which in turn enables the cantilever to vibrate. When the applied potential difference has the form of:

$$V_{tip} = V_{dc} + V_{ac} \cdot \cos(\omega t) \quad (37)$$

the 1<sup>st</sup> Harmonic  $d$  of the cantilever can be calculated as follows [30]:

$$d = d_0 + A \cdot \cos(\omega t + \phi) \quad (38)$$

In eq. 38,  $d_0$  represents the static component due to the dc component,  $A$  is the amplitude and  $\phi$  is the phase of the signal. This means that the material gives a piezoelectric response to the applied ac voltage with the characteristic values: amplitude  $A$  and phase shift  $\phi$ . To measure and especially separate these signals from both the

input signal and the topography a lock-amplifier is used. As shown in fig. 16 important conclusions can be gathered from these two parameters on the domain structure. If the

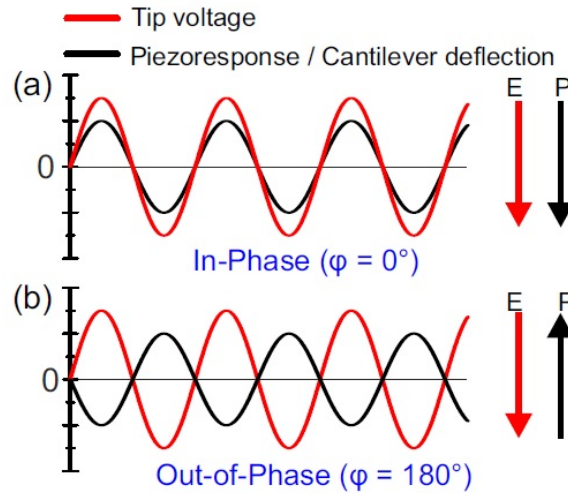


Figure 16: Piezoresponse signal (black) (a) in-phase ( $\phi = 0^\circ$ ) and (b) out-of-phase ( $\phi = 180^\circ$ ) with the applied alternating voltage marked in red color. Taken from [39].

electric field vector  $\mathbf{E}$  of the applied voltage is parallel to the polarization vector  $\mathbf{P}$  the sample will extend in the vertical direction by means of a lateral reduction as can be seen in fig. 17a. In the case of an antiparallel arrangement, the solid will shrink in the

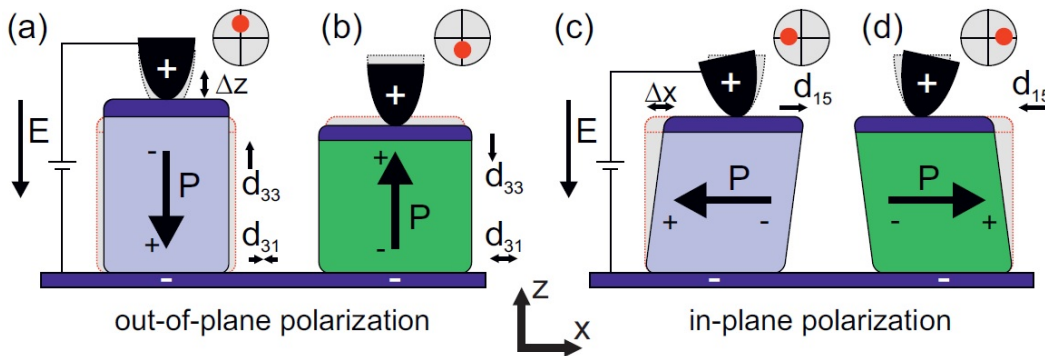


Figure 17: The converse piezoelectric effect as a result of an applied voltage between the conductive tip and a bottom electrode in a piezoelectric material. The induced tip deflection as well as the corresponding position of the reflected beam on the photodiode are displayed by red dots. The effect is shown for (a) vertical and (b) lateral polarization alignments. Taken from [79].

$z$  direction and expand in the  $x$  direction. In the detector, this response is recorded as amplitude, namely  $\Delta z$ , and phase shift  $\Delta\phi$ . This allows a distinct characterization of vertical domains in view of the orientation of the polarization vector and is referred to vertical PFM (VPFM). If the electric field vector is aligned parallel to the polarization

vector, there will be no phase shift  $\Delta\phi = 0^\circ$  between the signals, whereas in antiparallel position a phase shift of  $\Delta\phi = 180^\circ$  occurs. The amplitude, however, reveals something about the strength of polarization. This longitudinal displacement is related to the tensor element  $d_{33}$ .

However, if the polarization of the sample is aligned in the film plane, and consequently perpendicular to the electric field, this will lead to a shearing of the sample surface and therefore to the torsion of the cantilever. As already stated in the AFM chapter 4, this rotation of the tip can be measured as a light intensity difference in the areas between  $A + C$  and  $B + D$ . This signal thus reveals information about a right- or leftward orientation of polarization. The strength of the twist, hence the amplitude, is associated with the shear tensor element  $d_{15}$ . This measurement method is called lateral PFM or LPFM.

In the case of an orientation of the polarization vector neither parallel nor perpendicular to the electric field, the measurement signal will have both a lateral and vertical component.

Oftentimes, the piezoresponse PR is calculated from both the amplitude and the phase according to eq. 39:

$$PR = \text{amplitude} \cdot \cos(\text{phase}) \quad (39)$$

Simultaneously to the piezoelectric response, the surface topography is recorded by feeding a low-pass filter with the low-frequency cantilever motion. As a result, both the surface topography and the polarization are measured in a single measuring step and give rise to spatially resolved polarization maps.

An important note for interpreting the domain structure is that all subsequent measurements (if not stated otherwise) have been carried out at room temperature.

## 5.1. Contributions of a PFM signal

Contrary to the theoretical idea presented in chapter 5 that pure electromechanical forces occur in the PFM, electrostatic forces also act in the experiment, which can falsify the measuring signal. These can be divided into different categories and should be discussed at this point on the basis of [80].

The total amplitude  $A$  of a conductive coated cantilever in contact with a sample

surface can be described as follows:

$$A = A_{piezo} + A_{el} + A_{nl} \quad (40)$$

Hereby,  $A_{piezo}$  stands for the purely electromechanical deflection of the cantilever due to the piezoelectric effect.  $A_{el}$  describes the electrostatic interaction of the tip with the surface and  $A_{nl}$  is the non-local part of the electrostatic interaction due to the capacitive coupling between tip and surface.

Eq. 40 consists of the following summands: According to the piezoelectric effect, the longitudinal deflection  $A_{piezo}$  of a sample is linked linearly to the dielectric tensor element  $d'_{33}$  at a perpendicularly applied voltage  $V_{ac}$  [[81],[82]]:

$$A_{piezo} = d'_{33} \cdot V_{ac} \quad (41)$$

The symbol ' refers to the different coordinate systems of sample and laboratory. The two further terms in eq. 40 describe the electrostatic interactions as follows:

$$A_{el} = F_{loc} \cdot V_{ac} \cdot (V_{tip} - V_{loc}) \quad (42)$$

$$A_{nl} = F_{nl} \cdot V_{ac} \cdot (V_{tip} - V_{av}) \quad (43)$$

In the case of local influences, the local potential gradient  $V_{loc}$  and the local capacitive forces between tip and sample  $F_{loc}$  play the decisive role. For non-local interactions (=influences that exceed the cantilever dimension), the average surface potential  $V_{av}$  and the capacitive forces between tip and sample  $F_{nl}$  dominate the signal.

Which changes can appear in the measured PFM signal? If the vertical PFM signal is measured over a surface with  $c^+$ ,  $c^-$  and a domains, the mentioned interactions can lead to falsifications of the measurement signal as depicted in fig. 18. In the case of pure electromechanical coupling, the forces  $F_{loc} = F_{nl} = 0$ . This means that the amplitude signal is equal for  $c^+$  and  $c^-$  domains, and zero for a domains. The corresponding phase signal shows a phase shift of  $180^\circ$  between the vertical c domains and is zero (or in the range of noise) for lateral a domains.

If there is a weak non-local electrostatic interaction  $F_{nl} \neq 0$  (fig. 18b), it will result in a slightly different amplitude signal for vertical  $c^+$  and  $c^-$  domains, while the phase shift is still correctly displayed with  $180^\circ$ . In addition, a non-zero signal for lateral a-domains evolves in the vertical PFM, which falsifies additionally the phase contrast. Similarly behavior is expected for weak local electrostatic forces  $F_{loc} \neq 0$  (fig. 18c).

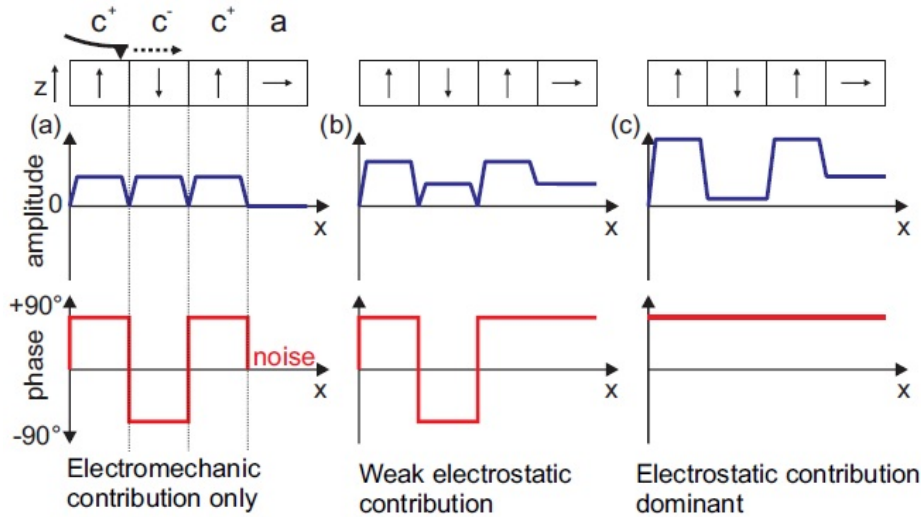


Figure 18: Representation of the piezoresponse divided in amplitude and phase signals over a  $c^+/c^-/c^+/a$  domain pattern for three different electrostatic contributions. Taken from [39].

However, if this component dominates, there won't be any phase shift and a strongly distorted amplitude signal.

This discussion clearly shows that a trustworthy measurement can only be obtained with a dominant electromechanical response. It is therefore unavoidable to minimize the electrostatic interactions.

How this can be achieved experimentally will be discussed below.

## 5.2. Experimentally influencing the PFM signal

First of all, a good electrical contact between the sample surface and the tip must be ensured. An intermediate layer between the two components can affect the measurement signal. However, they naturally occur in the form of, for example, thin water films on the surface or oxidation of the tip, since the measurement is not taken under vacuum conditions. Thus further experimental parameters have to be optimized.

One approach is to make use of the different contrast mechanisms between electromechanical and electrostatic interaction. In the first case, this is a purely stress-induced effect which leads to a mechanical deflection. In the second case, forces between the tip and the sample play the dominant role and are therefore influenced by the probe geometry or the measuring frequency. At this point it can be hooked up.

Solving the differential equation of a clamped beam [80] yield information how the

electromechanical and electrostatic contributions scale with the modulation frequency  $\omega$  [80]:

- i vertical components of the electromechanical force  $\propto \frac{k}{\omega}$
- ii local electrostatic force  $\propto \frac{1}{\omega}$
- iii non-local electrostatic force  $\propto \frac{1}{\omega^{\frac{3}{2}}}$

All contributions decrease with increasing measuring frequency. Furthermore, the frequency dependency is the same for purely mechanical and local electrostatic contributions, but they differ for uneven spring constants. Thus, this can not be separated here by choosing a suitable frequency of the alternating voltage, but by choosing proper cantilever properties. For dominant electromechanical response the spring constant  $k$  should be [80]:

$$k \gg \frac{LwU\varepsilon_0}{48H^2d_{33}} \quad (44)$$

For typical measuring conditions for weak piezoelectric materials, such as thin films, where the cantilever dimensions are in the range of length  $L = 225\mu\text{m}$ , width  $w = 30\mu\text{m}$  and height  $H = 15\mu\text{m}$  as well as a voltage of  $U = 1\text{V}$  and a resulting response of  $d = 5\frac{\text{pm}}{\text{V}}$ , this means a stiffness larger than  $1.1\frac{\text{N}}{\text{m}}$  must be chosen. This can be well done experimentally and has been realized in the present experiment by the choice of cantilever with  $k_1 = 2.8\frac{\text{N}}{\text{m}}$  or  $k_2 = 5.0\frac{\text{N}}{\text{m}}$ .

A further possibility to reduce unwanted electrostatic influences is the use of top electrodes. Since these could not be deposited routinely in our institute, this method was rejected.

Basically this is a rather static view on the problem, neglecting dynamic and spatial effects like buckling. This would, however, make an analytical solution impossible and would have to be treated numerically by differential equations adapted to the system, which should not be discussed here.

In summary, the experimental signal can be shifted to high electromechanical proportions when the cantilever has a sufficient stiffness and the measuring frequency is chosen to be correspondingly high. The latter can be driven up to the resonant frequency, which will be explained in more detail in the following section.

### 5.3. Resonance enhancement of PFM signal

The measuring mode in the PFM is based on inducing vibrations into a piezoelectric sample by an electrical field and evaluating the strength as well as the direction of the response with regard to the piezoelectric effect. It is precisely this vibration that can be driven through a suitable choice of voltage up to the resonance case where the electromechanical interaction reaching its natural maximum. As a result, the signal-to-noise ratio is minimized, which is almost unavoidable for an evaluable signal in the case of weak piezoelectric samples, such as thin films.

However, the main problem is that the contact resonance frequency  $f_0$  depends on the sample-tip contact and is therefore, for example, topography-dependent.

To avoid this obstacle, Rodriguez et al. [83] developed a method in which the contact resonance frequency is tracked for each measurement point. For this purpose, the tip-sample contact is described by two frequencies  $f_1$  and  $f_2$ , where  $f_1$  is the same measure smaller than  $f_0$  as  $f_2$  is larger than  $f_0$ . The corresponding amplitudes  $A_1$  and  $A_2$  are selected in the manner that  $A_1 = A_2$  is always valid. The latter are used to track the resonant frequency  $f_0$ . For a better understanding, all sizes are shown in fig. 19. When

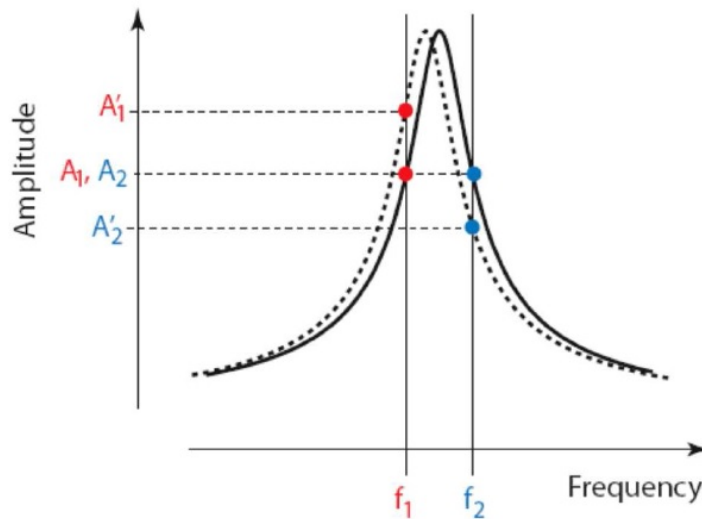


Figure 19: Schematic sketch of the piezoelectric resonance peak. Central point of the DART mode is tracking the contact-resonance amplitude peak by dual-frequency excitation. For the tracking, the amplitudes on both sides of the flank and the corresponding frequencies are essential. Taken from [83].

the resonance peak shifts due to changing characteristics of the tip-surface contact, the amplitude equality is no longer valid ( $A'_1 \neq A'_2$ ). This result is fed into a feedback loop and results in a changed signal frequency until  $A'_1 = A'_2$  holds.

This resonance tracking was technically implemented in the Asylum MFP-3D classic as a dual AC resonance tracking (DART) method and was used for each of the subsequent measurements.

#### 5.4. Evaluation of the local piezoelectric coefficient $d'_{33}$

In this work, the local piezoelectric coefficient  $d'_{33}$  of thin films was measured via resonance-amplified PFM. The amplitude  $A$  measured in DART mode can be described as follows [84]:

$$A = d'_{33} \cdot V_{ac} \cdot Q \quad (45)$$

In eq. 45,  $Q$  corresponds to the amplification factor of the measurement signal. Depending on the cantilever used, typical values for  $Q$  are in the range of 10-100. This value must be known for each single measurement point and be calculated off. Since this value is different at each measurement point as a result of tracking the system's resonance, the operation is not trivial or can be made manually.

If a surface is measured in the DART-PFM mode by tracking the first resonant frequency, four quantities  $A_{1,2}$  and  $f_{1,2}$  can be obtained from a single measurement. If the tip-sample-contact during the oscillation is described as a damped harmonic oscillator (DHO), the individual measured variables  $A_i$  and  $f_i$  are composed as follows [85]:

$$A_{1,2}(f_{1,2}) = \frac{A_{Drive} f_0^2}{\sqrt{(f_0^2 + f_{1,2}^2)^2 + (f_0 f_{1,2}/Q)^2}} \quad (46)$$

$$\phi_{1,2}(f_{1,2}) = \tan^{-1} \left( \frac{f_0 f_{1,2}}{Q(f_0^2 - f_{1,2}^2)} \right) + \phi_{Drive} \quad (47)$$

Where  $f_0$ ,  $A_{Drive}$ ,  $\phi_{Drive}$  and  $Q$  are the four unknown parameters of the resonance frequency, amplitude, and phase and the quality factor.

Since four quantities are measured and four unknown ones remain, the equation system is uniquely solvable and  $Q$  can be determined for each point [86]. This conversion is carried out numerically and provides a picture with quasi subtracted resonance.

In order to compare several samples, however, the sensitivity of the detector on the deflection of the cantilever has to be calibrated. The most frequent method for this purpose is the inverse optical lever sensibility, InvOLS, as it should be explained on the basis of [[87],[88],[89]].

Experimentally, the laser or white light diode spot is reflected from the rear side of the

cantilever into the position - sensitive detector (PSD), that detects changes in the laser position as a voltage change  $\Delta V$ . The measured electric signal has to be converted into the cantilever deflection  $x$ , which is called the InvOLS calibration.

In scanning force microscopes this is realized by the force  $\tau$ , which can be described with Hooke's law in dependence of the deflection  $x$  and the spring constant  $k$ :

$$\tau = kx \quad (48)$$

This means that the two quantities  $x$  and  $k$  must be known in order to measure the force at the same time for each measurement.

First, a force-distance curve  $\tau(x)$  is measured. For this purpose, the cantilever is brought into contact with the surface and then retracted by a defined distance. From this measurement, the voltage  $\Delta V$  in the PSD is gained as a function of the distance  $x$ . It follows from Hooke's law that the contact regime between sample and peak is linear in the force-distance curve. InvOLS can be obtained from the slope of exactly this linear part of the curve:

$$\tau = kx = k \cdot \text{InvOLS} \cdot \Delta V \quad (49)$$

In a second step, the spring constant  $k$  will be determined. For this task, a thermal spectrum is recorded. Hereby, the resonance frequency of the cantilever is measured by applying an iterative series of frequencies and finally averaging the result. The outcome is a real-time measurement of the amplitude of the cantilever as a function of the applied frequency (power spectrum). In the following, the 1<sup>st</sup> Harmonic is fitted with a Gaussian function and the resonance frequency and finally the spring constant  $k$  is determined via the software.

In the end, the detector is calibrated in the sense that a defined voltage in the PSD can be recalculated into a real deflection. Thus, the measured amplitude can be depicted in meter and after division by the drive voltage, the longitudinal piezoelectric coefficient  $d'_{33}$  can be gained with spatial resolution.

## 6. X-ray diffraction

### 6.1. High-resolution x-ray diffraction (HRXRD)

In the following chapter, a brief and basic introduction should be given to the structural investigation of the crystal lattice by means of high-resolution x-ray diffraction (HRXRD).

X-rays were discovered rather accidentally by Conrad Wilhelm Röntgen in 1895 during a study on cathode rays. He discovered luminous effects that can not be related to the actual experiment itself and called them therefore x-rays. Their wave length  $\lambda$  is in the range of 1 pm to 10 nm and thus on the same scale as atomic distances in a crystal. As a result, the three dimensional crystal lattice can serve as diffraction grating for the x-rays to examine the lattice structure itself in detail. In contrast to measurements with electrons or neutrons, the access to x-rays are comparable easy and the penetration depth in the range of microns is rather large.

The scattering process can be described as follows. The electrons of the atoms are excited to forced vibrations as Hertzian's dipoles within the electromagnetic field of the incident x-rays. As a result, they reemit x-rays of the same frequency that can interfere. Depending on the distance of the atoms in the lattice, unequal path differences result for the diffracted waves. Since crystals consist of three-dimensional, periodically arranged structural units, constructive interference is limited to particular angles  $\theta$ . In a schematic model, crystal planes can be spanned between these atoms denoted as net planes. The distance  $d$  of these planes is the decisive parameter for the path difference. Mathematically, the constructive interference during the diffraction process can be described by the Bragg equation 50:

$$n\lambda = 2d \sin \theta \quad n \in \mathbb{Z} \quad (50)$$

When the path difference  $d$  of two net planes is an integer multiple of the x-ray wave length  $\lambda$ , constructive interference occur. This scenario is restricted to selected angles towards the net plane for the incident beam that are called Bragg angles  $\theta_B$ .

Transferring this model into reciprocal space requires the usage of vector algebra [90] as depicted in fig. 20. A monochromatic, collimated incident x-ray beam with a wave vector  $\mathbf{k}$  and length  $\frac{2\pi}{\lambda}$  hits the sample under an inclination angle  $\omega$ , defined between the x-ray source and the sample surface. For an elastic scattering process as the one discussed in this chapter, the reemitted wave has the wave vector  $\mathbf{k}'$  with the same

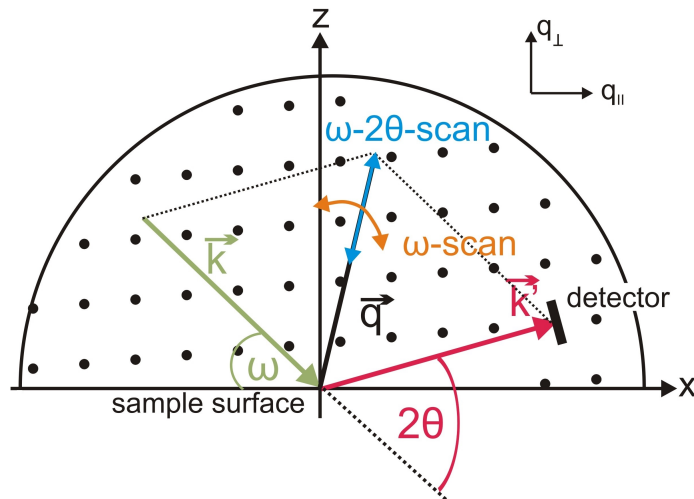


Figure 20: Schematic illustration of the HRXRD scattering geometry in 2D section of the Ewald sphere. Adapted from [90].

length  $\frac{2\pi}{\lambda}$ .

Constructive interference between waves reemitted from two points in the reciprocal space with the spatial difference vector  $\mathbf{K} = \mathbf{k}' - \mathbf{k}$  can be expected exclusively when  $\mathbf{K}$  is equal to a reciprocal lattice vector  $\mathbf{q}$ . This restriction is denoted as Laue equation 51:

$$\mathbf{K} = \mathbf{q} \quad (51)$$

Consequently, the scattering vector  $\mathbf{q} = \mathbf{k}' - \mathbf{k}$  depends on  $\omega$  and  $2\theta$  as well. Splitting  $\mathbf{q}$  into the components parallel (=in-plane) and normal (=out-of-plane) to the sample surface yields [90]:

$$q_{\parallel} = \frac{2\pi}{\lambda} [\cos(2\theta - \omega) - \cos \omega] \quad (52)$$

$$q_{\perp} = \frac{2\pi}{\lambda} [\sin(2\theta - \omega) + \sin \omega] \quad (53)$$

Two different measurement procedures are typically used. First, when the sample and the detector are both rotated with an angle-relation of 1:2, the direction of  $\mathbf{q}$  is kept constant while its length changes. Thus, the Bragg reflection is scanned along radial direction which is named  $\omega - 2\theta$ - or  $\theta - 2\theta$  scan. This case is depicted in fig. 20 by a blue double arrow.

Second, if the detector position  $2\theta$  is fixed but the sample is rotated and thus  $\omega$  is changing ( $\omega$ -scan), the angle between  $\mathbf{k}$  and  $\mathbf{k}'$  remains unmodified. As a result, the length of  $\mathbf{q}$  is fixed while the scanning direction is angular along the Ewald sphere [91].

This measurement principle is called  $\omega$ -scan and is illustrated by a double orange arrow in fig. 20.

Due to the fact, that the  $\omega - 2\theta$ - and  $\omega$ -scan are locally perpendicular, a combined measurement yields a surface in the reciprocal space. This technique is called reciprocal space mapping.

In epitaxial growth, the strain state of the film is of crucial interest. This information can be derived from the relative distance between film and substrate peak (whose angular position is known). From eq. 50 it follows:

$$\frac{\Delta d}{d} = \frac{\Delta 2\theta}{\tan \theta_{\perp}} \quad (54)$$

with  $\Delta 2\theta = 2\theta_{\perp} - 2\theta_s$  and  $\Delta d = d_{\perp} - d_s$ . Hereby,  $\theta_{\perp}$  and  $\theta_s$  are the Bragg positions of the film and the substrate, respectively. Similar,  $d_{\perp}$  and  $d_s$  denote the vertical lattice parameter of the film and the substrate, respectively. Using eq. 54, the vertical lattice parameter of the film can be calculated via:

$$d_{\perp} = d_s \cdot \left[ 1 - \frac{2\theta_{\perp} - 2\theta_s}{2} \cdot (\tan \theta_{\perp})^{-1} \right] \quad (55)$$

$$= \frac{n\lambda}{2 \sin \theta_s} \cdot \left[ 1 - \frac{2\theta_{\perp} - 2\theta_s}{2} \cdot (\tan \theta_{\perp})^{-1} \right] \quad (56)$$

If the grown films are of good crystalline quality ( $< 1$  nm rms roughness) and thus having smooth interfaces and surfaces, thickness oscillations emerge on each side of the film reflection. These Kiessig fringes results from the fact, that the experiment is equal to the diffraction on a slit yielding a modulation by  $(\frac{\sin \theta}{\theta})^2$ . Evaluating the distance of the minima of the fringes  $\Delta\theta_{\min}$  in a symmetric reflex yields the layer thickness  $t$ :

$$t = \frac{\lambda \sin \theta_{\perp}}{\Delta\theta_{\min} \cdot \sin(2\theta_{\perp})} \quad (57)$$

The high resolved x-ray diffraction measurements were performed on a D8 Discover diffractometer from Bruker Corporation. X-ray  $\text{CuK}\alpha$  radiation provided by a copper tube was employed as source. If relative changes in the vertical lattice parameter of  $\frac{\Delta d}{d} = 3 \cdot 10^{-4}$  Å should be measured, the angular resolution of the diffractometer has to be  $\omega = 0.003^{\circ}$  [91]. Hence, the x-ray beam has to be collimated. The primary beam is precollimated by a Goebel mirror and than transmits a 2-bounce Si channel cut monochromator for minimizing the divergence of the x-ray beam. In the end,  $\text{CuK}\alpha_1$  radiation ( $\lambda_{\text{CuK}\alpha_1} = 1.54056$  Å) is collimated to  $< 20$  arcsec. The diffracted beam enters a scintillation counter trough a collimating slit system.

In order to evaluate the in- and out-of-plane lattice strain state of the epitaxial film, reciprocal space maps have to be recorded. In contrast to the high resolution x-ray diffraction scans described above, a one-dimensional Dectris Mythen 1K detector was used for that purpose. The advantage of this detector is the measurement of the respective Bragg reflection within an angular range of  $8.7^\circ$  [91]. In consequence, to map a surface in reciprocal space do not require both - an  $\omega - 2\theta$ - and  $\omega$ -scan - but rather a single movement of the  $\omega$  axis. This procedure decreases the measuring time immensely.

## 6.2. Grazing incidence x-ray diffraction (GIXD)

In the chapter before, the large penetration depth was depicted as one among many advantages of x-rays. Unfortunately, in case of thin films, that property is not always desirable because of the huge background signal of the substrate. To avoid the latter, the measurement geometry has to be slightly modified in this way that the x-ray hits the sample surface at a very grazing angle of incidence  $\vartheta_i$  and an in-plane angle  $\theta_i$  (see fig. 21a). Indeed,  $\vartheta_i$  has to be close to the angle of total external reflection. As a

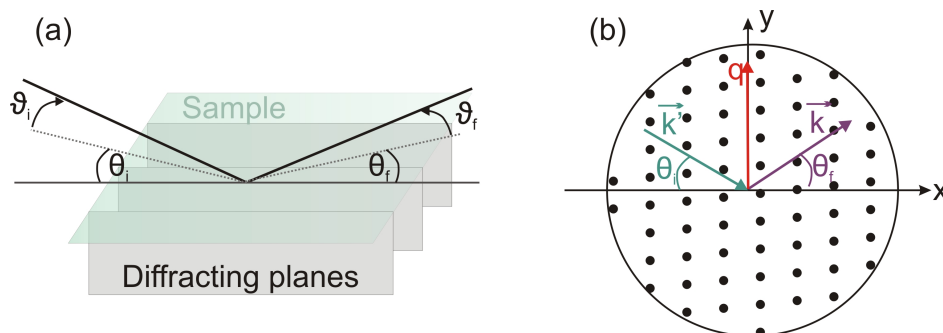


Figure 21: Schematic illustration of the GIXD scattering geometry. Adapted from [90].

result, diffraction occurs solely from net planes that are almost perpendicular to the sample surface.

As illustrated for the reciprocal space in fig. 21b, the scattering vector  $\mathbf{q}$  thus depends on the in-plane entrance and exit angle  $\theta_i$  and  $\theta_f$ , respectively. Experimentally, a linear position-sensitive detector records the exit angle  $\vartheta_f$  with respect to the surface. Simultaneously, a crystal analyzer selects the in-plane angle  $\theta_f$  of the diffracted beam. This geometry allows to picture a three-dimensional map of the reciprocal space [90].

Eventually, GIXD offers the possibility to investigate the in-plane lattice parameter and in-plane lattice distortions as they can occur in monoclinic phase.

Generally, these x-ray measurements - and in particular the latter - require good collimation of the incidence beam both in vertical and lateral direction. Moreover, chal-

lenging is the rather weak scattered x-ray signal. Therefore, it is oftentimes useful to measure with bright and high collimated x-ray beams as it is inherent in synchrotron radiation [90]. In consequence, most of the GIXD mappings presented in this thesis were recorded at synchrotron radiation facilities as the European Synchrotron (ESRF, Grenoble, France) and Bessy II (Helmholtz Center, Berlin, Germany).

The presented x-ray measurements have been performed by Dr. Martin Schmidbauer, Albert Kwasniewski, Dr. Michael Hanke and Christoph Feldt.

## Part III.

# Results & Discussion

The greater goal of the presented study is the investigation of changing ferroelectric properties in dependence on the incorporated lattice strain to learn how to perform "strain engineering". Therefore, different paths can be taken: lattice strain can be modified by varying the lattice parameter (i) of the substrate (e.g. by different rare-earth scandates) and/or (ii) of the film by changing the composition.

## 7. Theoretical Considerations

### 7.1. Calculating lattice parameter from Vegard's law

The  $K_xNa_{1-x}NbO_3$  thin films investigated in this work exhibit all an orthorhombic symmetry. Using eqs. 22-24, the pseudocubic parameters can be calculated from the former orthorhombic ones. According to Vegard's law, the pseudocubic lattice parameters of potassium sodium niobate films  $a_{pc}^{K_xNa_{1-x}NbO_3}$ ,  $b_{pc}^{K_xNa_{1-x}NbO_3}$ ,  $c_{pc}^{K_xNa_{1-x}NbO_3}$  and  $\beta_{pc}^{K_xNa_{1-x}NbO_3}$  with  $0.5 \leq x \leq 1$  can be estimated from a linear interpolation:

$$a_{pc}^{K_xNa_{1-x}NbO_3} = x \cdot a_{pc}^{KNbO_3} + (1 - x) \cdot a_{pc}^{K_{0.5}Na_{0.5}NbO_3} \quad (58)$$

$$b_{pc}^{K_xNa_{1-x}NbO_3} = c_{pc}^{K_xNa_{1-x}NbO_3} = x \cdot b_{pc}^{KNbO_3} + (1 - x) \cdot b_{pc}^{K_{0.5}Na_{0.5}NbO_3} \quad (59)$$

$$\beta_{pc}^{K_xNa_{1-x}NbO_3} = 90^\circ - \arccos \left( 1 - \frac{(a_o^{K_xNa_{1-x}NbO_3})^2}{2 (b_{pc}^{K_xNa_{1-x}NbO_3})^2} \right) \quad (60)$$

with the boundary lattice parameter [[92],[93]]:

Table 3: Orthorhombic and pseudocubic lattice parameter for  $KNbO_3$  and  $K_{0.5}Na_{0.5}NbO_3$  [[92],[93]] serving as boundary parameter for Vegard's law.

	$a_{KNbO_3}$	$b_{KNbO_3}$	$c_{KNbO_3}$	$a_{K_{0.5}Na_{0.5}NbO_3}$	$b_{K_{0.5}Na_{0.5}NbO_3}$	$c_{K_{0.5}Na_{0.5}NbO_3}$
orthorhombic	3.971 Å	5.697 Å	5.722 Å	3.940 Å	5.640 Å	5.567 Å
pseudocubic	3.974 Å	4.036 Å	4.036 Å	3.940 Å	4.000 Å	4.000 Å

## 7.2. Calculation of the strain energy density $F(\varepsilon)(\mathbf{x})$

Which energy cost is needed for the epitaxy and thus which crystallographic orientation will be favorable can be determined by the linear elasticity theory. The resulting strain energy density  $F(\varepsilon)$  indicates the effort expended to elastically distort the crystal structure. This process depends on the material characterizing stiffness tensor  $c_{ijkl}$  and the strain in both in-plane directions  $\varepsilon_{mn}$ .

$$F(\varepsilon) = \frac{1}{2} \sum_{ijkl} c_{ijkl} \varepsilon_{ij} \varepsilon_{kl} \quad (61)$$

By using the Voigt notation depicted in eq. 3 and applying symmetry considerations, the problem can be simplified. The elasticity tensor can be written as followed in case of an orthorhombic lattice:

$$c_{Voigt} = \begin{pmatrix} c_{11} & c_{12} & c_{13} & c_{14} & c_{15} & c_{16} \\ c_{21} & c_{22} & c_{23} & c_{24} & c_{25} & c_{26} \\ c_{31} & c_{32} & c_{33} & c_{34} & c_{35} & c_{36} \\ c_{41} & c_{42} & c_{43} & c_{44} & c_{45} & c_{46} \\ c_{51} & c_{52} & c_{53} & c_{54} & c_{55} & c_{56} \\ c_{61} & c_{62} & c_{63} & c_{64} & c_{65} & c_{66} \end{pmatrix} \rightarrow c_{Voigt}^{orth} = \begin{pmatrix} c_{11} & c_{12} & c_{13} & 0 & 0 & 0 \\ c_{12} & c_{22} & c_{23} & 0 & 0 & 0 \\ c_{13} & c_{23} & c_{33} & 0 & 0 & 0 \\ 0 & 0 & 0 & c_{44} & 0 & 0 \\ 0 & 0 & 0 & 0 & c_{55} & 0 \\ 0 & 0 & 0 & 0 & 0 & c_{66} \end{pmatrix} \quad (62)$$

Moreover, boundary conditions for the applied stress can be defined.

If the stress from the substrate onto the film lattice shall be calculated, the problem can be regarded as first approximation as pure interfacial effect. Hence, the following limitations should be valid [[94],[95]]: for in-plane biaxial strain the contributions  $\varepsilon_{xz}$  and  $\varepsilon_{yz}$  should be neglected. Likewise, for in-plane stress  $\sigma_{zz} = \sigma_{xz} = \sigma_{yz} = 0$  (see eq. 64) should be used. Moreover, the layer should grow epitaxially without any in-plane shearing ( $\varepsilon_{xy} = 0$ ).

The latter is an approximation for the potassium sodium niobate films under investigation. In reality, they possess monoclinic symmetry and hence a monoclinic distortion angle  $\beta$ . For  $(100)_{pc}$  oriented films,  $\beta$  lies in-plane. However, the substrates illustrated in tab. 1 have a rectangular surface. In consequence, the rectangular growth of  $K_xNa_{1-x}NbO_3$  requires an additional energy contribution to elastically distort the lattice which is not considered in the following calculations. Indeed, it was shown for  $NaNbO_3$  films of only a 1-3 nm that the monoclinic angle is forced to  $\beta \cong 0$  [96] on a  $DyScO_3$  substrate.

As a consequence, eq. 61 can be reduced to:

$$F(\varepsilon)^{orth} = \frac{1}{2} (\varepsilon_{xx}^2 c_{11} + \varepsilon_{yy}^2 c_{22} + 2\varepsilon_{xx}\varepsilon_{yy}c_{12}) \quad (63)$$

for orthorhombic films. Hereby, the strain  $\varepsilon_{ii}$  is calculated between the film lattice parameter and those of the substrate illustrated in tab. 1 according to eq. 17.

In the orthorhombic symmetry, three different orientations can exist according to the unit cell axes a,b,c differing in the out-of-plane axis. Indeed, either of these can occur in two 90° in-plane rotated variants. In consequence of the likewise changing stress applied from the substrate, the energy density  $F(\varepsilon)^{orth}$  will vary. Hence, eq. 63 allows to predict the most favorable orientation on the basis of the minimal energy density of the six possible variants.

It has to be noted, that the elastic constants are reported for KNbO<sub>3</sub> only [92], while they are not available for K<sub>x</sub>Na<sub>1-x</sub>NbO<sub>3</sub>. But since we assume similar coefficients for the K<sub>x</sub>Na<sub>1-x</sub>NbO<sub>3</sub> solid-solutions, we also refer for prediction of preferred film unit cell orientations for these materials to the coefficients of KNbO<sub>3</sub> [92].

In consequence of the discussed assumption to solve eq. 61, eq. 63 is strictly spoken only an approximation for the discussed K<sub>x</sub>Na<sub>1-x</sub>NbO<sub>3</sub> in this thesis.

The elasticity coefficients used for the calculations are depicted in tab. 4:

Table 4: Directional dependent elastic coefficients  $c_{ij}$  (GPa) of KNbO<sub>3</sub> taken from [92].

$c_{11}$	$c_{22}$	$c_{33}$	$c_{12}$	$c_{13}$	$c_{23}$
224 GPa	273 GPa	245 GPa	102 GPa	182 GPa	130 GPa

From tab. 4 the conclusion can be drawn, that KNbO<sub>3</sub> possesses different stiffnesses along the unit cell axes denoted in tab. 4 as 1,2,3 because  $c_{11} \neq c_{22} \neq c_{33}$  is valid. Consequently, the material has an inherent elastic anisotropy which has to be considered additionally to the anisotropic in-plane lattice parameter of a rare-earth scandate substrate (see tab. 1).

Furthermore, eq. 63 enables to calculate  $F(\varepsilon)^{orth}$  for every potassium concentration  $x$  yielding the functionality  $F(\varepsilon)(x)$ . The result is an  $x$ -dependent information on the preferred growth mode.

### 7.3. Calculation of the strained vertical lattice parameter $d_{\perp}^{strained}$

Within Hooke's theory, the strained vertical lattice spacing can be calculated. Taking the eq. 61 in notation 64:

$$\sigma_{ij} = \sum_{k=1}^3 \sum_{l=1}^3 c_{ijkl} \varepsilon_{kl} \quad (64)$$

and the elasticity tensor for orthorhombic media illustrated in eq. 62, yield the transformation from stress to strain:

$$\begin{pmatrix} \sigma_{xx} \\ \sigma_{yy} \\ \sigma_{zz} \\ \sigma_{yz} \\ \sigma_{xz} \\ \sigma_{xy} \end{pmatrix} = \begin{pmatrix} c_{11} & c_{12} & c_{13} & 0 & 0 & 0 \\ c_{12} & c_{22} & c_{23} & 0 & 0 & 0 \\ c_{13} & c_{23} & c_{33} & 0 & 0 & 0 \\ 0 & 0 & 0 & c_{44} & 0 & 0 \\ 0 & 0 & 0 & 0 & c_{55} & 0 \\ 0 & 0 & 0 & 0 & 0 & c_{66} \end{pmatrix} \cdot \begin{pmatrix} \varepsilon_{xx} \\ \varepsilon_{yy} \\ \varepsilon_{zz} \\ 2\varepsilon_{yz} \\ 2\varepsilon_{xz} \\ 2\varepsilon_{xy} \end{pmatrix} \quad (65)$$

If the stress results exclusively from the underlying substrate and thus by an in-plane force on the unit cell, it can be concluded that  $\sigma_{zz} = 0$ . Thus, the strain in vertical direction as a consequence of in-plane stress in an orthorhombic lattice can be calculated according to eq. 67:

$$\sigma_{zz} = 0 = c_{13} \cdot \varepsilon_{xx} + c_{23} \cdot \varepsilon_{yy} + c_{33} \cdot \varepsilon_{zz} \quad (66)$$

$$\varepsilon_{zz} = -\frac{1}{c_{33}}(c_{13} \cdot \varepsilon_{xx} + c_{23} \cdot \varepsilon_{yy}) \quad (67)$$

The strained vertical lattice parameter  $d_{\perp}^{\text{strained}}$  can be calculated from the unstrained, bulk lattice parameter  $d_{\perp}$  with eq. 68:

$$d_{\perp}^{\text{strained}} = (1 + \varepsilon_{zz}) \cdot d_{\perp} \quad (68)$$

As discussed in chapter 7.2, the elastic constants  $c_{ijkl}$  are listed in the literature only for  $\text{KNbO}_3$  [92], but we assume similar coefficients for the  $\text{K}_x\text{Na}_{1-x}\text{NbO}_3$  solid-solutions. As a result, the parameter listed in tab. 4 were taken for the calculation of the strained vertical lattice value.

## 7.4. Calculation of the misfit strain-misfit strain phase diagram for $\text{KNbO}_3$

As already described in chapter 1.3, several different domains can appear in a ferroelectric material. For pure potassium niobate, a prediction from Bai and Ma [3] exists, that illustrates the most favorable domain state in dependence of the biaxial misfit strain (depicted in fig. 10). However, comparing the experimental results to this theoretical predictions yielded oftentimes no agreement. Probably, the transitions points

were plotted with major increment. Hence, the calculation is too rough. Therefore, I calculated and plotted the diagram with minor step size.

The basis of the former calculations is Gibbs free energy in the framework of the Landau-Ginzburg-Devonshire theory as discussed in chapter 1.2. Due to the fact that the film is clamped to a bulky substrate, parts of the energy functions do not longer describe a free stranding material. In consequence, a Legendre transformation of  $G$  has to be calculated [[22],[97]]. In contrast to the initial function of  $G$ , the modified thermodynamic potential  $\tilde{G}$  depends on different variables compared to eq. 2. These changes are denoted by the index \* whereby some of them correlate directly with the biaxial strain  $\varepsilon_{xx}$  and  $\varepsilon_{yy}$  [98] as denoted by the index \*\* on the respective summand [98].

$$\begin{aligned}
\Delta\tilde{G} = & \alpha_1^{**}P_1^2 + \alpha_2^{**}P_2^2 + \alpha_3^{**}P_3^2 + \alpha_{11}^*(P_1^4 + P_2^4) + \alpha_{33}^*P_3^4 + \alpha_{13}^*(P_1^2 + P_2^2)P_3^2 + \alpha_{12}^*P_1^2P_2^2 \\
& + \alpha_{111}(P_1^6 + P_2^6 + P_3^6) + \alpha_{112}[P_1^4(P_2^2 + P_3^2) + P_2^4(P_1^2 + P_3^2) + P_3^4(P_2^2 + P_1^2)] \\
& + \alpha_{123}(P_1^2P_2^2P_3^2) + \alpha_{1111}(P_1^8 + P_2^8 + P_3^8) \\
& + \alpha_{1112}[P_1^6(P_2^2 + P_3^2) + P_2^6(P_1^2 + P_3^2) + P_3^6(P_2^2 + P_1^2)] \\
& + \alpha_{1122}(P_1^4P_2^4 + P_1^4P_3^4 + P_2^4P_3^4) + \alpha_{1123}(P_1^4P_2^2P_3^2 + P_2^4P_1^2P_3^2 + P_3^4P_1^2P_2^2) \\
& + \frac{s_{11}(\varepsilon_{xx}^2 + \varepsilon_{yy}^2) - 2s_{12}\varepsilon_{xx}\varepsilon_{yy}}{2(s_{11}^2 - s_{12}^2)}
\end{aligned} \tag{69}$$

To obtain a misfit strain-misfit strain phase diagram,  $\tilde{G}$  has to be minimized in respect to the respective polarization component to determine the equilibrium thermodynamic state of the thin film. In detail, that means that for every strain configuration  $(\varepsilon_{xx}, \varepsilon_{yy})$  the minimum minimum has to be calculated with regard to  $P_1$ ,  $P_2$  and  $P_3$ . This global minimum can then be compared to the equilibrium states that may occur in thin films [[3],[24],[99]]:

(i) p phase ( $P_1 = P_2 = P_3 = 0$ ); (ii)  $a_1$  phase ( $P_1 \neq 0$  and  $P_2 = P_3 = 0$ ); (iii)  $a_2$  phase ( $P_2 \neq 0$  and  $P_1 = P_3 = 0$ ); (iv) c phase ( $P_3 \neq 0$  and  $P_1 = P_2 = 0$ ); (v)  $a_1a_2$  phase ( $P_1 \neq 0$ ,  $P_2 \neq 0$  and  $P_3 = 0$ ); (vi)  $a_1c$  or  $M_c$  phase ( $P_1 \neq 0$ ,  $P_3 \neq 0$  and  $P_2 = 0$ ); (vii)  $a_2c$  or  $M_c$  phase ( $P_2 \neq 0$ ,  $P_3 \neq 0$  and  $P_1 = 0$ ) and (viii) r or  $M_A$  phase ( $P_1 \neq 0$ ,  $P_2 \neq 0$  and  $P_3 \neq 0$ ).

One possibility is to plot the transition points between the equilibrium phases to separate the favored ferroelectric states as depicted in fig. 22a for the material constants

of  $\text{KNbO}_3$  [3] and a temperature of  $T = 25^\circ\text{C}$ .

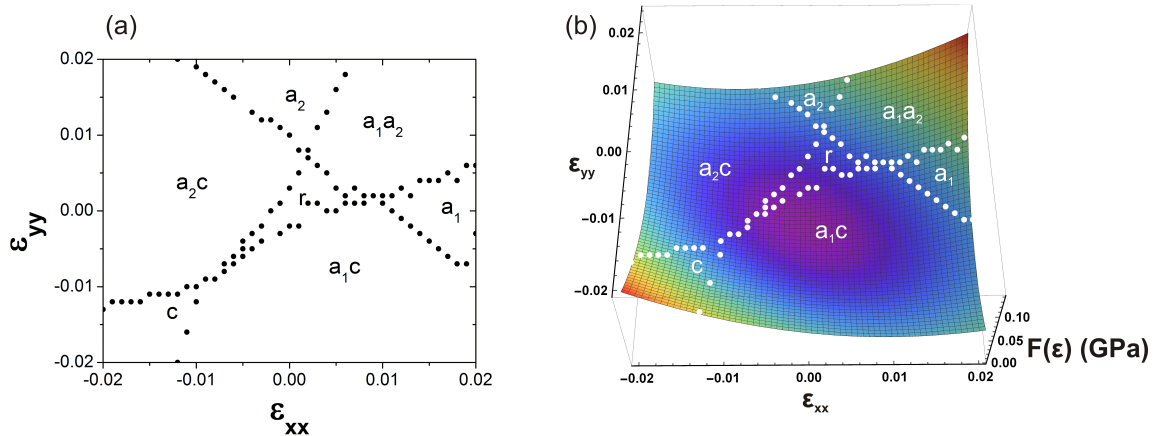


Figure 22: (a) Misfit strain - misfit strain phase diagram of single-domain  $\text{KNbO}_3$  thin films calculated for  $T = 25^\circ\text{C}$ . (b) Multilayer plot consisting of the elastic strain energy density  $F(\varepsilon)$  for  $\text{KNbO}_3$  in dependence of the biaxial strain  $\varepsilon_{ij}$  together with the phase transition points calculated according to eq. 69.

From consideration 63 further predictions can be inferred. It immediately provides information about the energy density surface in dependence of the biaxial strain  $F(\varepsilon_{xx}, \varepsilon_{yy})$ . If moreover the stability regions for individual ferroelectric domain are calculated numerically according to eq. 69, a multi-dimensional plot can be derived as shown in fig. 22b. Herefrom, it can be concluded that the strain as discrete variable alone may not be the only decisive parameter whether a domain configuration will be stable and occur. Rather the elastic energy needed to distort the material under an applied stress has to be considered likewise.

Meanwhile, it shows impressively, that monoclinic phases as they would be highly desirable because of the high piezoresponses (see chapter 2.5) are energetically favorable in  $\text{KNbO}_3$ .

To summarize chapter 7, the elastic deformations enforced during epitaxial growth dictate the crystal film symmetry and thereby the functional properties. Consequently, the substrate stress induced distortions in the film unit cell have to be understood for a precise prediction of the ferroelectric ordering. This way, strain engineering can become a sophisticated tool for the targeted fabrication of functional thin films.

In the following,  $\text{K}_x\text{Na}_{1-x}\text{NbO}_3$  films were grown on (001)  $\text{SrTiO}_3$ , (110)  $\text{DyScO}_3$ , (110)  $\text{TbScO}_3$ , (110)  $\text{GdScO}_3$  and (110)  $\text{NdScO}_3$  single-crystalline substrates. As a result of varying misfit strain, the ferroelectric domain structure changes drastically as can be seen in fig. 23. For example, although the change of the average strain is rather

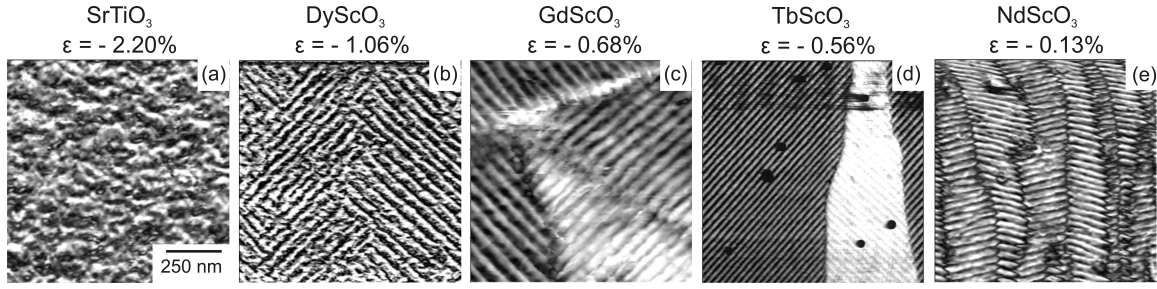


Figure 23: Lateral PFM amplitude measurements of  $K_xNa_{1-x}NbO_3$  on (a) (001)  $SrTiO_3$ , (b) (110)  $DyScO_3$ , (c) (110)  $TbScO_3$ , (d) (110)  $GdScO_3$  and (e) (110)  $NdScO_3$  single-crystalline substrates.  $\varepsilon$  is the average in-plane strain.

minor between films on  $TbScO_3$  and  $NdScO_3$ , the domain pattern reveals enormous differences. The reasons has to be associated to the energy density situation as they represent different strain states. Therefore, to verify the theory and to eventually prove the possibility to systematically adjust the ferroelectric properties, these both examples on  $TbScO_3$  and  $NdScO_3$  should be discussed in detail in chapter 8 and 9, respectively.

## 8. Uniaxial strain: $\text{K}_{0.75}\text{Na}_{0.25}\text{NbO}_3$ films on (110)

### $\text{TbScO}_3$

In the  $\varepsilon(x)$  diagram 24a the film composition with  $x = 0.75$  on (110)  $\text{TbScO}_3$  (TSO) determines an unique point. The in-plane lattice parameter of the film calculated according to eq. 58 to  $a_{\text{pc}} = 3.957 \text{ \AA}$  and  $c_{\text{pc}} = 4.018 \text{ \AA}$  can be arranged on the (110)  $\text{TbScO}_3$  surface with its  $a_{\text{pc}} = 2 \times 3.958 \text{ \AA}$  and  $b_{\text{pc}} = 2 \times 3.959 \text{ \AA}$  lattice parameters this way that the strain is almost zero along the  $[001]_{\text{TSO}}$  direction and  $-1.47\%$  compressive for the orthogonal  $[1\bar{1}0]_{\text{TSO}}$  direction as it is illustrated in fig. 24a. In the end, it marks the unique possibility to investigate uniaxial strain and was therefore discussed in detail [100].

From the elastic strain energy density plotted in fig. 24b for films on  $\text{TbScO}_3$  in dependence of the potassium content  $x$ , it becomes obvious that for  $x = 0.75$  a  $(001)_{\text{pc}}$  orientation is the preferred growth mode.

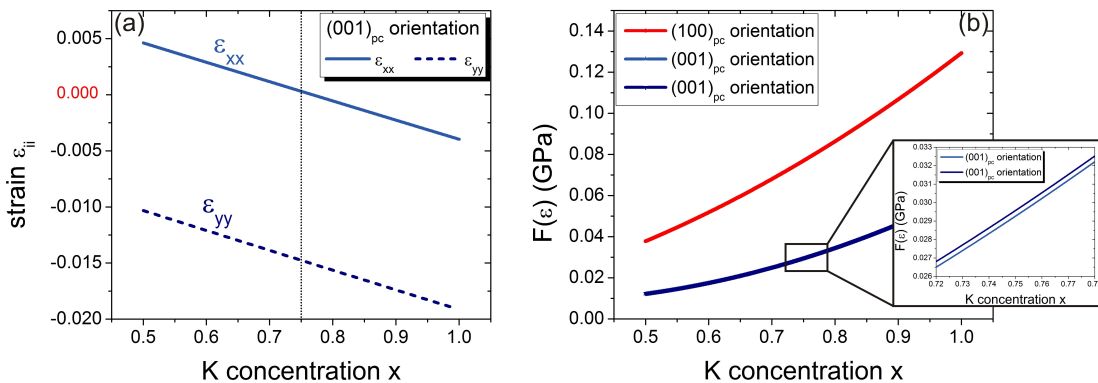


Figure 24: (a) Strain in dependence of the potassium concentration  $x$  in the solid solution  $\text{K}_x\text{Na}_{1-x}\text{NbO}_3$  for  $0.5 \leq x \leq 1$  on  $\text{TbScO}_3$  substrate. The composition with  $x = 0.75$  is marked with a dotted line. (b) Estimation of the elastic strain energy density  $F(\varepsilon)$  for four possible orientations of  $\text{K}_x\text{Na}_{1-x}\text{NbO}_3$  on  $\text{TbScO}_3$  substrate versus potassium content  $x$  for  $0.5 \leq x \leq 1$ . As inset a magnification of the elastic energy density for both  $90^\circ$  rotated  $(001)_{\text{pc}}$  variants in the vicinity of  $x = 0.75$  is shown.

The atomic force microscopy (AFM) was used to study the surface topography in ambient air shown in fig. 25a. The AFM image of the film illustrates very smooth surfaces with an average root mean square surface roughness of 0.3 nm. To determine the growth mode, a detailed thickness series should have been performed. However, from the AFM image (fig. 25a) it can be suggested that no step flow growth occurred

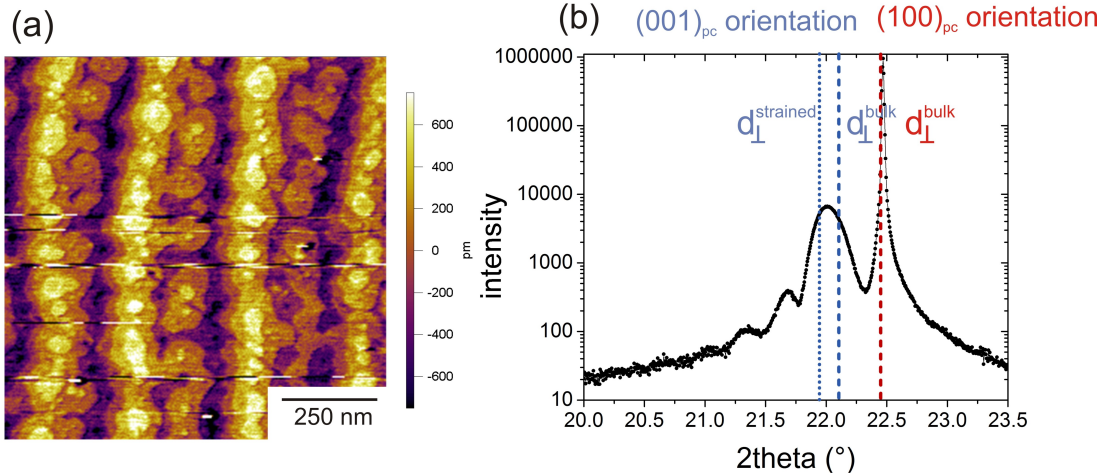


Figure 25: (a) Surface morphology of a respective film on a  $(1 \times 1) \mu\text{m}^2$  scale. (b)  $\theta - 2\theta$  HRXRD pattern of a  $\text{K}_{0.75}\text{Na}_{0.25}\text{NbO}_3$  films on  $(110)$   $\text{TbScO}_3$  in the range from  $2\theta = 20^\circ - 23.5^\circ$ . The red and blue dashed lines indicate the nominal angular position of the bulk vertical lattice parameter in case of an  $(100)_{\text{pc}}$ - and  $(001)_{\text{pc}}$  orientation, respectively, for  $\text{K}_{0.75}\text{Na}_{0.25}\text{NbO}_3$ . The blue dotted line indicates the nominal angular position of the strained vertical lattice parameter  $d_{\perp}^{\text{strained}}$  for a  $(001)_{\text{pc}}$  orientation in case of  $\text{K}_{0.75}\text{Na}_{0.25}\text{NbO}_3/\text{TbScO}_3$ .

but rather a transition from 2D growth on each step to island growth.

In fig. 25b the  $\theta - 2\theta$  HRXRD pattern of the  $\text{K}_{0.75}\text{Na}_{0.25}\text{NbO}_3$  film around the  $(110)_{\text{TbScO}_3}$  Bragg reflection of the orthorhombic  $\text{TbScO}_3$  substrate is shown in the range from  $2\theta = 20^\circ - 23.5^\circ$ . The diffraction measurement reveals a sharp substrate peak around  $2\theta = 22.44^\circ$  and a single film peak appearing at about  $2\theta = 21.99^\circ$ . A quantitative analysis according to the procedure presented in eq. 56 and 57 yields a vertical lattice parameter of  $d_{\perp} = 4.040 \text{ \AA}$  and film thickness  $t = 29 \text{ nm}$ . To clarify the strain state, the strained vertical lattice spacing of the  $(001)_{\text{pc}}$  orientated  $\text{K}_{0.75}\text{Na}_{0.25}\text{NbO}_3$  phase was estimated from eq. 67 to  $d_{\perp}^{\text{strained}} = 4.047 \text{ \AA}$  and transferred into the  $\theta - 2\theta$  HRXRD pattern in fig. 25b as dotted line. In regard of the uncertainty arising from the calculation e.g. by taking the elastic constants of  $\text{KNbO}_3$  instead of those from  $\text{K}_{0.75}\text{Na}_{0.25}\text{NbO}_3$ , it can be concluded that the film contribution matches rather exactly the theoretical value. This demonstrates that the film has been grown under compressive strain with indeed  $(001)_{\text{pc}}$ -orientation, confirming the energetic considerations presented in fig. 24b.

Evaluating the strain state along both substrate directions from fig. 24a and intro-

ducing the values as black circles in the strain-phase diagram in fig. 26a yields the prediction of monoclinic  $M_c$  domains for a fully strained film. In the monoclinic phase,

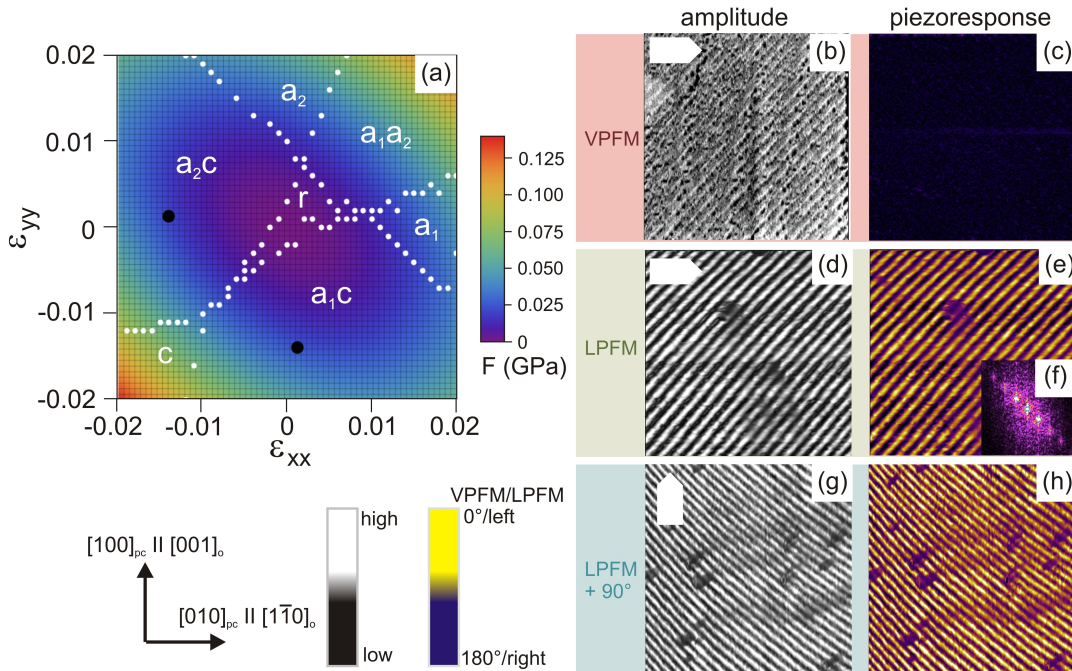


Figure 26: (a) 3D plot of the elastic strain energy density  $F(\varepsilon)$  for  $K_xNa_{1-x}NbO_3$  in dependence of the biaxial strain  $\varepsilon_{xx}$  and  $\varepsilon_{yy}$ . On the energy landscape the strain-phase diagram presented in fig. 22a for  $KNbO_3$  was plotted. The filled black circles indicate the strain state in  $K_{0.75}Na_{0.25}NbO_3$  on a  $(110)$   $TbScO_3$  substrate. PFM measurements of a  $K_{0.75}Na_{0.25}NbO_3/TbScO_3$  film, picture size  $(1 \times 1) \mu m^2$ : vertical amplitude (b) and piezoresponse PR (c). (d)-(h) are lateral measurements whereby (d) and (g) show amplitude images and (e) and (h) the piezoresponse images. The cantilever orientation is illustrated in the upper left of part of the amplitude images. (f) 2D-FFT of the lateral amplitude image (d).

the electric polarization vector is not constrained to highly symmetric crystallographic directions as it is the case for rhombohedral, orthorhombic or tetragonal phases. In contrast, the polarization can rotate unhamperedly within the mirror plane of the monoclinic unit cell  $[101]$ . In the special case of  $M_c$  domains this means the  $\{100\}_{pc}$  planes [5].

The VPFM and LPFM measurements are illustrated in fig. 26b-h separated in amplitude and piezoresponse signal both for a sample area size of  $(1 \times 1) \mu m^2$ . Stripe domains become visible in the vertical amplitude in fig. 26b but no resulting phase contrast can be detected (see fig. 26c). Eventually, such a missing  $180^\circ$  phase shift is not unusual and can be caused by several phenomena:

- i One explanation could be, that all polarization vectors are aligned equally and hence a vertical monodomain has formed. But, in this case, a complete up or down alignment should result in a charged surface and interface. Consequently, it is energetically not favorable.
- ii During the PFM mode, a drive voltage in the range of  $V_{\text{drive}} = 0.2 - 1$  V is applied to a tip with an effective tip radius of  $r \approx 30$  nm. Finally, enormous electric fields result that can lead to a strong electrostatic contribution to the signal misrepresenting the vertical response as discussed in chapter 5.1.
- iii A third effect that can not be neglected in PFM measurements is that the pressure of the tip in contact mode leads immediately to a mechanically induced switching process and hence to a poling of the film.

In principle, all three explanations could be responsible for the missing phase contrast in fig. 26. However, a buckling effect [102] can be neglected, since the cantilever axis is not parallel to the stripes.

In the end, from the vertical images 26b,c it can be concluded that the polarization exhibits a vertical component but its orientation can not be determined.

Contrariwise, in the lateral mode presented in fig. 26d,e well pronounced, almost perfectly ordered stripe domains arise. The phase signal shown in fig. 26e depicts an alternating left - and rightwards torsion of the cantilever manifesting a periodical change of the in-plane polarization component. The same lateral behavior can be detected on a  $90^\circ$  rotated sample illustrated in fig. 26g,h. The periodicity of the stripe domains can be evaluated to  $(50 \pm 1)$  nm.

In both modes, the domain walls are aligned along  $[1\bar{1}\bar{2}]_{\text{TSO}}$ . Measurements on a larger scale reveal the perfectness as the straight walls are running along microns. The proof is given in the periodic arrangement of spots in the 2D-FFT image of the lateral amplitude signal in fig. 26f. This effect can be attributed to both the defect-poor growth mode and the high oxygen partial pressure in the MOCVD process. As a result, the films have a low defect density leading to ferroelectric pattern ranging from the nano - to the micron scale without any domain wall bending around defect cluster as it was theoretical predicted [[103],[104]] and experimentally confirmed [[96],[105]] for other systems. This perfectness is unique and was rarely achieved before.

From the PFM measurements we conclude that the  $\text{K}_{0.75}\text{Na}_{0.25}\text{NbO}_3$  films on (110)  $\text{TbScO}_3$  result in a ferroelectric pattern with both a vertical and a lateral polarization component. Consequently, four in-plane domain arrangements are possible as can be seen in fig. 27a-d: two  $90^\circ$  (figs. 27a,b) and two  $180^\circ$  configurations (figs. 27c,d). However, only two of them (figs. 27a and c) fulfill the requirement of uncharged do-

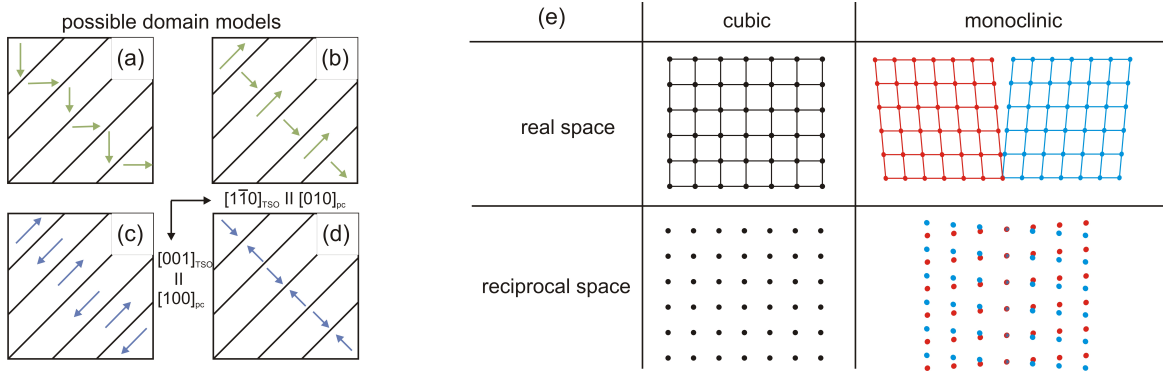


Figure 27: Possible in-plane arrangement of the electric polarization vector for stripe domains: (a), (b)  $90^\circ$  arrangement, (c), (d)  $180^\circ$  pattern. (e) Schematic presentation of the diffraction pattern in reciprocal space in case of a cubic and monoclinic unit cell in real space.

main walls. In order to distinguish between the remaining two opportunities, in-plane GIXD and out-of-plane HRXRD experiments were performed to get detailed information about the film lattice structure. Hereby, the questions have to be answered in which orientation the film is grown and if indeed monoclinic domains occur as predicted in fig. 24c. As a proof of monoclinic film symmetry a respective lattice splitting has to be detected as it is schematically illustrated for real and reciprocal space for cubic and monoclinic symmetry in fig. 27e. Depending on the film orientation, thus either  $(100)_{\text{pc}}$  or  $(001)_{\text{pc}}$  orientation, the according splitting appears in the in-plane or out-of-plane reciprocal space maps, respectively.

For the following discussion, it should be claimed that in reference to the substrate lattice parameter, the x-ray data are denoted in the orthorhombic notation. For the in-plane characterization, reciprocal space maps were recorded in the vicinity of the  $(008)_{\text{Tso}}$  (fig. 28a),  $(4\bar{4}0)_{\text{Tso}}$  (fig. 28b) and  $(2\bar{2}4)_{\text{Tso}}$  (fig. 28c) Bragg reflections. In order to guard against misunderstandings, it should be mentioned that the experimental resolution element indicated in fig. 28a-c in every left bottom corner leads to a slight blurring of the diffraction pattern although the film is almost perfectly ordered.

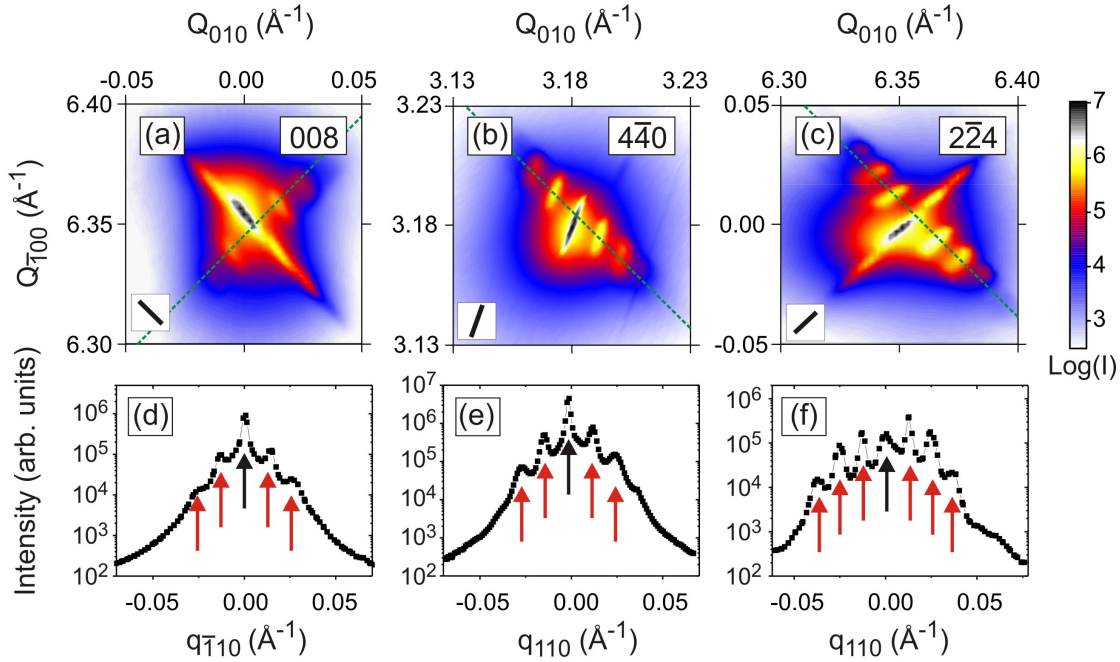


Figure 28: GIXD intensity distribution patterns for the (a) (008)<sub>TSO</sub>, (b) (440)<sub>TSO</sub> and (c) (224)<sub>TSO</sub> in-plane reciprocal lattice points of the substrate. (d) to (f) Plots of the corresponding line scans along the green dashed lines in part (a), (b) and (c), respectively. Black arrows mark the positions of the main film peaks, while red arrows indicate the satellite peaks. Adapted from [100].

In all measured Bragg reflections, a distinct central peak emerges that can be identified as the film peak. This film peak reveals no in-plane peak splitting as it is schematically drawn in fig. 27b. Consequently, no monoclinic in-plane distortion exists. Furthermore, periodic satellite peaks along  $[\bar{1}10]_{\text{pc}}$  and  $[110]_{\text{pc}}$  occur in the proximity of the central peaks for all presented in-plane reciprocal lattice points. Evaluation of the distance of these satellites by means of a line scans along the dashed green lines in figs. 28a,b,c and plotting them in fig. 28d,e,f, respectively, reveals an equidistant appearance. In addition, the spacing is identical for all Bragg reflections. Herefrom, it can be concluded that the satellites are caused by a positional correlation. For the real space, this can be translated into identical film in-plane lattices in neighboring domains independent of the domain state. Thus, they are due to the periodical formation of the ferroelectric domain pattern along the  $[110]_{\text{pc}} = [1\bar{1}\bar{2}]_{\text{TSO}}$  directions in the film plane. Transferring the distance between the satellite peaks in the reciprocal space of  $\Delta q = 0.0129 \text{\AA}^{-1}$  into the real space yields a periodicity of the domain pattern of  $(49 \pm 1) \text{ nm}$ , which is in excellent agreement with the PFM value of  $(50 \pm 1) \text{ nm}$ .

Due to the fact, that the monoclinicity could not be proven in the in-plane GIXD

data, further out-of-plane measurements are needed. The reciprocal space maps in the vicinity of the  $(44\bar{4})_{\text{TSO}}$ ,  $(42\bar{2})_{\text{TSO}}$ ,  $(422)_{\text{TSO}}$ ,  $(220)_{\text{TSO}}$  and  $(620)_{\text{TSO}}$  Bragg reflection points are plotted in figs. 29a-e, respectively. For a better illustration of their arrangement and the relationship to the pseudocubic film notation, the corresponding  $(hkl)$  of the in-plane reciprocal lattice points are depicted schematically in fig. 29i by red circles. The first result is that the in-plane component of the reciprocal lattice vectors

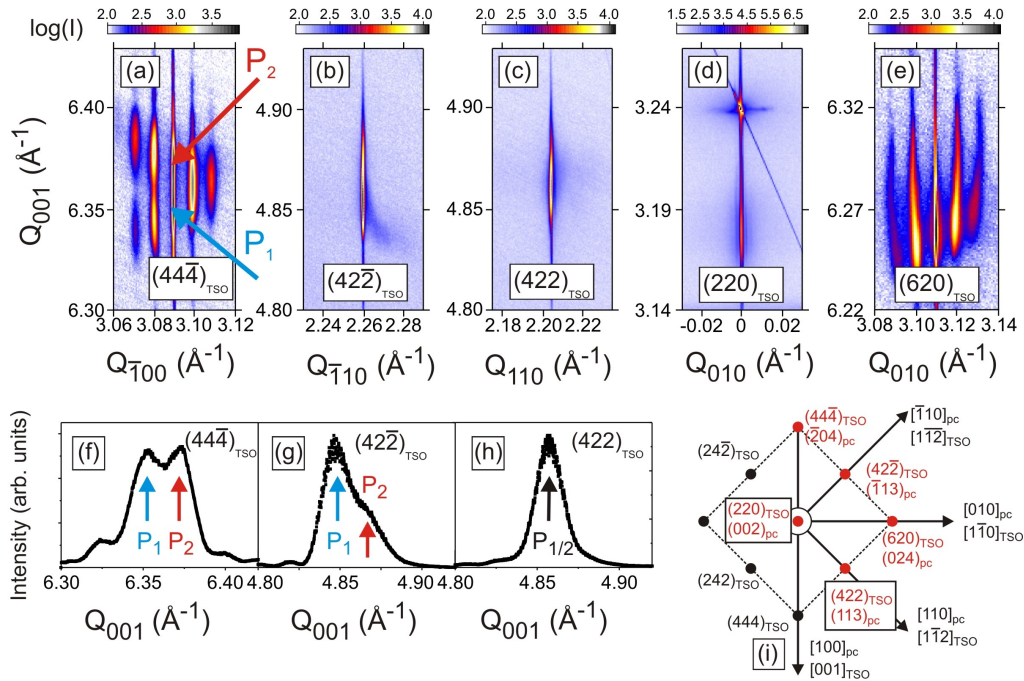


Figure 29: X-ray reciprocal space maps of the (a)  $(44\bar{4})_{\text{TSO}}$ , (b)  $(42\bar{2})_{\text{TSO}}$ , (c)  $(422)_{\text{TSO}}$ , (d)  $(220)_{\text{TSO}}$  and (e)  $(620)_{\text{TSO}}$  Bragg peaks. In the lower image the line scans along  $Q_{001}$  in the (f)  $(44\bar{4})_{\text{TSO}}$ , (g)  $(42\bar{2})_{\text{TSO}}$  and (h)  $(422)_{\text{TSO}}$  mappings are plotted. (i) A sketch of the in-plane arrangement of reciprocal lattice points around the  $(220)_{\text{TSO}}$  diffraction point. The recorded reciprocal space maps are indicated by red circles and additionally referred to the pseudocubic notation. Adapted from [100].

of the film equals that of the substrate in all measured Bragg reflection. Herefrom, it can be denoted that the film lattice is grown fully matched to the in-plane dimensions of the substrate unit cell.

Moreover, equidistant satellite peaks of the film contribution appear in the asymmetric  $(44\bar{4})_{\text{TSO}}$  and  $(620)_{\text{TSO}}$  mappings. The examination of the satellite spacings and converting them into real space yield a domain periodicity of  $(48 \pm 1)$  nm. This result is in full accordance to the values obtained from GIXD and PFM measurements.

Furthermore, the film peak substructure was investigated in detail by line scans along  $Q_{001}$  as they are presented in fig. 29f-h. The Bragg reflections around the  $(42\bar{2})_{\text{TSO}}$ ,

$(422)_{\text{TSO}}$  and  $(220)_{\text{TSO}}$  do not show any film peak splitting. Hence, here only one single film peak exists. In contrast, the  $(44\bar{4})_{\text{TSO}}$ ,  $(42\bar{2})_{\text{TSO}}$  and  $(620)_{\text{TSO}}$  reciprocal space maps reveal a vertical splitting of the film peak as it should be indicated exemplarily by arrows in fig. 29a. In consequence, the film lattice is indeed monoclinically distorted in out-of-plane direction.

How these appearances of splitting and single film peaks can be summarized into a structural model to obtain the domain type, should be examined in the following.

A structural model is presented in fig. 30a. The black cube displays the undistorted,

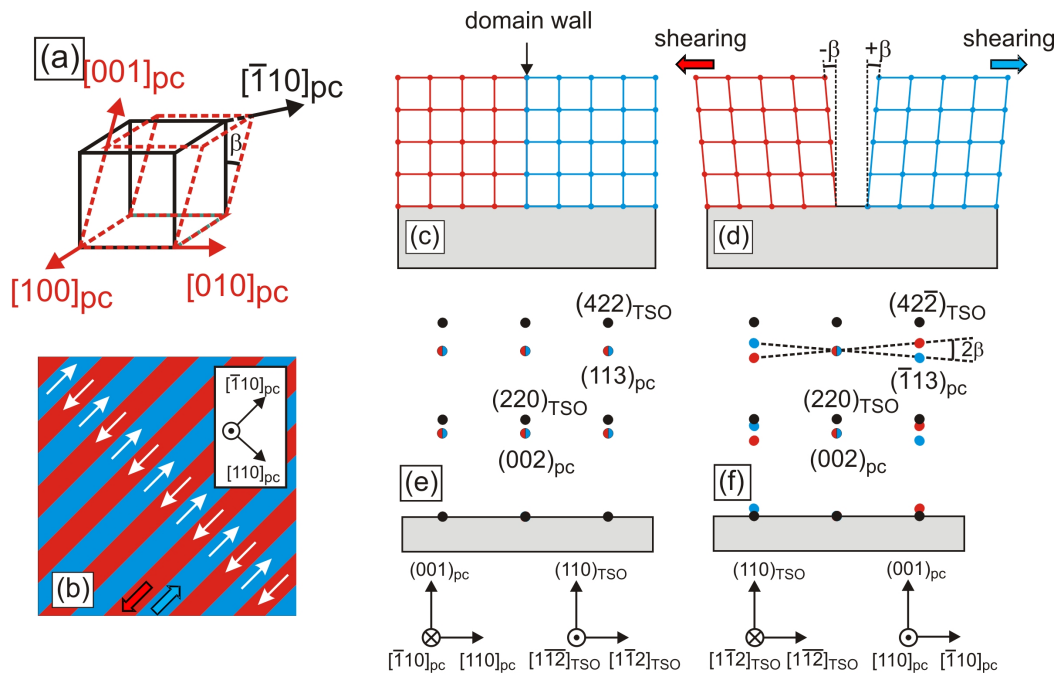


Figure 30: (a) View on an unstrained (black) and a monoclinically distorted (red) pseudocubic unit cell. For a better understanding, the monoclinic shearing angle  $\beta$  is illustrated in an exaggerated manner. (b) Schematic illustration of the domain pattern in top view with white arrows denoting the in-plane component of the polarization vector. (c), (d) Cross-sectional views of the monoclinically distorted pseudocubic unit cells along the  $[\bar{1}10]_{\text{pc}}$  and  $[110]_{\text{pc}}$  directions, respectively. For (b) – (d) the shearing direction of unit cells in the respective domains is indicated with bold red and blue arrows. (e), (f) Transformation of the cross-sectional views from (c) and (d) into reciprocal space. Black and blue/red circles indicate the reciprocal lattice points of the substrate and the film, respectively, in accordance to the color code in fig. 27e. Adapted from [100].

pseudocubic unit cell. The observed peaks splittings can be understood this way that pseudocubic unit cells of the films are sheared along the  $\pm[110]_{\text{pc}}$  direction, while the rectangular in-plane symmetry of the unit cell is preserved as illustrated by red dashed

lines.

Furthermore, the occurrence of satellite peaks only in the case of the  $(44\bar{4})_{\text{TSO}}$  and  $(620)_{\text{TSO}}$  Bragg reflection points indicate that the shearing of the film unit cell has to be in  $[\bar{1}\bar{1}0]_{\text{pc}}$  direction. Simultaneously, unit cells with the opposite shearing along  $\pm[\bar{1}\bar{1}0]_{\text{pc}}$  have to exist. For illustration of the effect, a cubic unit cell is sheared parallel to the film plane. The involving distortion is transferred from real space - depicted in figs. 30c,d - into reciprocal space in figs. 30e,f. Hereby, figs. 30c,d enable a view on the cross-section in the  $[110]_{\text{pc}}$  and  $[\bar{1}\bar{1}0]_{\text{pc}}$  directions, respectively. For a better discrimination, the red and blue color code imply a shearing of the unit cell by an angle  $+\beta$  and  $-\beta$ , respectively. A monoclinic distortion in the real lattice as shown in fig. 30d leads to a splitting of the film contribution into red and blue circles in the reciprocal space exactly for the above mentioned Bragg points as can be seen in fig. 30f. Simultaneously, for the chosen geometry in fig. 30d the scattering plane is perpendicular to the direction of domain periodicity. Consequently, the lateral domain periodicity can not be detected preventing satellite reflections in the  $(42\bar{2})_{\text{TSO}}$  diffraction pattern. As a result of a distortion along  $\pm[\bar{1}\bar{1}0]_{\text{pc}}$ , the unit cell meshes along the  $(001)_{\text{pc}}$  planes are still rectangular (fig. 30c). In contrast, for the opposite direction the unit cell meshes in the  $(110)_{\text{pc}}$  planes form parallelograms with angles  $90^\circ \pm \beta$  (fig. 30d).

The monoclinic angle  $\beta$  can be evaluated directly from the vertical peak splitting  $2\Delta Q_{001}$  using the equation:

$$\tan \beta = \frac{\Delta Q_{001}}{Q_{\parallel}} \quad (70)$$

whereby  $Q_{\parallel}$  is the horizontal component of the scattering vector  $Q_{\text{hkl}}$  in the  $[\bar{1}\bar{1}0]_{\text{pc}}$  direction. The results are presented in tab. 5.

Table 5: Measured  $Q_{001}$  and  $Q_{\parallel}$  values and calculated monoclinic distortion angle  $\beta$  for the  $(44\bar{4})_{\text{TSO}}$ ,  $(620)_{\text{TSO}}$  and  $(42\bar{2})_{\text{TSO}}$  Bragg reflection.

	$(44\bar{4})_{\text{TSO}}$	$(620)_{\text{TSO}}$	$(42\bar{2})_{\text{TSO}}$
$2\Delta Q_{001}$ ( $\text{\AA}^{-1}$ )	0.0210	0.0193	0.0190
$Q_{\parallel}$ ( $\text{\AA}^{-1}$ )	2.19	2.20	2.26
$\beta$	$(0.27 \pm 0.02)^\circ$	$(0.25 \pm 0.02)^\circ$	$(0.24 \pm 0.02)^\circ$

As a result of tab. 5, the averaged monoclinic angle can be calculated to  $\beta_{\text{film}} = (0.26 \pm 0.02)^\circ$  which is slightly below  $\beta_{\text{bulk}} = 0.30^\circ$  for bulk  $\text{K}_{0.75}\text{Na}_{0.25}\text{NbO}_3$ . The discrepancy can be understood in terms of elastic relaxation of the film lattice: the monoclinic  $\beta_{\text{film}}$  angle increases with increasing film thickness as it was former discussed

for  $\text{NaNbO}_3$  films on  $\text{DyScO}_3$  and  $\text{TbScO}_3$  single crystalline substrates [[96],[106]].

Combining the structural and the electrical measurements yield the following domain model. The lateral PFM shows a distinct phase contrast between adjacent domains (see fig. 26e). According to the x-ray data, these neighboring domains are formed by unit cells with the opposite shearing along  $\pm[1\bar{1}0]_{\text{pc}}$ . Because the unit cell distortion is different by  $180^\circ$  the electrical polarization has to change likewise alternately by  $180^\circ$ . This model is shown in fig. 30b in plane view. Regarding the domain arrangements in fig. 27, the model confirms variant c in fig. 27. In combination with the vertical response, the conclusion is drawn that the electrical polarization is located within the  $\{110\}_{\text{pc}}$  planes. In regard to the literature [5], the domain pattern is described by monoclinic  $M_A$  or  $M_B$  domains, with periodically arranged domain walls along the  $\pm[110]_{\text{pc}}$  direction and a periodicity of averaged 50 nm.

In order to distinguish between the two monoclinic phases, the ratio between the out-of-plane and in-plane (pseudocubic) lattice parameters is decisive [107]:

**i**  $a_{\text{pc}} > c_{\text{pc}}$  and  $b_{\text{pc}} > c_{\text{pc}}$  means tensile stress and result in  $M_B$  domains.

**ii**  $a_{\text{pc}} < c_{\text{pc}}$  and  $b_{\text{pc}} < c_{\text{pc}}$  refers to compressive strain and  $M_A$  domains.

In the case of  $\text{K}_{0.75}\text{Na}_{0.25}\text{NbO}_3$ , films are grown epitaxially under compressive in-plane strain on the  $\text{TbScO}_3$  substrate with in-plane lattice parameters equal to the those of the substrate of  $a_{\text{pc}} = 3.959 \text{ \AA}$  and  $b_{\text{pc}} = 3.960 \text{ \AA}$ . As a result of strain, the out-of-plane lattice parameter amounts to  $c_{\text{pc}} = 4.040 \text{ \AA}$ . In consequence,  $a_{\text{pc}} < c_{\text{pc}}$  and  $b_{\text{pc}} < c_{\text{pc}}$  and we conclude that the observed monoclinic phase is a  $M_A$  phase.

Interestingly, the x-ray results predict a coexistence of both  $(001)_{\text{pc}}$ -orientations because the evaluation of the RSM in the vicinity of the  $(4\bar{4}0)_{\text{TbScO}_3}$  in-plane reciprocal lattice point reveals equidistant satellite peaks in both  $\pm[1\bar{1}0]_{\text{pc}}$  directions.

Prospective, the following notation should be used for further discussion: the in-plane film orientation with  $[100]_{\text{pc}}||[001]_{\text{TbScO}_3}$  and  $[010]_{\text{pc}}||[1\bar{1}0]_{\text{TbScO}_3}$  will be referred as  $0^\circ$  variant and the  $90^\circ$  rotated variant with  $[010]_{\text{pc}}||[001]_{\text{TbScO}_3}$  and  $[100]_{\text{pc}}||[1\bar{1}0]_{\text{TbScO}_3}$  will be noted as  $90^\circ$  variant.

But, the experimental intensity of the satellite peaks of the  $90^\circ$  variant is about one order of magnitude lower than that of the  $0^\circ$  variant. Surprisingly, they exhibit the same periodicity as those in  $\pm[110]_{\text{pc}}$  direction.

From the discussed model in fig. 27c the deduction can be drawn that the domain wall

alignment has to be collinear with the shearing direction of the pseudocubic unit cell. This implies that a  $90^\circ$  in-plane rotation of the  $(001)_{\text{pc}}$  film orientation should lead to a likewise  $90^\circ$  in-plane rotation of the stripe domains.

Indeed, the x-ray diffraction results could be confirmed by recording several LPFM images at different film positions. A  $90^\circ$  rotated domain variant with domain walls running along the  $\pm[1\bar{1}2]_{\text{TSO}}$  direction was found in rather few cases. One example is shown in fig. 31, where the  $90^\circ$  rotated variant is visible as a bright bundle.

The reason for the uneven appearance of both variants can be found by using the

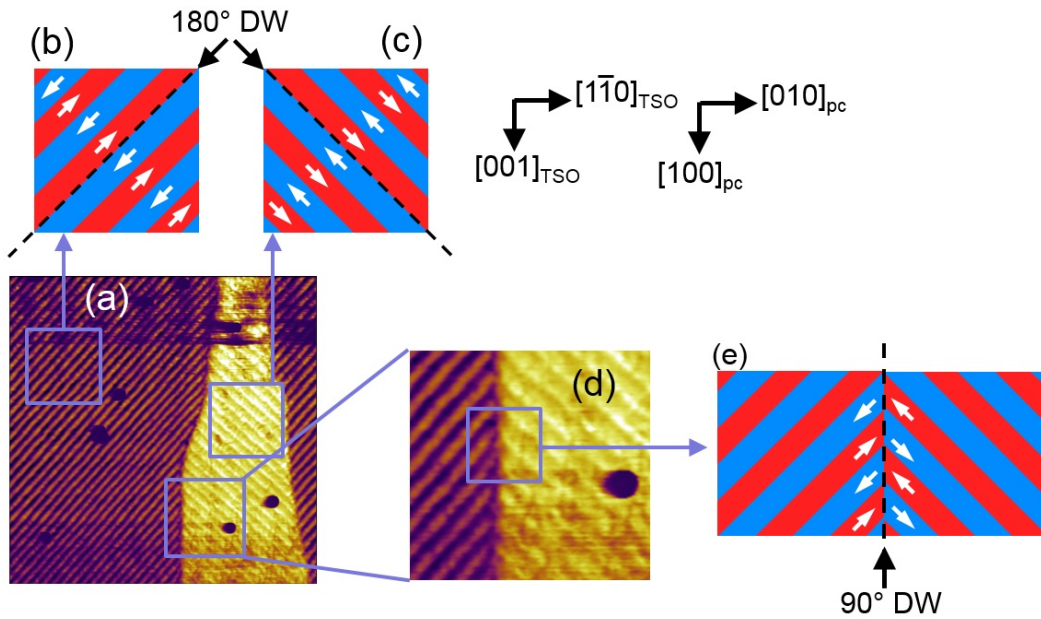


Figure 31: (a) A lateral piezoresponse image with a scan size of  $(2 \times 2) \mu\text{m}^2$  revealing both  $(001)_{\text{pc}}$  orientations further labeled as  $0^\circ$  and  $90^\circ$  variant; (b), (c) Schematic presentations of the in-plane component of the electric polarization vector (white arrows) in the domains for both variants with highlighted  $180^\circ$  domain walls within one variant. (d) Higher magnification of the lateral piezoresponse image shown in (a) on a scale of  $600 \times 600 \text{ nm}$  on the transition between the  $0^\circ$  and  $90^\circ$  variant. (e) The lateral change of the electric polarization vector at the boundary between the two variants forming a  $90^\circ$  domain wall. Adapted from [100].

linear elasticity theory. Zooming in fig. 24b as illustrated by the inset displays that the energy density difference between the two  $90^\circ$  rotated  $(001)_{\text{pc}}$  variants is rather small. Hence, both variants may be stable but obviously different energy densities lead to a preference of the  $0^\circ$  variant.

Regarding fig. 31, it seems that the domains in both variants have a different domain width. While in the  $0^\circ$  area the sheared  $M_A$  domains have equal size, the  $90^\circ$  variant

seems to be built up with broad and narrow stripes. This result is in contradiction to the x-ray data where the same domain periodicity is predicted for both types.

Why the domains of both variants can not be imaged in equal resolution with the PFM technique in fig. 31 can only be estimated. Regarding the domain wall model in fig. 31b,c, no reason can be found why there should be a different detection sensitivity for both variants as long as the cantilever is aligned as depicted in fig. 31a. However, already the lateral amplitude image in fig. 26b shows a clear evidence of strong electrostatic contribution leading to a misrepresentation of equal domains in the amplitude image [108]. As discussed in chapter 5.1, the amplitude signal measured over equal domains should not differ. But as can be seen in fig. 26b already for the  $0^\circ$  variant a bright-dark contrast appears that is not real. So far it can be assumed, that the measurement background is large and shifts the zero level of the amplitude signal in such a manner that the domains and the respective walls are measured in a false color code.

Returning to the starting point for  $\text{K}_{0.75}\text{Na}_{0.25}\text{NbO}_3$  thin films on (110)  $\text{TbScO}_3$ , the question arises why the experiment yields  $M_A$  domains and the theory predicts a  $M_C$  phase. Several explanations can be discussed:

- i The strain-phase diagram from Bai et al. [3] was calculated for pure  $\text{KNbO}_3$  and could therefore deviate for films with 25% sodium in the solid solution. Regarding the average strain - phase diagram from Diéguez et al. [22] calculated for pure  $\text{KNbO}_3$  and  $\text{NaNbO}_3$  supports the assumption. There, changes between both alkaline niobates become apparent that will lead to a shift of the transition points in fig. 26a for  $x = 0.75$ .
- ii It can not be ruled out that the composition delivered into the reaction chamber during the MOCVD process is not originally transferred into the film stoichiometry. A slightly different ratio between sodium and potassium can originate leading to changed lattice parameter of the unstrained film unit cell. Thus, the stress from the  $\text{TbScO}_3$  substrate can likewise differ. Considering the strain in dependence of the potassium content illustrated in fig. 24a shows clearly that with decreasing potassium content, the compressive strain decreases likewise. Hence, transferring a strain state with less potassium into the strain-phase diagram e.g. in fig. 24c can yield indeed a monoclinic  $M_A$  phase in contrast to the theoretically predicted  $M_C$  structure in case of a potassium content of  $x = 0.75$ .

However, in contradiction, the fact that the experimental vertical lattice parameter for the fully strained film  $d_{\perp} = 4.040 \text{ \AA}$  equals the theoretically predicted strained vertical lattice spacing of  $d_{\perp}^{\text{strained}} = 4.047 \text{ \AA}$  for  $x = 0.75$  yield the result of rather a the targeted stoichiometry.

- iii  $M_A$  domains occur oftentimes as metastable ferroelectric phase. In the literature, reasons like excessive mechanic pressure, exaggerated voltage or post-growth cooling in electric fields are claimed [[5],[107],[109]]. Likewise, the growth conditions could lead to metastable ferroelectric states. The deposition temperature was adjusted to  $T_{\text{Growth}} = 650^{\circ}\text{C}$  in the case discussed beforehand. If  $T_{\text{Growth}}$  is chosen to low, the mobility of the molecules on the substrate surface is to small to arrange in the best manner. Such, the growth does not take place at the thermodynamic equilibrium. As a proof,  $\text{K}_{0.75}\text{Na}_{0.25}\text{NbO}_3$  films on  $\text{TbScO}_3$  substrates have to be deposited at higher temperatures.

## 9. Energy density degeneration for $(100)_{\text{pc}}$ and $(001)_{\text{pc}}$ orientation:

### $\text{K}_{0.90}\text{Na}_{0.10}\text{NbO}_3$ films on $(110)$ $\text{NdScO}_3$

A second unique strain state occurrence is the film composition with  $x = 0.90$  on  $(110)$   $\text{NdScO}_3$  (NSO). Calculating the  $a_{\text{pc}}$  and  $c_{\text{pc}}$  bulk lattice parameters of  $\text{K}_{0.90}\text{Na}_{0.10}\text{NbO}_3$  according to eq. 58 yields  $a_{\text{pc}} = 3.967 \text{ \AA}$  and  $c_{\text{pc}} = 4.029 \text{ \AA}$ . In contrast to  $\text{TbScO}_3$  substrates, neodymium scandate offers a rather high anisotropic in-plane parameter on the  $(110)$  growth plane with  $a_{\text{pc}} = 2 \times 4.0015 \text{ \AA}$  and  $b_{\text{pc}} = 2 \times 4.0138 \text{ \AA}$  (see tab. 1). Evaluating the elastic strain energy density when depositing a  $\text{K}_x\text{Na}_{1-x}\text{NbO}_3$  film with  $(100)_{\text{pc}}$  or  $(001)_{\text{pc}}$  orientation on the  $(110)$   $\text{NdScO}_3$  surface reveals an energetic degeneration (fig. 32b) at  $x = 0.87$ . Since the elastic strain energy densities at this point have the same value for  $(100)_{\text{pc}}$  and  $(001)_{\text{pc}}$  oriented films, no surface orientation is preferred; this may lead to a coexistence of both phases. Calculating the strain for

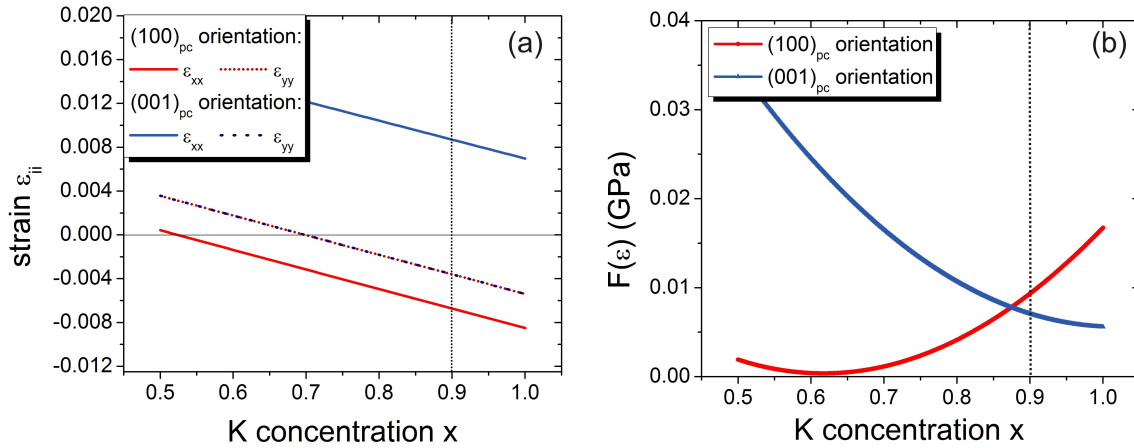


Figure 32: (a) Strain in dependence of the potassium concentration  $x$  in the solid solution  $\text{K}_x\text{Na}_{1-x}\text{NbO}_3$  for  $0.5 \leq x \leq 1$  on  $\text{NdScO}_3$  substrate. (b) Estimation of the elastic strain energy density  $F(\varepsilon)$  for  $\text{K}_x\text{Na}_{1-x}\text{NbO}_3$  on  $\text{NdScO}_3$  substrate versus potassium content  $x$  for  $0.5 \leq x \leq 1$ . For (a) and (b) the position with  $x = 0.90$  is marked.

both orientations leads to the strain-composition diagram illustrated in fig. 32a for  $x \geq 0.5$ . As a result of the large anisotropic substrate lattice parameters, the film unit cell is likewise highly anisotropically strained. For  $x = 0.90$ , the  $(100)_{\text{pc}}$  phase is compressively strained along both substrate directions counting  $\varepsilon_{xx}^{[001]_{\text{NSO}}} = -0.67\%$  and  $\varepsilon_{yy}^{[1\bar{1}0]_{\text{NSO}}} = -0.36\%$ . However, the  $(001)_{\text{pc}}$  orientation expires tensile strain of about  $\varepsilon_{xx}^{[001]_{\text{NSO}}} = +0.87\%$  and compressive strain of  $\varepsilon_{yy}^{[1\bar{1}0]_{\text{NSO}}} = -0.36\%$ . As a result, the film

composition with  $x = 0.90$  on  $(110)$   $\text{NdScO}_3$  facilitates the coexistence of a  $(100)_{\text{pc}}$  phase under average compressive strain and a  $(001)_{\text{pc}}$  orientation with mean tensile strain.

In order to study the surface morphology a  $(1 \times 1) \mu\text{m}^2$  area was measured in ambient air with the atomic force microscopy and the scan is represented in fig. 33a.

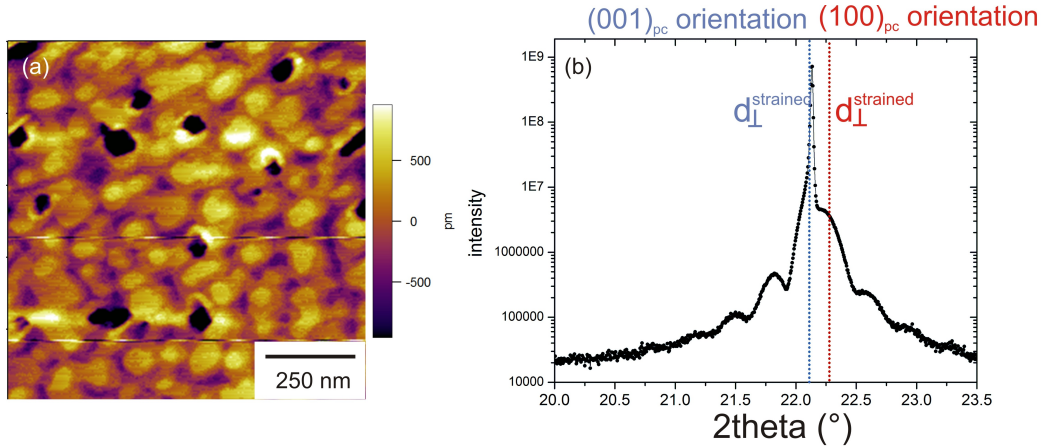


Figure 33: (a) Surface morphology of a  $\text{K}_{0.90}\text{Na}_{0.10}\text{NbO}_3$  film on a  $(110)$   $\text{NdScO}_3$  substrate on a  $(1 \times 1) \mu\text{m}^2$  scale. (b)  $\theta - 2\theta$  HRXRD pattern of a  $\text{K}_{0.90}\text{Na}_{0.10}\text{NbO}_3$  films on  $(110)$   $\text{NdScO}_3$  in the range from  $2\theta = 20^\circ - 23.5^\circ$ . The red and blue dotted lines indicate the nominal angular position of the strained vertical lattice parameter  $d_{\perp}^{\text{strained}}$  for both a  $(100)_{\text{pc}}$  and  $(001)_{\text{pc}}$  orientation, respectively, in case of  $\text{K}_{0.90}\text{Na}_{0.10}\text{NbO}_3/\text{NdScO}_3$ .

The AFM image of the film reveals very smooth surfaces with an average root mean square surface roughness of 0.5 nm. As explained in chapter 8, the determination of the growth mode for  $\text{K}_{0.90}\text{Na}_{0.10}\text{NbO}_3$  films on  $(110)$   $\text{NdScO}_3$  would require a detailed thickness series. However, from the AFM image (fig. 33a) it can be reasoned that a transition occurs from 2D growth on each single step to island growth.

For the structural investigation, a  $\theta - 2\theta$  HRXRD scan of the  $\text{K}_{0.90}\text{Na}_{0.10}\text{NbO}_3$  film around the  $(110)_{\text{NSO}}$  Bragg reflection of the orthorhombic  $\text{NdScO}_3$  substrate was performed. The measurement is shown in the range from  $2\theta = 20^\circ - 23.5^\circ$  in fig. 33b. The diffraction pattern is characterized by a sharp substrate peak around  $2\theta = 22.13^\circ$  and a single film peak shaped as a shoulder appearing at about  $2\theta = 22.22^\circ$ . Measuring the diffraction pattern until  $2\theta = 70^\circ$  reveals no secondary phases proving a pure perovskite structure of the film. Extracting the angular values needed for eq. 56 and 57 from fig. 33b yield a vertical lattice parameter of  $d_{\perp} = 4.013 \text{ \AA}$  and film thickness  $t = 29 \text{ nm}$

for the  $\text{K}_{0.90}\text{Na}_{0.10}\text{NbO}_3$  film. For comparison, the theoretical strained vertical lattice spacing for both, a  $(100)_{\text{pc}}$  and  $(001)_{\text{pc}}$  orientation, were estimated in accordance to eq. 67 to  $d_{\perp}^{(100)_{\text{pc}}\text{strained}} = 3.987 \text{ \AA}$  and  $d_{\perp}^{(001)_{\text{pc}}\text{strained}} = 4.018 \text{ \AA}$ . These values are transferred into the  $\theta - 2\theta$ -scan in fig. 33b as red and blue dotted lines, respectively.

As expected from the linear elastic theory, the experimental parameter is between both theoretical ones. In consequence, indeed, both orientation could have been occurred.

Transferring the strain values obtained for  $x = 0.90$  from fig. 32a into the multi-dimensional misfit strain - misfit strain phase and energy density diagram in fig. 34a yields the prediction of a monoclinic  $M_c$  phase for both orientations. Indeed, a  $M_c$

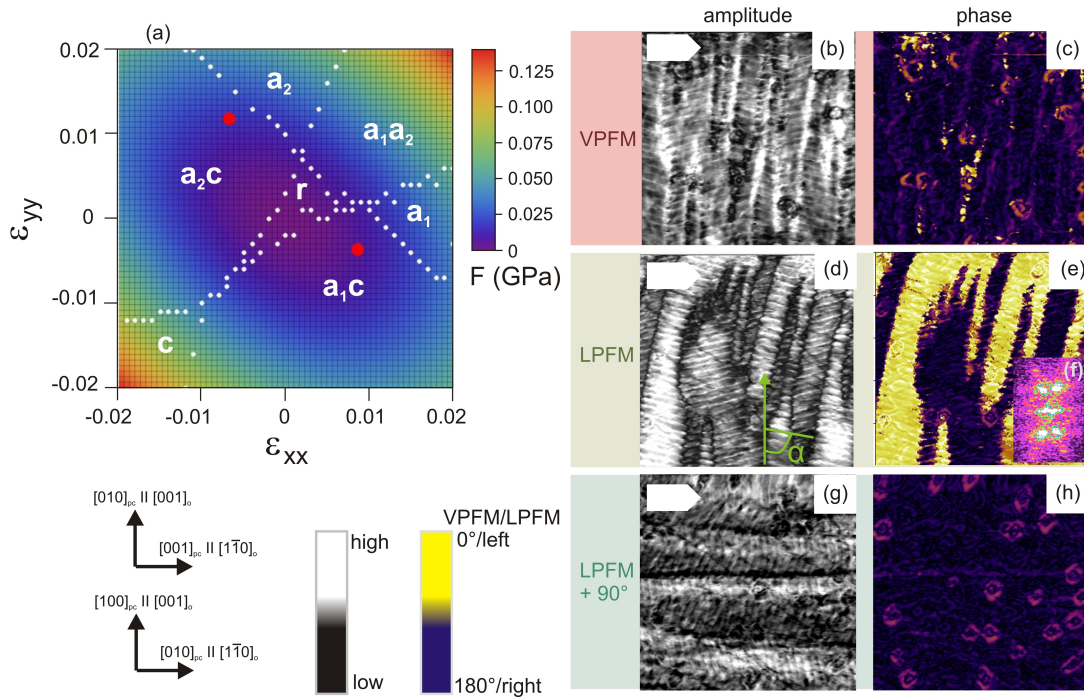


Figure 34: (a) 3D plot of the elastic strain energy density  $F(\varepsilon)$  for  $\text{K}_x\text{Na}_{1-x}\text{NbO}_3$  in dependence of the biaxial strain  $\varepsilon_{xx}$  and  $\varepsilon_{yy}$ . On the energy landscape the strain-phase diagram for  $\text{KNbO}_3$  from fig. 22a was plotted. The filled red circles indicate the  $(001)_{\text{pc}}$  strain state in  $\text{K}_{0.90}\text{Na}_{0.10}\text{NbO}_3/\text{NdScO}_3$ . PFM measurements of a  $\text{K}_{0.90}\text{Na}_{0.10}\text{NbO}_3/\text{NdScO}_3$  film, picture size  $(1 \times 1) \mu\text{m}^2$ : (b), (c) vertical, (d)-(h) lateral amplitude and phase image, respectively. The cantilever orientation is illustrated in the upper left of part of the image. (f) 2D-FFT of the lateral amplitude image (d).

domain structure is characterized by a polarization vector that can freely rotate within the  $\{100\}_{\text{pc}}$  monoclinic mirror planes and exhibits a  $Pm$  symmetry. Problematically, the misfit strain - misfit strain phase diagram was calculated exclusively for a  $(001)_{\text{pc}}$  orientation because the relevant coefficients for eq. 69 are only available for  $\text{KNbO}_3$

in the *c*-orientation. In conclusion, the prediction of  $M_c$  domains for the  $(100)_{pc}$  phase may not be correct.

However, to get an idea about the expectable domain type in the *a*-orientation, the unit cell distortion should be inspected. Both regarded orientations differ by at least one  $90^\circ$  rotation of the film unit cell. As a result, the monoclinic angle is in-plane for the  $(100)_{pc}$  oriented cells. This distortion would fit to the monoclinic  $a_1a_2$  formation. Meanwhile, the latter exhibits  $Pm$  symmetry in agreement to the  $M_c$  domains for  $(001)_{pc}$  orientation. Indeed, for a  $(100)_{pc}$  oriented film a  $a_1a_2$  domain structure was confirmed experimentally [[96],[106]]. Therefore, it can be assumed that rather a monoclinic  $a_1a_2$  pattern is going to develop for the  $(100)_{pc}$  phase.

The vertical and lateral PFM images are displayed in fig. 34b-h distinguished into amplitude and phase signal on a scale of  $(1 \times 1) \mu\text{m}^2$ . Already on a first sight, these electric images show apparently a domain pattern which is rather complex and differs significantly from those of  $\text{K}_{0.75}\text{Na}_{0.25}\text{NbO}_3/\text{TbScO}_3$ .

In the lateral phase image in fig. 34e comparatively large domain bundles colored in yellow and violet can be resolved. They are tentatively aligned along the  $[001]_{\text{NSO}}$  direction with typical lateral sizes in  $[1\bar{1}0]_{\text{NSO}}$  direction between 50 and 200 nm. The color code implies a distinct left - and rightwards torsion of the cantilever caused by a changing direction of the lateral piezo active component from left to right. Already in the lateral phase image 34e it can be assumed, that the domain pattern is not continuously one domain type along the  $[001]_{\text{NSO}}$  direction, but interrupted by tiny stripes running rather along the  $[1\bar{1}0]_{\text{NSO}}$  direction. Indeed, a particular substructure arises in the corresponding vertical and lateral amplitude figs. 34b and d. The large domain bundles consist of a highly periodic array with alternating narrow and broad domains that are shaped like honeycombs. The periodicity in  $[001]_{\text{NSO}}$  direction amounts to about  $L_{\text{PFM}} = (30 \pm 1) \text{ nm}$ .

Of major interest is if these narrow stripes are domains or represent only domain walls. Analyzing both amplitude images 34b and d in detail on the basis of the color code enables a distinct classification. The lateral amplitude image 34d reveals that the bundles along  $[001]_{\text{NSO}}$  are separated by pure domain walls because the amplitude decreases to zero. In contrast, the narrow domains within the bundles including an angle to the  $[1\bar{1}0]_{\text{NSO}}$  direction are dyed in white for both the vertical and lateral amplitude manifesting a high response. Therefore, it can be concluded that they are domains otherwise the amplitude has to drop to roughly zero as in the case discussed beforehand. It

seems, that the domain walls there are too small to be solved within the resolution of a piezoresponse force microscope. That circumstance is not unusual because the width of a ferroelectric domain wall can be about a few unit cells only  $[[110],[111],[112]]$ . Indeed, the same situation arose in the  $K_{0.75}Na_{0.25}NbO_3$  films on  $TbScO_3$  hence it seems to be common in these films.

In addition to the white colored narrow domains in the vertical and lateral amplitude images 34b and d, the broad stripe domains are dyed differently in both modes. They have a low response in the vertical and a high signal in the lateral image. Herefrom it can be concluded that two different domain types occur which are alternatingly arranged. On one hand, the narrow domains with high response in the vertical and lateral mode manifesting a phase with a distinct in- and out-of-plane signal. On the other hand, comparably broad stripes that exhibit mainly in-plane polarization.

It should also be noted that the interpretation with only one domain variant and domain walls would be incomprehensible from the theoretical background of domain wall formation energies and - algorithms. Then, the walls would separate domains of the same type with the same in-plane polarization alignment as can be concluded from the lateral phase figure 34e. Such a structure would be accompanied by remarkably energetic costs caused by the formation of a huge density of domains walls.

Unusually, these embedded stripes are tilted off against the  $[001]_{NSO}$  direction by  $\alpha = \pm 75^\circ$  as it is schematically illustrated in green in fig. 34d. This circumstance can be likewise evaluated from the two branches in the 2D-FFT image in fig. 34f. Such a tilting is completely unknown from classical ferroelectric systems in tetragonal, orthorhombic or rhombohedral materials where the domain walls are fixed to the high symmetric directions and therefore only tilting angles of  $\alpha = 45^\circ$  and  $90^\circ$  can occur.

In order to clarify the orientation(s) of the film, grazing incidence in-plane x-ray diffraction (GIXD) has been performed at the European Synchrotron Radiation Facility (ESRF) using an x-ray wavelength of  $\lambda = 1.239 \text{ \AA}$ . In-plane x-ray reciprocal space maps have been measured in the vicinity of the  $(008)_{NSO}$  and  $(2\bar{2}4)_{NSO}$  in-plane Bragg reflections and are shown in fig. 35a,b. In contrast to the film on  $TbScO_3$ , a characteristic peak splitting  $P_1$  and  $P_2$  can be observed for both measured reciprocal lattice points. As discussed in chapter 8, the lattice splits as a result of monoclinic symmetry as illustrated schematically in fig. 27e.

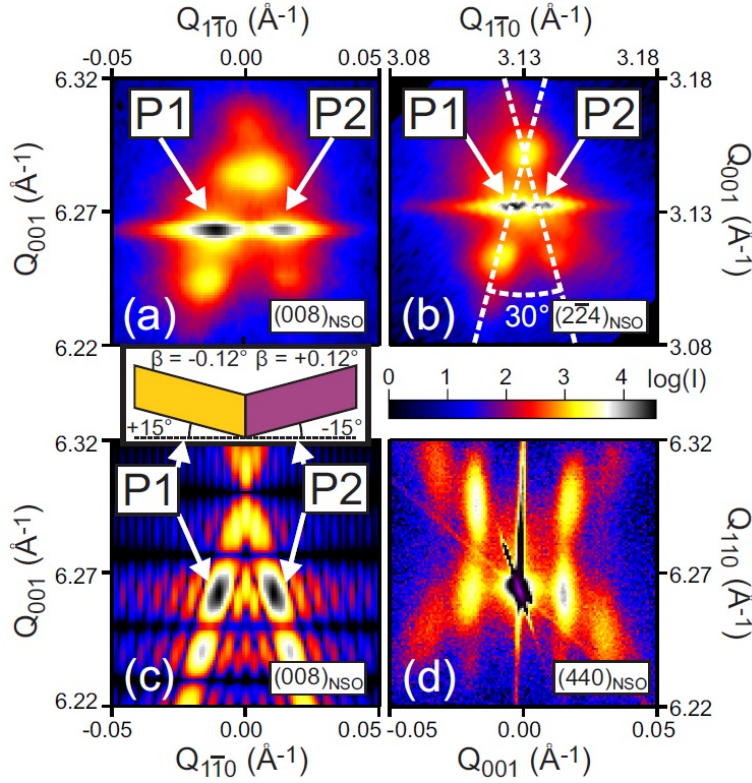


Figure 35: GIXD in-plane x-ray reciprocal space maps in the vicinity of the (a)  $(008)_{\text{NSO}}$  and (b)  $(2\bar{2}4)_{\text{NSO}}$  substrate Bragg reflections. (c) Simulation of reciprocal space map around  $(008)_{\text{NSO}}$ , for details see text. (d) Out-of-plane reciprocal space map in the vicinity of  $(440)_{\text{NSO}}$  substrate Bragg reflection. Taken from [113].

A detailed analysis of the observation of peak splitting near the  $(008)_{\text{NSO}}$  and  $(2\bar{2}4)_{\text{NSO}}$  Bragg reflection points together with the absence of a film peak splitting in the vicinity of the  $(4\bar{4}0)_{\text{NSO}}$  reflex (not shown here) reveals that  $P_1$  and  $P_2$  are caused by domains with alternate in-plane shearing. The monoclinic cell exhibits a distortion angle of  $\beta = \pm 0.12^\circ$  and a shearing along the  $[001]_{\text{NSO}}$  direction whereas the film crystal lattice remains coherent along the  $[\bar{1}\bar{1}0]_{\text{NSO}}$  direction. In conclusion, the observed in-plane shearing of the film lattice is attributed to the presence of a monoclinic phase with  $(100)_{\text{pc}}$  orientation and thus  $a_1a_2$  domains. This is in agreement with the strong lateral piezoelectric response of the bundles in the PFM measurements.

As an evidence of the periodic ordering of the domains well pronounced satellite reflections emerge in the vicinity of  $P_1$  and  $P_2$  for both the  $(008)_{\text{NSO}}$  and  $(2\bar{2}4)_{\text{NSO}}$  in-plane reciprocal lattice points. From the satellite peak spacing a periodicity of  $L_{\text{GIXD}} = (30 \pm 1)$  nm along the  $[001]_{\text{NSO}}$  direction can be deduced. This result is in accordance with the PFM data  $L_{\text{PFM}} = (30 \pm 1)$  nm shown in fig. 34b-h.

Interestingly, for each peak only one satellite branch emerges. For  $P_1$  it is tilted off by  $\alpha = +75^\circ$  while for  $P_2$  it is tilted off by  $\alpha = -75^\circ$  against the  $[001]_{\text{NSO}}$  direction. As a result, the sign of the monoclinic shearing can be directly related to the observation in the piezoresponse force micrographs. The "yellow" domains in fig. 34e exhibit an in-plane lattice shearing of  $\beta = -0.12^\circ$  whereas the "violet" domains can be associated with an in-plane lattice shearing of  $\beta = +0.12^\circ$ .

In order to prove the model, the domain arrangement as depicted schematically in fig. 35 was simulated by means of the Hosemann function [114] for the  $(008)_{\text{NSO}}$  Bragg reflection by Dr. Martin Schmidbauer and Dr. Michael Hanke. The result can be seen in fig. 35c and is in good agreement to the respective experimental result in fig. 35a.

To unveil the structure of the narrow subdomains, plan-view transmission electron microscopy (TEM) investigations using a FEI Titan 80-300 operating at 300 kV were carried out by Dr. Toni Markurt (for further information see [113]). Hereby, the sample has to be "destroyed" for preparation and therefore a similar sample with the same deposition parameters were used as for the sample discussed before. In order to avoid elastic relaxation of the strained  $\text{K}_{0.90}\text{Na}_{0.10}\text{NbO}_3$  film as a result of thinning down the substrate during specimen preparation, TEM specimens with a comparatively thick ( $t > 100$  nm) substrate layer were used. A dark field contrast pattern obtained by using the excitation vector  $\mathbf{g} = (002)_{\text{NSO}}$  is illustrated in fig. 36. In excellent agreement with the PFM measurement shown in fig. 34c and e the same characteristic features appear. A substructure of narrow stripe domains arise within the matrix of large domain bundles as can be seen in the dark field image 36a, in the in-plane shear component  $\varepsilon_{xy}$  map as well as in the in-plane strain  $\varepsilon_{xx}$  image in fig. 36c,d, respectively. This confirms that the TEM specimen preparation has not changed significantly the local strain state of the film and thus the domain structure is still comparable to the as-grown sample state. The analysis in fig. 36c shows that the large domain bundles colored in yellow and violet in the PFM (fig. 34e) - and red and green in the TEM results - differ in their in-plane shear angle  $\varepsilon_{xy}$ . This result is in agreement with GIXD observations discussed beforehand: There, the  $(100)_{\text{pc}}$  orientation of the pseudocubic unit cell was determined with an alternate shearing along  $\pm[001]_{\text{NSO}}$ . From the STEM images, the corresponding monoclinic shear angle difference between adjacent domain bundles can be evaluated to  $\Delta\varepsilon_{xy} = 2\beta = (0.4 \pm 0.1)^\circ$ . In comparison to the value obtained by GIXD  $2\beta = (0.2 \pm 0.1)^\circ$ , these data are slightly larger but is still in satisfactory agreement. The deviation could result from the fact that for both measurements

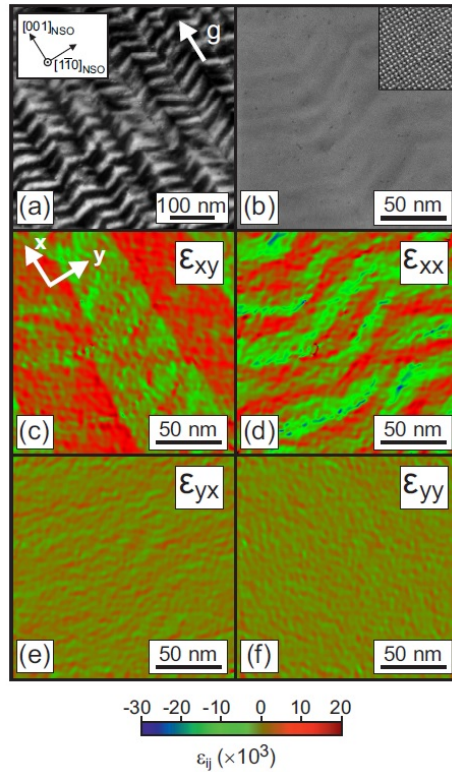


Figure 36: Plan-view (S)TEM micrographs of a  $\text{K}_{0.90}\text{Na}_{0.10}\text{NbO}_3$  film on  $(110)$   $\text{NdScO}_3$  substrate: (a) Dark field TEM image and (b) high-resolution STEM ADF measurement. The inset in (b) shows a magnification whereby white intensity maxima correspond to the Nb atomic columns of the film. The in-plane shear strain maps divided in  $\varepsilon_{xx}$  (d) and  $\varepsilon_{xy}$  (c). In addition the in-plane axial strain maps  $\varepsilon_{yx}$  (e)  $\varepsilon_{yy}$  (f) obtained from a geometric phase analysis of (b). Taken from [113].

different samples were used that slightly differ.

A major information that can be gained from these STEM measurements is that the broad and narrow subdomains exhibit each a different in-plane lattice parameter along the  $[001]_{\text{NSO}}$  direction. The evaluation shows that the narrow areas exhibit a reduced lattice parameter of  $\Delta\varepsilon_{xx}^{\text{TEM}} = (-1.0 \pm 0.3)\%$  in comparison to the broader ones. In contrast, complementary maps along the orthogonal  $[1\bar{1}0]_{\text{NSO}}$  direction reveal no significant contrast within the accuracy as depicted in fig. 36e,f. This behavior would be likewise in agreement to the prediction of an additional  $(001)_{\text{pc}}$  orientation because the  $\varepsilon(x)$  characteristic in fig. 32a shows no strain difference for both orientations along the  $[1\bar{1}0]_{\text{NSO}}$  direction. These results strongly suggest a  $(001)_{\text{pc}}$  orientation of the pseudocubic unit cell in the narrow subdomains.

To identify a  $(001)_{\text{pc}}$  orientation, x-ray diffraction in normal geometry was performed. The  $c$ -orientation should have a different vertical lattice parameter compared to the  $(100)_{\text{pc}}$  symmetry as it was discussed in the beginning of this chapter ( $d_{\perp}^{(100)_{\text{pc}}\text{strained}} = 3.987 \text{ \AA}$  and  $d_{\perp}^{(001)_{\text{pc}}\text{strained}} = 4.018 \text{ \AA}$ ). Moreover, the  $(001)_{\text{pc}}$  orientation is characterized by an out-of-plane monoclinic distortion in contrast to the  $(100)_{\text{pc}}$  phase. As a result, four Bragg reflection points should occur: one each for the substrate and the  $(100)_{\text{pc}}$  phase and two for the monoclinically distorted unit cells with  $(001)_{\text{pc}}$  orientation. A reciprocal space map around the symmetrical  $(440)_{\text{NSO}}$  out-of-plane substrate Bragg reflection was measured and illustrated in fig. 35d. However, since the Bragg reflection peaks of the  $(001)_{\text{pc}}$  phase are interfered by the substrate peak and the Bragg peak of the  $(100)_{\text{pc}}$  phase, the monoclinic distortion of the  $(001)_{\text{pc}}$  orientation can not be resolved.

But, a complex pattern with satellite peaks arises. The latter can only be explained, if a period arrangement of two orientations with different out-of-plane parameter exists. Moreover, the spacing between these two orientations can be evaluated from the separation of the satellite peaks along  $Q_{001}$  to a periodicity of 30 nm. Together with the information from GIXD, where a distinct  $(100)_{\text{pc}}$  orientation was detected and the alternating domain pattern determined in PFM as well as in STEM mode, the only possibility is a  $(001)_{\text{pc}}$  phase in the narrow subdomains.

Summarizing the electrical and structural data into a domain model yields fig. 37. The analysis shows that the large bundles in fig. 34e, marked likewise by yellow and violet colors in fig. 37, exhibit  $(100)_{\text{pc}}$  orientation. As displayed in fig. 37 at the bottom, for this type the film unit cell features an in-plane monoclinic distortion accompanied with an in-plane electric polarization. Between the bundles, the in-plane polarization changes by  $90^\circ$  as can be extracted from the color code in the lateral phase image 34f. Such a ferroelectric pattern is assigned as  $a_1a_2$  domain. In the adjacent narrow domain, schematically sketched in light blue and green, the film lattice is rotated by  $90^\circ$  into a  $(001)_{\text{pc}}$  orientation. Simultaneously, the polarization rotates and exhibits then a pronounced vertical component. Due to the fact, that the vector is aligned within the  $\{100\}_{\text{pc}}$  planes, the corresponding domain pattern is indeed a so-called  $M_c$  pattern. This result is moreover in agreement with the calculated misfit strain-misfit strain phase diagram shown in fig. 34a. From the crystallographic view, both orientations have  $Pm$  symmetry and can be transformed into each other easily by a rotation. This point may facilitate the growth of both types by means of elastic deformation and

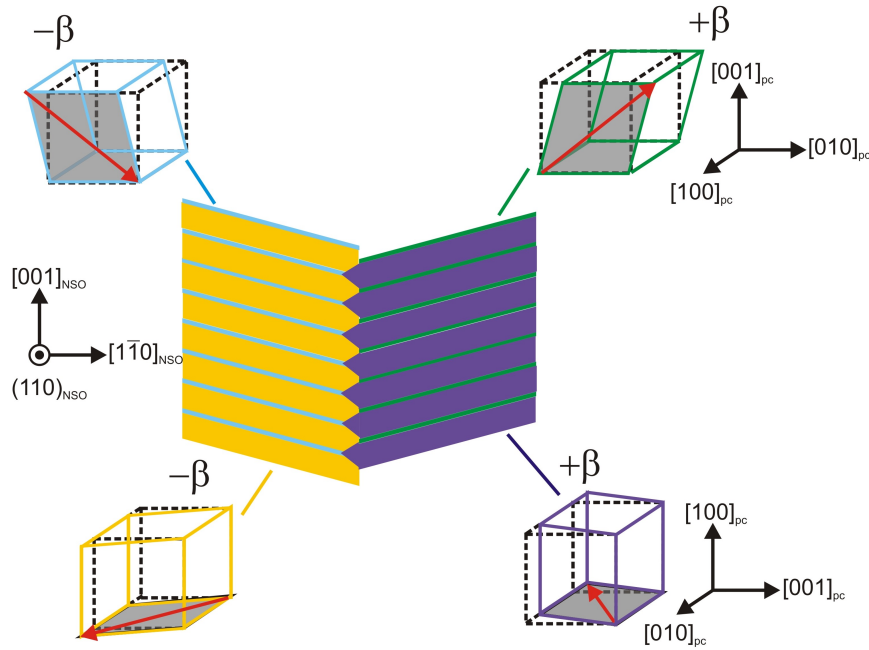


Figure 37: Schematic plan view of the domain pattern arising in the corresponding  $\text{K}_{0.90}\text{Na}_{0.10}\text{NbO}_3$  depicted in cross sectional view. Moreover, sheared pseudocubic unit cells for both  $(100)_{\text{pc}}$  and  $(001)_{\text{pc}}$  orientations. The  $a_1a_2$  domains with  $(100)_{\text{pc}}$  orientation are dyed in yellow and violet colors whereas the  $M_c$  domains with  $(001)_{\text{pc}}$  orientation are colored in blue and green. The red arrows indicate the orientation of the electrical polarization vector.

thus without defects.

In contrast to ferroelectric materials with tetragonal or rhombohedral symmetry, in  $\text{K}_{0.90}\text{Na}_{0.10}\text{NbO}_3$  films on  $\text{NdScO}_3$  distinctive differences can be observed:

- i** monoclinic symmetry resulting in  $a_1a_2/M_c$  domains instead of a  $a/c$  domain pattern
- ii** due to the monoclinic symmetry domain walls do not necessarily run along main crystallographic axes, e.g. parallel to  $[001]_{\text{NSO}}$ ,  $[\bar{1}\bar{1}0]_{\text{NSO}}$  or  $[112]_{\text{NSO}}$ . As a consequence, the film in fig. 34 exhibits an inclination angle of  $\alpha = 75^\circ$  in respect to the  $[001]_{\text{NSO}}$  direction. This phenomenon will be discussed in detail in chapter 10.

One important factor is the switching behavior of a ferroelectric film under an external bias. Experimentally, a direct voltage is applied to the tip and a pattern is written on the film surface. For vertical  $c$ -domains, the result is the well-known switching of the polarization vector by  $180^\circ$   $[[115],[116]]$ .

If and how a mainly lateral domain pattern reacts on a vertically applied voltage is rather less studied [[117],[118],[119]]. Therefore, the discussed domain pattern formed in  $\text{K}_{0.90}\text{Na}_{0.10}\text{NbO}_3$  on (110)  $\text{NdScO}_3$  is ideally suited for a fundamental investigation of lateral poling.

The lateral PFM measurements before and after a writing pulse of  $V_{\text{dc}} = +2$  V are shown in fig. 38. Within the red square in fig. 38a the voltage was applied exclusively. For a better correlation of the PFM signal to the lithography area, the red square was illustrated in all LPFM images in fig. 38.

The poling field was situated this way on the ferroelectric herringbone pattern that it has overlap with "ending" bundles aligned along  $[001]_{\text{NSO}}$ . The result can be seen

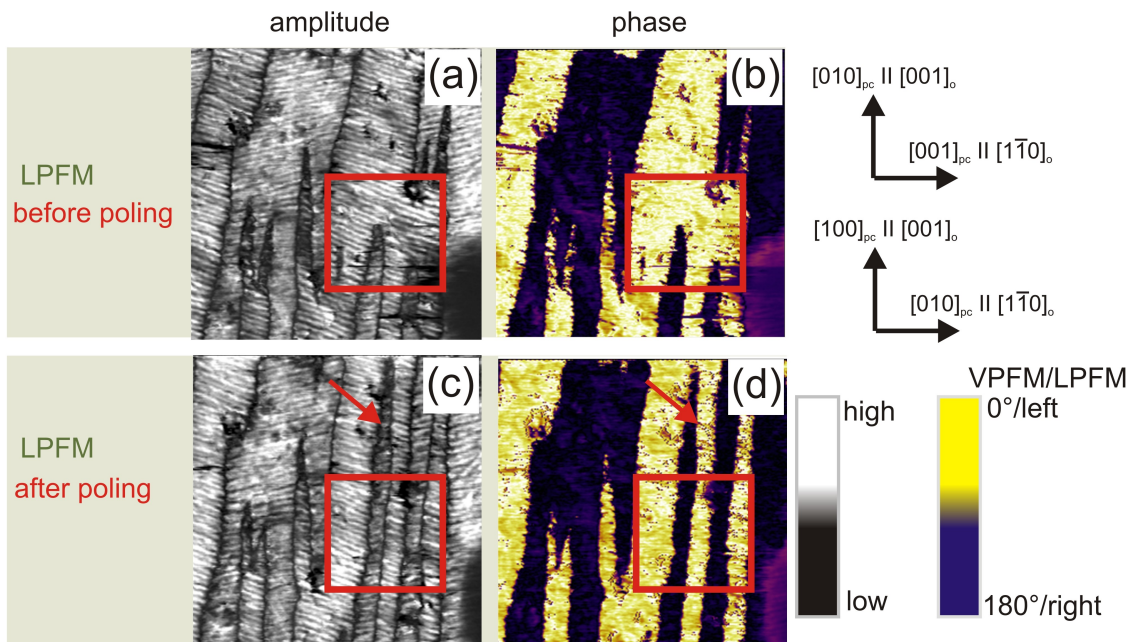


Figure 38: Lateral PFM images of a  $\text{K}_{0.90}\text{Na}_{0.10}\text{NbO}_3$  film deposited on a (110)  $\text{NdScO}_3$  substrate presented (a)-(b) before poling and (c)-(d) after poling each distinguish into amplitude and phase signal. The red square marks the lithography area. The bias applied amounts  $V_{\text{dc}} = 2$  V.

in fig. 38c,d. The former "ending" bundles grow in  $[001]_{\text{NSO}}$  direction far behind the red poling square (see red arrows). Interestingly, the positive voltage does not lead to a single polarization alignment, a so-called monodomain, within the red square. As can be seen in the lateral phase image in fig. 38d, the in-plane polarization within the written square leads to a torsion of the cantilever both left - and rightwards. Eventually, the highly periodic and nested herringbone structure leads immediately to a compensation of the polarization after switching to remain stable.

How can it be explained that a vertically applied bias lead to a lateral poling? It has to be noted that in contrast to the poling model in chapter 1.4, the  $\text{K}_{0.90}\text{Na}_{0.10}\text{NbO}_3$  film was grown epitaxially and fully strained on the bare substrate. Hence, the deposition of a bottom electrode in-between film and substrate was rejected. Consequently, the introduced field may be distributed completely different in comparison to the domain switching model in chapter 1.4. This effect is schematically drawn in fig. 39. While the

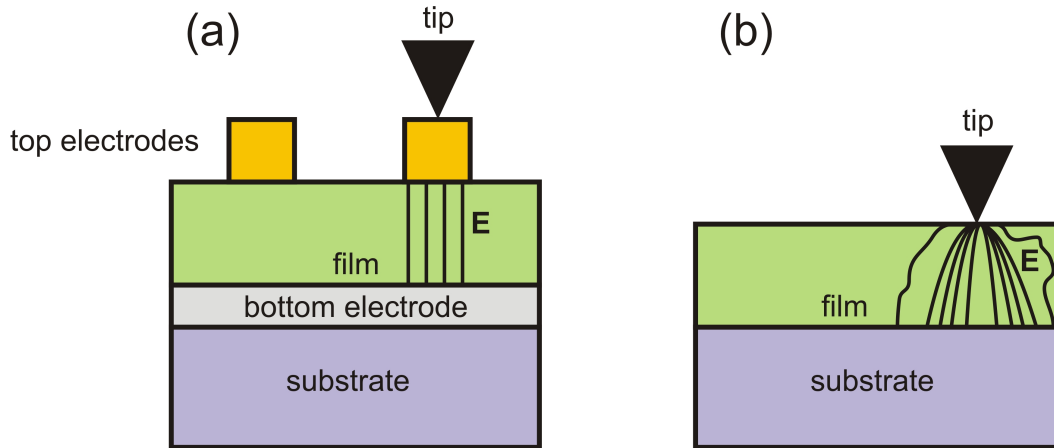


Figure 39: Electric field (a) between a top and bottom electrode and (b) without any electrode.

electric field is homogeneously distributed between two electrodes (fig. 39a), it could propagate not directly to the substrate in the case without any electrode (fig. 39b). In the latter, defects and film distortions can influence the energetically favored path. In consequence, the lateral expansion of the electric field in the film can be much higher. From fig. 38c,d the conclusion can be drawn that the electric field propagates well in lateral dimension yielding a switching far behind the poling area. Hence, the missing bottom electrode could be beneficial for the lateral switching.

Generally, lateral domains reduce mainly the strain. How it works to pole an  $a_1a_2$  domains from "yellow" to "violet" is not completely understood so far. Regarding fig. 37, the  $(100)_{pc}$  unit cell has to rotate by  $90^\circ$  although it should be pinned to the substrate. Perhaps, this rotation is not needed because the monoclinic unit cell distortion is rather small with  $\beta = 0.12^\circ$ . Hence, the distortion difference between "yellow" to "violet" is about  $\beta = \pm 0.12^\circ$  only and can be switched by means of an elastic progress.

Meanwhile the bundle width in  $[\bar{1}\bar{1}0]_{NSO}$  remains constant as well as the periodicity of the stripe domains within the bundles. This effect is maybe due to the nested multi-domain structure itself. Considering the theoretical calculations for these so-called "multi-rank" or "herringbone" structures  $[[120],[121],[122],[123]]$ , domain walls behave

differently. To explain this characteristic, the following notation should be used. As can be seen in fig. 40, the domain walls separating the bundles shall be denoted as  $d_2$  whereas the small herringbones should be confined by  $d_1$  walls. The theoretical calculations on domain switching in such a confinement as the herringbone arrangement come to the conclusion that  $d_1$  and  $d_2$  have different freedom to move  $[[120],[121]]$ . The reason is due to the pursuit of energetic neutralization. In consequence, the shape and domain volume have to be kept constant during domain growth/switching. This aim can be easily fulfilled when the  $d_1$  domain walls move, but is difficult for a movement of  $d_2$  domain walls as it should be illustrated schematically in fig. 40. Indeed, the same

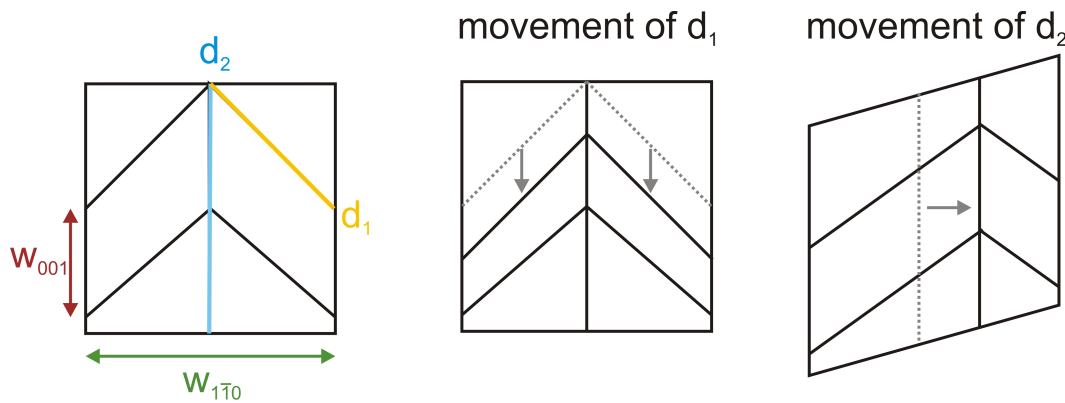


Figure 40: Schematic illustration of the movability of different domain walls in ferroelectric herringbone pattern according to  $[[120],[121]]$ .

behavior can be observed during poling of the  $K_{0.90}Na_{0.10}NbO_3$  film grown on a (110)  $NdScO_3$  substrate. Hence, the development exclusively along  $[001]_{NSO}$  seems to be in order of energetic neutralization.

Finally, the lithography area was scanned for hours to see if a back switching occurs. But the domain pattern remains stable. Hence, a vertically applied bias can yield to an irreversible lateral switching.

It shall be mentioned, that no experimental difference can be observed if the applied voltage has a positive or negative sign.

To sum up, the commonly known switching from vertical domains into one polarization state does not appear. This circumstance may be explained by the missing bottom electrode and the nested herringbone pattern.

Because of the problem how the lateral switching could progress, it was considered to be impossible. But, the example  $K_{0.90}Na_{0.10}NbO_3$  on  $NdScO_3$  prove impressively the possibility to switch also in lateral direction.

Such an alternating monoclinic domain pattern of  $a_1a_2/M_c$  domains is potentially of huge technological relevance. As already described in chapter 2.5 and 8, monoclinic phases are accompanied by giant piezoelectric responses attributed to the free rotation of the polarization vector. A similar rotation can be artificially mimicked by a domain structure with alternating exclusive in-plane and out-of-plane polarization. At the domain walls discontinuities exist that provoke a polarization rotation enhancing the piezoresponse in the same manner. Such a behavior was observed in tetragonal  $a/c$  domain pattern [[124],[125]]. Meanwhile, a piezo-enhanced signal was also detected in vortex structures [126].

However, an even larger longitudinal piezoelectric coefficient is expected for the combination of both - a monoclinic alternating domain structure with polarization discontinuities at the domain walls due to the exclusive in-plane and inclined polarization components in adjacent domains as it was theoretically predicted by Koukhar et al. [97]. Indeed, the presented pattern is the first experimental realization of such a structure.

Therefore, after proving the concept of coexisting monoclinic phases predicted by linear elasticity theory and experimentally verified by XRD, TEM and PFM, a similar film with a thickness of  $t = 25$  nm was deposited on a conducting  $\text{SrRuO}_3$  bottom electrode deposited with pulsed laser deposition for comparison. The resulting vertical and lateral PFM images are depicted in fig. 41a-d. The same herringbone pattern as described before for the deposition of  $\text{K}_{0.90}\text{Na}_{0.10}\text{NbO}_3$  on the bare  $\text{NdScO}_3$  substrate arises on the multi-layer structure  $\text{K}_{0.90}\text{Na}_{0.10}\text{NbO}_3/\text{SrRuO}_3/\text{NdScO}_3$  (fig. 41a-d). It becomes obviously that the ordering is worse on the sample coated with  $\text{SrRuO}_3$  compared to the 29 nm sample thick sample discussed in fig. 34b-h. This behavior could be explained by several effects. Defects could be introduced from the intersection  $\text{SrRuO}_3$  layer into the  $\text{K}_{0.90}\text{Na}_{0.10}\text{NbO}_3$  film partially hindering the perfect ferroelectric ordering. Indeed, the bottom electrode was grown via pulsed laser deposition (PLD) yielding oftentimes off-stoichiometric films with reduced crystal quality. Moreover, the films have to be transported from the PLD chamber to the MOCVD reactor yielding the possibility of further environmental dust on the surface. Additionally, the electrical boundary conditions are different with a conducting electrode underneath the film which may influence the domain formation. Indeed, a plastic lattice relaxation of the  $\text{SrRuO}_3$  film reducing the final stress on the  $\text{K}_{0.90}\text{Na}_{0.10}\text{NbO}_3$  film can be neglected as

the SrRuO<sub>3</sub> is only 10 nm thick and reciprocal space maps performed in the University of Groningen showed no onset of relaxation processes.

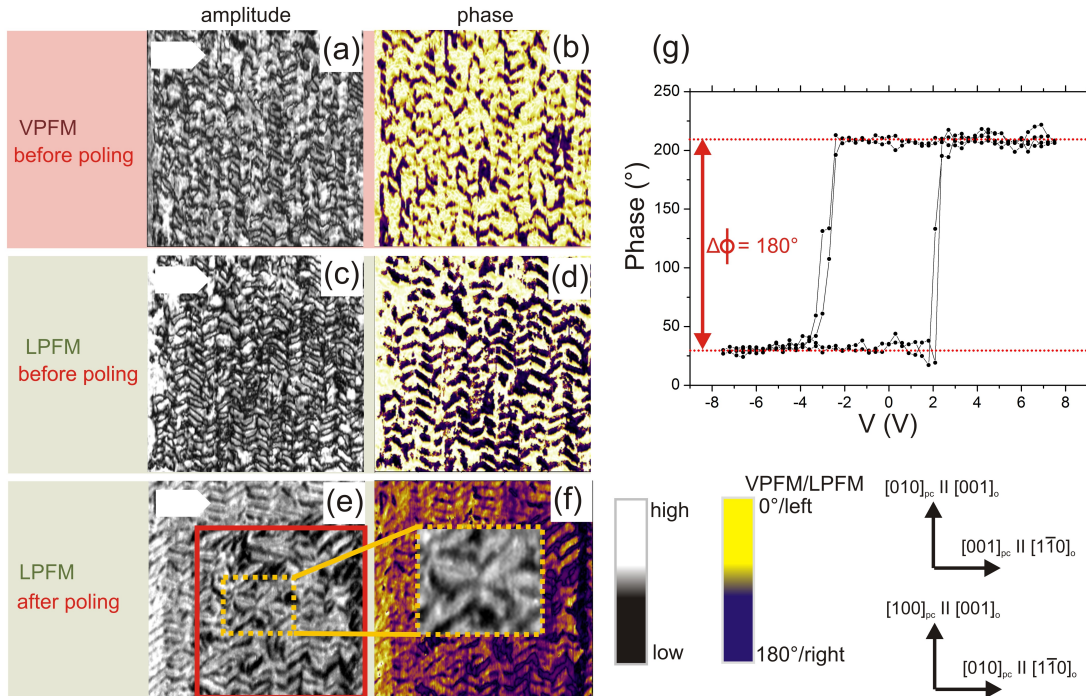


Figure 41: PFM measurements of a  $\text{K}_{0.90}\text{Na}_{0.10}\text{NbO}_3$  film on a SrRuO<sub>3</sub> bottom electrode on a NdScO<sub>3</sub> substrate, picture size  $(1 \times 1) \mu\text{m}^2$ : (a), (b) vertical, (c)-(f) lateral amplitude and phase image, respectively. The measurements (a)-(d) are taken before writing the red square with  $V_{\text{dc}} = 2 \text{ V}$  on the sample surface. The lateral PFM images (e) and (f) are measured afterward. The orange, dotted square shows a magnification of the lateral amplitude image. (g) Phase-Voltage diagram extracted from a local hysteresis measurement. The phase shift of  $\Delta\phi = 180^\circ$  is illustrated in red.

In order to reveal the influence of the bottom electrode on the lateral switching process, the  $\text{K}_{0.90}\text{Na}_{0.10}\text{NbO}_3/\text{SrRuO}_3/\text{NdScO}_3$  stack was written with a square of  $V_{\text{dc}} = 2 \text{ V}$ . The resulting lateral PFM measurement is depicted in fig. 41e,f indicating the lithography area with a red square.

Obviously, the influence of a bias is different with a conducting bottom electrode underneath. First, the bias induced changes are limited to the poling area. Second, the bundles do not grow neither in  $[001]_{\text{NSO}}$  nor in  $[\bar{1}\bar{1}0]_{\text{NSO}}$  direction. But, the small stripe domains within the bundles are affected. They are partially rotated as it is highlighted in an orange dotted square for a specific position yielding a cross of stripe domains as it can be seen in the magnified orange dotted square. A similar rotation was observed before by Xu et al. [127] but as an intermediate step for a complete reversal. Therefore,

it can be assumed that the lateral PFM measurement in fig. 41e,f shows a metastable switching state. Why it was "frozen" in this state can only be supposed. Probably, it was pinned by defects, maybe arising from the SrRuO<sub>3</sub> electrode. This disadvantage from first sight, can provoke conducting domain walls. This could not be proven on this sample so far but is part of further research.

The bottom electrode enables further measurements. First, a ferroelectric hysteresis could be measured as it is shown in fig. 41g for the phase part. The hysteresis reveals a phase difference of  $\Delta\phi = 180^\circ$  which reflects at least two stable phases of the polarization that can be achieved via an external bias proving the ferroelectric nature of the film on a different scale.

Moreover the longitudinal piezoelectric coefficient  $d'_{33}$  can be recorded. According to the theoretical calculations of Koukhar et al. [97], the highest  $d'_{33}$  values can be achieved indeed in such an alternating, monoclinic  $a_1a_2/M_c$  structure. Due to a lack of top electrodes, the vertical piezoelectric coefficient was determined locally with the PFM according to the procedure explained in chapter 5.4 yielding a value for the piezoelectric response in z-direction of  $d'_{33} = 29 \frac{\text{pm}}{\text{V}}$ . This value is promising because it is in the range of bulk KNbO<sub>3</sub> crystals [[6],[7],[8],[9]] and can compete with piezoelectric coefficients recorded for Pb(Zr, Ti)O<sub>3</sub> thin films with similar thickness [10]. Therefore, further effort will be spent in optimizing the growth conditions for achieving a comparable ordering of the domains on the bottom electrode to those on the bare substrate.

Regarding the unusual domain wall inclination angle, I performed an intense study of  $\alpha$  as a function of potassium content  $x$  [128] presented in chapter 10.

## 10. Tunable ferroelectric domain wall alignment in monoclinic systems

In regard of charge neutrality, domains have to be formed as twins with equal shape and volume. Hereby, the alignment of domain walls is restricted to the symmetry elements of the crystallographic point group of the material under investigation. Hence, in common ferroelectric materials crystallizing in high symmetric tetragonal or orthorhombic phases, the electrical polarization vector is linked to a crystallographic axis. As a result of this restriction the corresponding domain walls can be tilted against the main crystallographic axes exclusively by angles of  $45^\circ$  or  $90^\circ$  [[111],[129]] although the angle between both adjacent polarization vectors could be different as apparent in rhombohedral systems [[130],[131]]. In contrast, in the low symmetric monoclinic phase, the mirror plane is the primary symmetry element. As a result, for ferroelectric systems with monoclinic symmetry, the domain walls are solely fixed to this mirror plane permitting arbitrary directions to the main crystallographic axes. Consequently, the included angle between both can be almost continuously modified.

Indeed, in a theoretical work, Bokov and Ye [5] showed that domain wall angles in monoclinic lead zirconium titanate may vary in the range of several tens of degree. They basically depend only on the lattice parameters and the monoclinic distortion angle  $\beta$ .

Lattice parameter in  $K_xNa_{1-x}NbO_3$  can easily be varied by changing the composition  $x$  or the underlying substrate. Here, the spatial dimension as well as the shearing angle of the monoclinic unit cell were modified through a variation of the potassium content  $x$  between  $x = 0.80$  to  $0.95$  in the  $K_xNa_{1-x}NbO_3$  thin films on  $NdScO_3$  substrates. The comparatively narrow composition range is based on the requirement of coexisting  $a_1a_2$  and  $M_c$  phases with  $Pm$  symmetry to induce the pronounced herringbone domain pattern. However, despite the small variation in the potassium content  $x$ , the monoclinic distortion angle  $\beta$  and the vertical lattice parameter do change significantly.

The surface morphology of the films was analyzed via atomic force microscopy. The surface topology of all films exhibit rather smooth surfaces with a root mean square roughness well below  $0.5$  nm. The ferroelectric domain structure was investigated with the piezoresponse force microscopy. The lateral piezoresponse images of all samples are shown in fig. 42a-d.

In accordance to the measurements presented before for  $x = 0.90$ , a coexistence of  $a_1a_2$

and  $M_c$  domains is observed which is interlaced to a herringbone pattern. Obviously, the stripe domains do not include an angle of  $45^\circ$  or  $90^\circ$  to the  $[001]_{\text{NSO}}$  directions. In order to quantitatively evaluate the inclination angles,  $\alpha_{\text{PFM}}^{\text{exp}}$ , of the stripe domains, two-dimensional Fourier analysis of the PFM images shown in fig. 42a-d were performed. As one example, the 2D-FFT calculation for the sample with 90% (fig. 42b) is shown in fig. 42f. According to the model from Bokov and Ye [5],  $\alpha$  depends on the

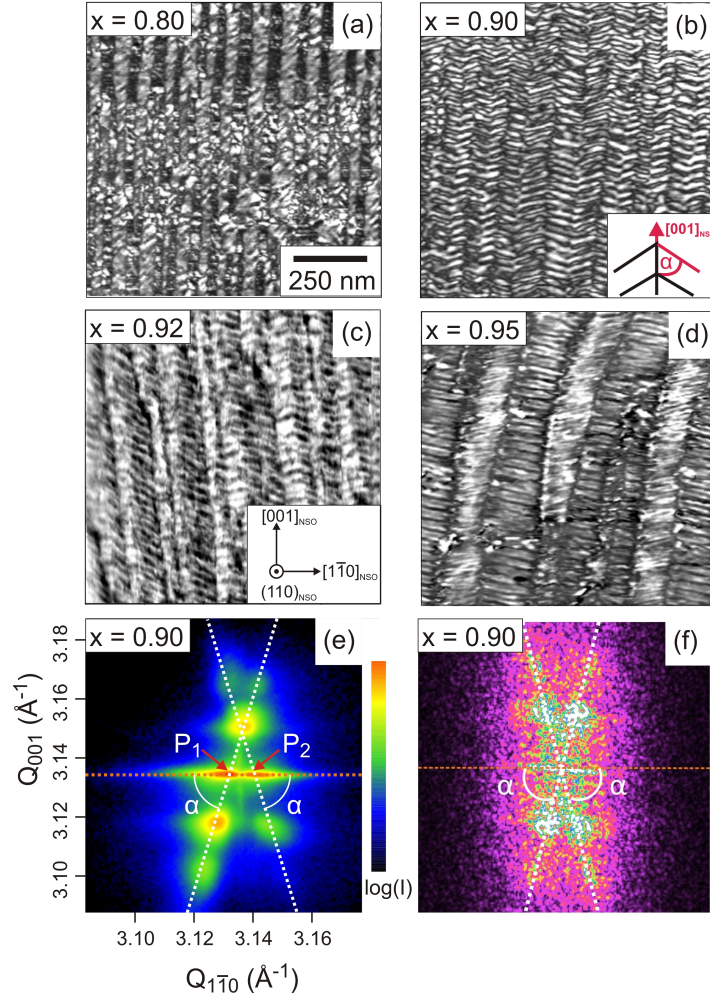


Figure 42: (a)-(d) Lateral piezoresponse force amplitude images ( $(1 \times 1) \mu\text{m}^2$ ) of  $\text{K}_x\text{Na}_{1-x}\text{NbO}_3$  thin films grown on  $\text{NdScO}_3$  orthorhombic substrate with varying potassium concentration  $x$ . Insets in (b) and (c) show the definition of in-plane domain wall inclination angle  $\alpha$  and the orientation of the  $\text{NdScO}_3$  substrate, respectively. (e) Grazing Incidence in-plane x-ray diffraction intensity distribution recorded in the vicinity of the  $(2\bar{2}4)_{\text{NSO}}$  reciprocal lattice point for  $x = 0.90$ . (f) 2D-FFT calculation of the PFM image shown in fig. 42b. Taken from [128].

monoclinic lattice parameters and the distortion angle  $\beta$ . For a better imagination, the monoclinic shearing angle  $\beta$  (exaggerated plotted) and the domain wall inclination

angle  $\alpha$  are sketched in fig. 43. To validate their consideration, the monoclinic lattice

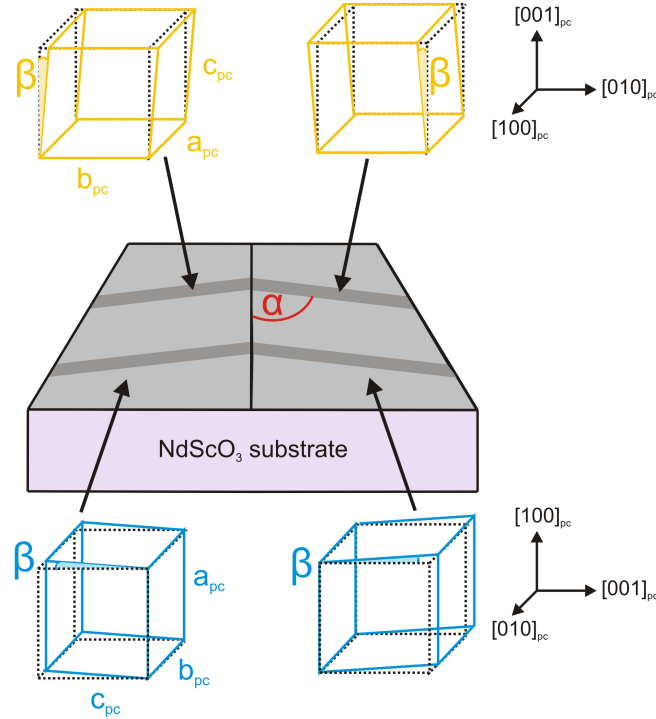


Figure 43: Schematic view of the domain pattern with embedded domain wall inclination angle  $\alpha$  and the respective  $\text{K}_x\text{Na}_{1-x}\text{NbO}_3$  (sheared) pseudocubic unit cells (cross sectional view). The monoclinic  $a_1a_2$  domains with  $(100)_{pc}$  orientation are colored in blue, the  $M_c$  domains with  $(001)_{pc}$  orientation in are depicted with yellow color. The monoclinic distortion angle  $\beta$  is illustrated for both orientations and shearing directions. Taken from [128].

parameters were experimentally determined. As in-plane lattice parameter, the surface lattice parameter of the neodymium scandate substrate are used because the films are grown fully strained.

In order to evaluate the monoclinic in-plane distortion angle  $\beta$ , grazing incidence in-plane x-ray diffraction has been performed. In order to distinguish between strain and morphology related features in reciprocal space a variety of Bragg reflections, e.g.  $(004)_{NSO}$ ,  $(008)_{NSO}$ , and  $(2\bar{2}4)_{NSO}$ , were investigated. Exemplary, the in-plane intensity distributions recorded in the vicinity of the  $(2\bar{2}4)_{NSO}$  reciprocal lattice point is presented in fig. 42e for the potassium content of  $x = 0.90$ . A complicated diffraction pattern evolves. The periodic arrangement of the domain walls leads to two inclined intensity branches (marked by white dashed lines) which are intersected by broad correlation peaks. From the inclination of the two branches the domain wall angle  $\alpha_{GIXD}^{exp}$  is obtained (indicated in fig. 42e-f). Moreover, the separation  $\Delta Q_{1\bar{1}0}$  of the central peaks  $P_1$  and  $P_2$  of the two branches is related to the monoclinic distortion angle  $\beta$

via:

$$\tan \beta = \frac{\Delta Q_{1\bar{1}0}}{2 \cdot Q_{001}} \quad (71)$$

In this way,  $\beta$  has been measured for all four samples depicted in fig. 42a-d. The corresponding  $\beta$  angles are summarized in table 6.

Table 6: Structural parameters of the samples under investigation. The in-plane lattice parameters of the film are equal to the in-plane lattice parameters of the (110) NdScO<sub>3</sub> surface unit cell ( $d_{1\bar{1}0} = 4.0124 \text{ \AA}$  and  $d_{001} = 4.0025 \text{ \AA}$ ).

	sample 1	sample 2	sample 3	sample 4
K atomic concentration x	0.80	0.90	0.92	0.95
Vertical lattice spacing d (Å)	3.969	3.986	3.989	3.992
Monoclinic angle $\beta$ (degrees)	0.145	0.11	0.08	0.077

The experimental domain wall angle obtained from PFM ( $\alpha_{\text{PFM}}^{\text{exp}}$ ) and GIXD ( $\alpha_{\text{GIXD}}^{\text{exp}}$ ) analysis are illustrated in fig. 44 as blue circles and red triangles, respectively, as a function of monoclinic distortion  $\beta$ . The error bars result from the reading accuracy

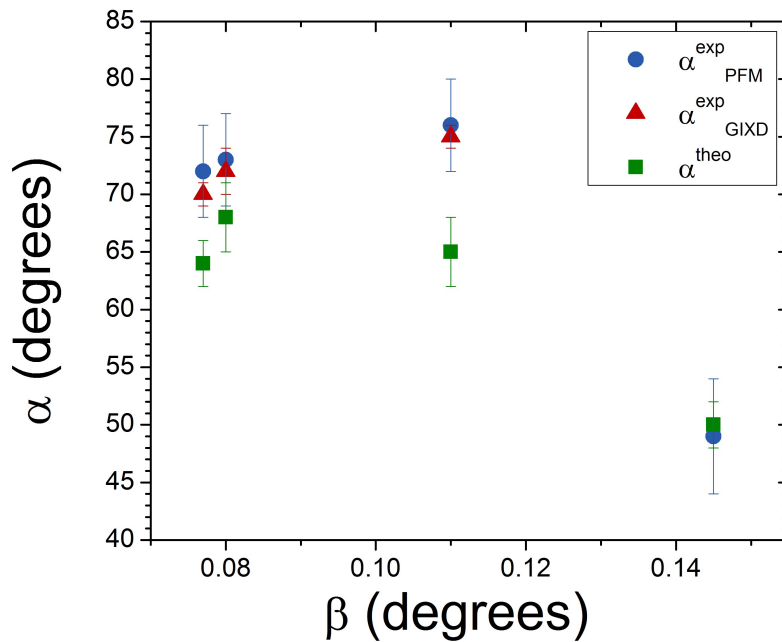


Figure 44: In-plane domain wall inclination angle  $\alpha$  derived from PFM and GIXD along with calculated values as a function of the monoclinic distortion angle  $\beta$  (for details see text). Taken from [128].

in figs. 42e,f. It is striking, that (i) the experimental data evaluated from PFM and GIXD are in excellent agreement and (ii) the domain wall angle is quite sensitive to

the monoclinic distortion of the film unit cell.

The correlation between monoclinic shearing angle  $\beta$  and in-plane domain wall angle  $\alpha$  has been theoretically considered by Fousek et al. [132] for the arrangement of compatible ferroelectric domain walls depending on their respective symmetry and by Sapriel [133] for ferroelastics. The special case of monoclinic symmetry was discussed later by Bokov and Ye [5]. On the basis of these geometrical considerations, compatible monoclinic domain walls can be identified and the resulting domain wall angles  $\alpha$  can be derived for  $Pm$  symmetry.

Thereby, two different domain walls  $S_1$  and  $S_2$  can appear whose plane equations are denoted as follows:

$$S_1 \rightarrow (a - b)(x \pm y) = \pm 2dz \quad (72)$$

$$S_2 \rightarrow (c - a)(x \pm y) = \pm 2dz \quad (73)$$

The difference is a quantitative change of the tilting angle of the domain wall around the  $\langle 001 \rangle_{pc}$  directions. In eq. 72 and 73, the parameter set  $a$ ,  $b$ ,  $c$  and  $d$  denotes the components of the so-called spontaneous strain tensor [134]. These quantities can be expressed by the pseudocubic [49] lattice parameters  $a_{pc}$ ,  $b_{pc}$ ,  $c_{pc}$  and the monoclinic distortion angle  $\beta$  via:

$$a = \frac{b_{pc} - p}{p} \quad (74)$$

$$b = \frac{a_{pc} - p}{p} \quad (75)$$

$$c = \frac{c_{pc} - p}{p} \quad (76)$$

$$2d = \frac{\pi}{2} - \beta \quad (77)$$

$$p = \frac{a_{pc} + b_{pc} + c_{pc}}{3} \quad (78)$$

Furthermore,  $x$ ,  $y$  and  $z$  describe likewise the main crystallographic axes as well as the indices of the planes in the pseudocubic notation. The domain wall angle  $\alpha$  with respect to the  $\langle 001 \rangle_{pc}$  directions can be evaluated as traces of these walls on e.g. the  $x = 0$  planes as described in eqs. 79-80:

$$S_1 \rightarrow \tan \alpha = \frac{a - b}{\pm 2d} \quad (79)$$

$$S_2 \rightarrow \tan \alpha = \frac{c - a}{\pm 2d} \quad (80)$$

As mentioned before for fully strained films, the dimensions of the surface unit cell of the NdScO<sub>3</sub> substrate can be used as in-plane lattice parameters of the film, while the vertical lattice parameters have been determined from  $\theta/2\theta$  high resolution x-ray diffraction scans (see table 6). Introducing these values in eqs. 74-80, the domain wall angles  $\alpha^{\text{theo}}$  were calculated and are displayed in fig. 44 as green squares with error bars given by the experimental uncertainties of  $\beta$  of  $u_\beta = \pm 0.010^\circ$ . Very good agreement between experimental and calculated values are achieved.

The remaining difference should be briefly discussed. In general, the theoretical descriptions [[5],[132]] are based on a single-domain and free-standing crystal. In consequence, no epitaxial, elastic stresses are considered as they apply for the epitaxial, fully strained film discussed in this thesis. Beyond that, Mokry and Fousek [135] calculated the case of elastic stresses resulting from domain wall alignment in the case of more than two ferroelectric/ferroelastic domains. They conclude that in the presence of these "domain quadruplets" the ferroelastic domains prohibit a stress-free coexistence. Indeed, the  $a_1a_2$  and  $M_c$  domains have different monoclinic distortion requiring an elastic relaxation process at the domain walls. As a result, the pure geometric aspects of the models [[5],[132]] do not reflect the experimental conditions and a deviation from the prediction seems reasonable.

In conclusion, the domain wall angle in a herringbone pattern in monoclinic  $K_xNa_{1-x}NbO_3$  thin films can significantly deviate from  $45^\circ$  or  $90^\circ$ . Indeed, it could even be verified that the domain wall alignment is flexible and can be adjusted according to the theoretical model of Bokov and Ye [5]. This emphasizes the outstanding role of monoclinic phases in ferroelectric materials. The symmetry inherent property to tilt the domain walls nearly arbitrarily against main crystallographic axes results in an additional degree of freedom with regard to "domain engineering" and allows for targeted manipulation of the ferroelectric, periodic domain pattern on a nanometer scale.

In order to tune the monoclinic lattice parameter, a second pathway would be to vary the monoclinic distortion  $\beta$  with film thickness [[96],[106]]. Above the critical thickness, the lattice parameters of a fully strained film relaxes to those of an unstrained film crucially influencing the domain pattern. Rather less is known about the thickness dependent evolution of such hierarchical ferroelectric pattern. Therefore a thickness series of  $K_{0.90}Na_{0.10}NbO_3$  on (110) NdScO<sub>3</sub> was deposited and studied in detail for the first time presented in chapter 11 and [136].

## 11. Hierarchy and scaling behavior of herringbone domain patterns in strained $K_{0.90}Na_{0.10}NbO_3$ ferroelectric epitaxial films

For epitaxial layers with thicknesses in the range of a few tens of nanometers, classical scaling theories calculated for laminar domain formations [[137],[138]] predict that the lateral domain widths and film thickness are of the same order of magnitude. In consequence, domain walls represent a significant volume fraction of the film and their contribution to the total piezoelectric response is of particular relevance [[139],[140]]. By contrast, very little is known about the evolution and scaling behavior of multi-rank [[122],[123]] structures with competing, different electric polarization alignments - especially if domains exhibit a monoclinic symmetry. Indeed, the formation of ferroelectric, monoclinic herringbone domain structures is highly interesting for possible technological applications as structuring devices [141] or building energy harvester [142]. However, the impact of film thickness on complex ferroelectric, monoclinic multi-rank arrangements has not been investigated yet in detail. In this context, open questions are, if there exists a hierarchy for the inset of each single ferroelectric domain. Which film thickness provokes what kind of domain formation? These questions are mandatory to answer for a targeted film deposition in nanoscale applications.

With regard to the questions raised above,  $K_{0.90}Na_{0.10}NbO_3$  thin films on a (110)  $NdScO_3$  substrate as discussed in chapter 9 represent an interesting model system. In order to study the thickness dependence of ferroelectric herringbone pattern for the first time, thin films with  $x = 0.90$  were deposited on  $NdScO_3$  in the range of 7 to 52 nm.

In order to directly correlate the electrical and structural properties, PFM and GIXD measurements have been performed.

Generally, the surface topology of all films is comparable to fig. 33a and exhibits rather smooth surfaces with a root mean square roughness well below 0.5 nm.

The piezoresponse force microscopy measurements are shown in fig. 45.

For the 7 nm thin film, the lateral PFM amplitude image (fig. 45a) indicates the onset of ferroelectric domain formation. The pattern reveals randomly distributed domains, which are elongated along  $[001]_{NSO}$  and exhibit a typical width of about 65 nm along  $[1\bar{1}0]_{NSO}$ . However, the vertical PFM image (fig. 45b) does not show any significant contrast variation. This is attributed either to a marginal amplitude contrast

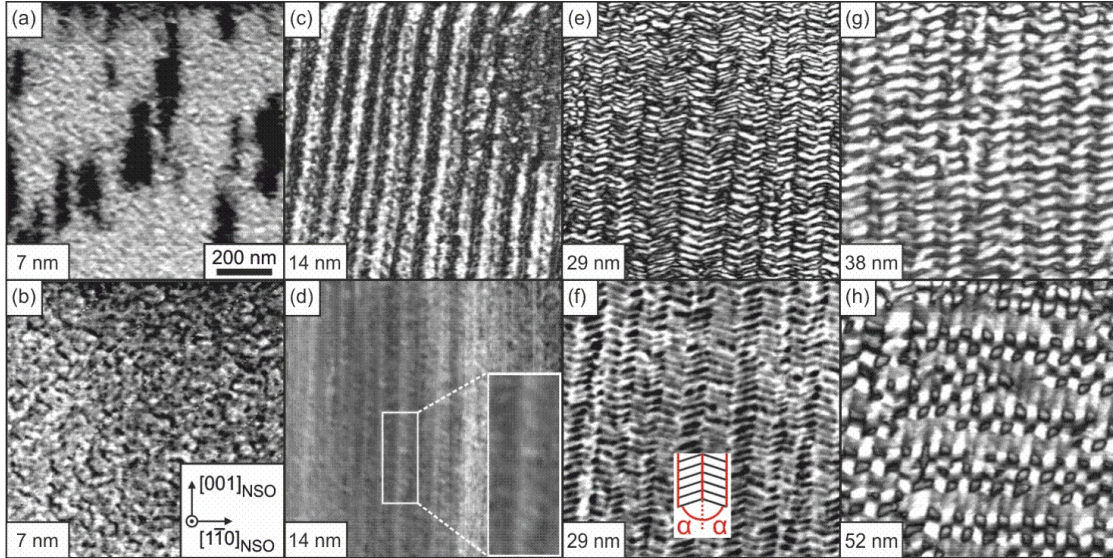


Figure 45: Piezoresponse force amplitude micrographs (PFM) of (a-b) 7 nm, (c-d) 14 nm, (e-f) 29 nm  $\text{K}_{0.90}\text{Na}_{0.10}\text{NbO}_3$  thin films grown on orthorhombic (110)  $\text{NdScO}_3$  substrate in lateral (top) and vertical (bottom) mode. For the (g) 38 nm and (h) 52 nm thin films lateral PFM amplitude measurements are depicted. The measurement area was chosen to  $(1 \times 1) \mu\text{m}^2$ . Taken from [136].

due to lower sensitivity of the vertical mode [143] or even the absence of a vertical polarization component. LPFM phase images (not shown here) indicates that in the dark and bright areas the in-plane component of the electric polarization vector is rotated by  $90^\circ$ . In accordance to the former results on a 29 nm thick film in chapter 9, the conclusion is drawn of exclusively in-plane oriented  $a_1a_2$  domains at very thin film thicknesses. Grazing incidence x-ray diffraction on this sample results in a sharp peak S (fig. 46a), which is caused by the coherently grown  $\text{K}_{0.90}\text{Na}_{0.10}\text{NbO}_3$  film on the underlying  $\text{NdScO}_3$  substrate. It is surrounded by pronounced diffuse scattering, which is presumably caused by fluctuations of the irregular domains sizes and of the (still very small) in-plane monoclinic angles of the  $a_1a_2$  domains.

With increasing thickness (14 nm), the domains form periodic bundles which are aligned along  $[001]_{\text{NSO}}$ , clearly observed in the lateral PFM image (fig. 45c). A detailed analysis of the PFM images indicates, however, that the bundles are regularly disrupted along  $[001]_{\text{NSO}}$  by slanted lines. This can be also detected in the vertical PFM image (fig. 45d). Since the slanted lines show a low amplitude signal in the lateral PFM image but appear in bright color (= large amplitude signal) in the vertical PFM (see magnified inset in fig. 45c) measurement, they are unlikely be caused by a crosstalk effect. Consequently, an experimental artifact can be excluded. Hence, at 14 nm film

thickness, the onset of a second ferroelectric phase can be observed with a strong vertical electrical polarization component. According to the intense study in chapter 9, the bright and dark domains in VPFM can be identified as monoclinic  $M_c$  and  $a_1a_2$  domains, respectively. The occurrence of  $(001)_{pc}$  oriented  $M_c$  domains in 14 nm thick films substantially changes the corresponding GIXD intensity distribution (fig. 46b). The  $a_1a_2$  domains provoke a distinct peak splitting ( $P_1$  and  $P_2$ ) along  $Q_{1\bar{1}0}$ . The corresponding monoclinic distortion angle, which describes the alternate in-plane shearing of the unit cells along the  $[001]_{NSO}$  direction, is determined to  $\beta = 0.075^\circ$ . However, the slanted lines, which is assigned to the onset of  $M_c$  domain formation, do not lead to a detectable signal in the x-ray diffraction data. This can be explained by the very small scattering volume accompanied with the  $M_c$  phase.

When the film thickness is further increased to 29 nm, a pronounced herringbone domain pattern arises in both the lateral (fig. 45e) and vertical (fig. 45f) PFM images. It consists of a highly periodic array of alternating  $a_1a_2/M_c$  domains, where the corresponding domain walls are tilted by an angle  $\pm\alpha$  with respect to the  $[001]_{NSO}$  direction (see inset in fig. 45f). Moreover, the periodic  $a_1a_2/M_c$  domain arrangement is embedded in large bundles which are aligned along  $[001]_{NSO}$  forming a herringbone pattern. These bundles exhibit a uniform width along  $[1\bar{1}0]_{NSO}$ , which has already been indicated in fig. 45c and d for the 14 nm thick film. Grazing incidence x-ray measurements on the same film exhibit an increased peak splitting ( $P_1$  and  $P_2$ ) (fig. 46c) pointing to a larger monoclinic shearing angle. Furthermore, pronounced satellite peaks occur which are aligned in branches inclined by  $\pm\alpha$  with respect to the  $[001]_{NSO}$  direction (see dashed white lines in fig. 46c). These are attributed to the periodic arrangement of the  $a_1a_2/M_c$  domains with corresponding inclined domains walls. Again, a direct scattering signal from the  $M_c$  domains cannot be detected in the x-ray data. The overall amount of the  $M_c$  phase is still too small as to lead to a detectable scattering signal. This behavior is consistent with the sample investigated in chapter 9.

Compared to the 29 nm thick film, the sample with a film thickness of 38 nm does not reveal remarkable modifications of the domain pattern (see the lateral PFM image in fig. 45g). The widths of both  $M_c$  and  $a_1a_2$  domains along  $[001]_{NSO}$  have further increased, however, the relative volume fraction of  $M_c$  domains has been grown. The corresponding characteristic x-ray diffraction pattern with two distinct peaks  $P_1$  and  $P_2$  and the associated satellite branches are maintained (fig. 46d). The intensity of the satellite peaks is increased indicating an increased periodicity of the domain pattern as compared to the 29 nm sample. This is in agreement with the lateral PFM micro-

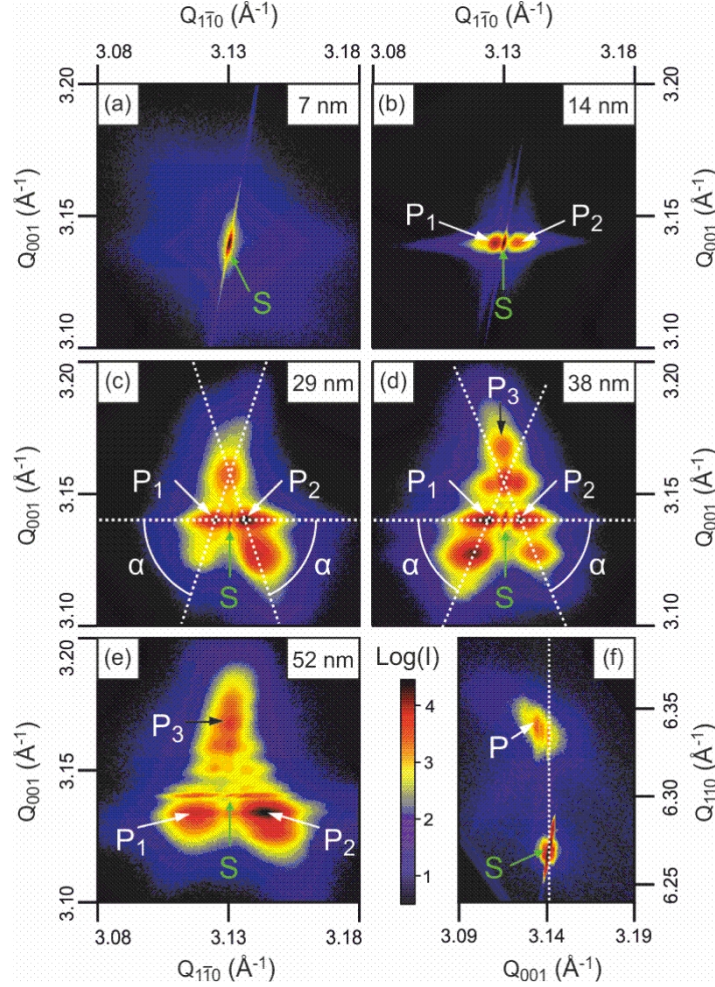


Figure 46: Grazing-incidence in-plane X-ray diffraction (GIXD) intensity distribution in the vicinity of the  $(2\bar{2}4)_{\text{NSO}}$  substrate Bragg reflection for the (a) 7 nm, (b) 14 nm, (c) 29 nm, (d) 38 nm and (e) 52 nm  $\text{K}_{0.90}\text{Na}_{0.10}\text{NbO}_3$  thin films grown on  $(110)$   $\text{NdScO}_3$  (NSO) substrate. (f) Out-of-plane intensity distribution in the vicinity of the  $(444)_{\text{NSO}}$  substrate Bragg reflection for the 52 nm film. Taken from [136].

graphs displayed in fig. 45g (38 nm) and fig. 45e (29 nm). However, importantly, an additional peak (denoted as  $P_3$  in fig. 46d) can be observed.

Increasing the film thickness to 52 nm leads to a further growth of the relative fraction of  $M_c$  domains, hence the widths of  $a_1a_2$  and  $M_c$  domains are approximately of about the same size. However, the overall arrangement of the  $a_1a_2/M_c$  domains has now transformed from a herringbone ( $\alpha < 90^\circ$ ) to a more checkerboard-like pattern (fig. 45h), where the domain walls are tilted by angles  $\alpha$  of about  $\pm 90^\circ$  with respect to the  $[001]_{\text{NSO}}$  direction. This is reflected in the in-plane X-ray pattern, which has changed significantly. The satellite branches initially observed for the 29 nm and 38 nm films have disappeared. Instead,  $P_3$  is now surrounded by satellite peaks, which

form a rectangular grid in reciprocal space in agreement with the transformation from a herringbone to a checkerboard-like pattern with almost rectangular domain walls. Regarding the diffraction pattern of the 52 nm sample, more details can be evaluated: (i) the peak  $P_3$  is even more pronounced (fig. 46e) compared to the intensity measured for the 38 nm film, while its position has not changed. From the experimental position ( $Q_{001}$ ,  $Q_{1\bar{1}0}$ ) of  $P_3$  peak, the horizontal dimensions of the film unit cell can be evaluated to  $d_{001} = (3.9675 \pm 0.0005) \text{ \AA}$  and  $d_{1\bar{1}0} = (4.0135 \pm 0.0005) \text{ \AA}$ . By comparing these film lattice values to (i) the bulk lattice parameter for  $x = 0.90$  calculated in chapter 9 to  $a_{pc} = 3.967 \text{ \AA}$  and  $c_{pc} = 4.029 \text{ \AA}$  and (ii) taking into account that the  $P_3$  peak only occurs for larger  $M_c$  domain widths, we conclude, that the  $P_3$  peak is caused by  $M_c$  domains. They consist of  $(001)_{pc}$  oriented unit cells with the epitaxial relationship  $[100]_{pc} || [001]_{NSO}$  and  $[010]_{pc} || [1\bar{1}0]_{NSO}$ . However, the tensile lattice strain in  $[001]_{NSO}$  of the  $M_c$  unit cells has been relaxed, while they are fully compressively strained in  $[1\bar{1}0]_{NSO}$  direction:

(ii) The peaks  $P_1$  and  $P_2$  provoked by the  $a_1a_2$  phase have slightly shifted to smaller  $Q_{001}$  values while their position with respect to the  $Q_{1\bar{1}0}$  direction remains unchanged (compared to  $Q_{001}$  and  $Q_{1\bar{1}0}$  determined for the thinner films). This can also be observed in the out-of-plane intensity distribution in the vicinity of  $(444)_{NSO}$  (fig. 46f) where the film reflection (P) is shifted to smaller  $Q_{001}$  values as compared to the substrate reflection (S). This proves an increased size of the pseudocubic unit cell along  $[001]_{NSO}$  while it stays fully (compressively) strained along the orthogonal  $[1\bar{1}0]_{NSO}$  direction.

Based on the presented PFM and XRD results several aspects with regard to domain evolution will be discussed now in more detail.

First, I will consider the different domain sizes and hierarchy of domain evolution. The domain widths along the  $[001]_{NSO}$  direction have been evaluated from PFM images as a function of the film thickness (fig. 47a). It is obvious that the widths of  $a_1a_2$  (closed circles) and  $M_c$  (open circles) domains continuously increase with film thickness. A closer look, however, reveals that for comparatively small film thicknesses, a strong asymmetry in the domain widths is observed. The  $M_c$  domains are significantly smaller than the  $a_1a_2$  domains. For the 7 nm film,  $M_c$  domains could not be even observed anymore. However, the  $M_c$  domain widths increase remarkably faster in the studied thickness range than those of the  $a_1a_2$  domains, eventually leading to almost equal sized domains in the 52 nm film. If only elastic strain energy density arguments are considered (for  $K_{0.90}Na_{0.10}NbO_3$  the elastic strain energy density for both  $(001)_{pc}$

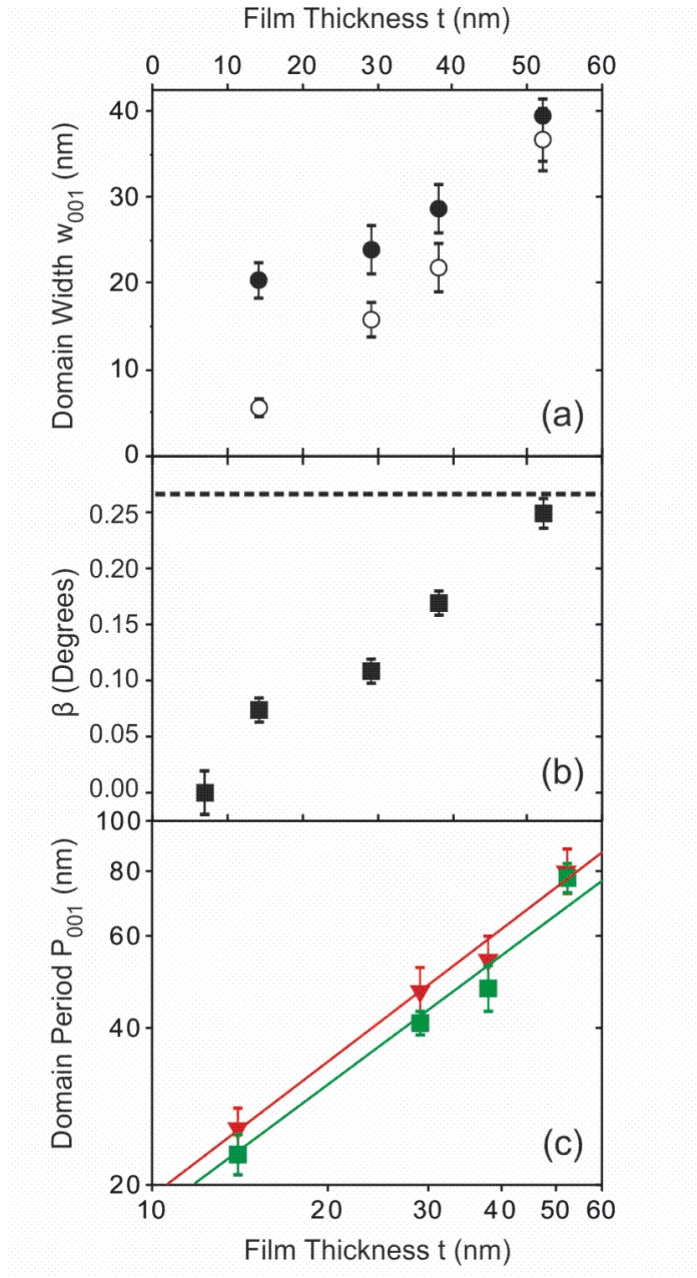


Figure 47: (a) Domain width  $w_{001}$  of the  $a_1a_2$  (black filled circles) and  $M_c$  (black empty circles) domains along the  $[001]_{\text{NSO}}$  direction as a function of film thickness  $t$ . (b) In-plane monoclinic distortion angle  $\beta$  of the  $a_1a_2$  domains. (c) Domain periodicity  $P_{001}$  along the  $[001]_{\text{NSO}}$  direction versus film thickness  $t$  evaluated from PFM (black triangle) and GIXD (black square) measurements. The corresponding solid lines represent best data fits using a power law  $P_{001} \propto t^\nu$  with  $\nu = 0.83 \pm 0.08$  (PFM, red line) and  $\nu = 0.80 \pm 0.10$  (GIXD, green line). Taken from [136].

and  $(100)_{\text{pc}}$  oriented phases is equal [see chapter 9]), the  $(100)_{\text{pc}}$  oriented  $a_1a_2$  and the  $(001)_{\text{pc}}$  oriented  $M_c$  domains should appear with identical probability independent on the film thickness or at least as long as both domains types are fully strained. This is in clear contradiction to the experimental observations, especially for the thinner films. However, additional energy terms may lead to a distinct shift of the energy balance. For example, ferroelastic domains are energetically more favorable than ferroelectric domains owing to the lack of any depolarization field. Indeed,  $M_c$  domains exhibit a strong vertical component of electrical polarization. They would require an increased amount of electric field energy (depolarization field). Therefore, at very small film thicknesses the  $a_1a_2$  domains should appear first, whereas the  $M_c$  domains should be strongly suppressed. This is in agreement with the experimental results obtained for the 7 nm thin film (fig. 45a, fig. 47a).

With increasing film thickness, the epitaxial strain can be effectively reduced by the combined formation of  $a_1a_2$  and  $M_c$  domains. This can be easily understood by the different strain states of both domain types: For  $(100)_{\text{pc}}$  orientation the  $\text{K}_{0.90}\text{Na}_{0.10}\text{NbO}_3$  pseudocubic unit cell is compressively strained, while for  $(001)_{\text{pc}}$  orientation the pseudocubic unit cell is tensely strained on average. Strictly speaking, it is weakly compressively strained along  $[1\bar{1}0]_{\text{NSO}}$  and strongly tensely strained along  $[001]_{\text{NSO}}$ . The coexistence of phases with compressive and tensile strain, however, would enable an efficient reduction of elastic strain energy. This can be achieved via the formation of a domain pattern consisting of both types of surface orientation leading to a herringbone pattern. Furthermore, it has to be noted, that in the thickness range between 14 nm and 38 nm the  $a_1a_2$  domains do not release strain, while the  $M_c$  domains are already fully relaxed at 38 nm in  $[001]_{\text{NSO}}$ . This is the reason, why in this thickness range the overall amount of  $M_c$  domains increases more rapidly with film thickness than the amount of  $a_1a_2$  domains. When both domain sizes have equalized the herringbone pattern transfers to a checkerboard-like pattern in this monoclinic system, which is predicted to be unstable for tetragonal materials [142].

Secondly, the domain period  $P_{001}$  in the direction along  $[001]_{\text{NSO}}$ , i.e., the sum of the individual  $a_1a_2$  and  $M_c$  domain widths, is evaluated from PFM (red triangles) and GIXD (green circles) measurements and presented as function of film thickness in fig. 47a in a double logarithmic scale. The experimental data can be fitted by a power law  $P_{001} \propto t^\nu$  with  $\nu = 0.83 \pm 0.08$  (using PFM data) and  $\nu = 0.80 \pm 0.10$  (using GIXD data). These values agree well but are slightly larger than  $\nu = 0.5$  as predicted in classical scaling theories [[137],[138]]. However, these calculations treat simplified cases,

only. The model by Roitburd [137] describes the scaling of periodic domain structures for limiting cases of very large and very small domains compared to the film thickness. On the other hand, Pertsev and Zembilgotov [138] have treated laminar, tetragonal  $a/c$  or  $a_1/a_2$  domains. These boundary conditions are certainly not applicable to our case of thin films and multi-rank domain arrangements, as e.g. herringbone patterns. A second important point is that these considerations were made for tetragonal and orthorhombic systems. In monoclinic materials, the arrangement of domain walls is much more flexible and is not restricted to highly symmetric crystallographic directions [128].

A third aspect concerns the lattice relaxation. From XRD measurements, it was derived that for the  $M_c$  domains (grown under tensile and compressive lattice in  $[001]_{\text{NSO}}$  and  $[1\bar{1}0]_{\text{NSO}}$  direction, respectively) the strain relaxation process exclusively proceeds along the  $[001]_{\text{NSO}}$  direction while the lattice remains, at least up to a thickness of 52 nm, fully coherent along the  $[1\bar{1}0]_{\text{NSO}}$  direction. These observations are in full qualitative and quantitative agreement with the investigations in chapter 9 where a reduction of the horizontal lattice spacing of the film along  $[001]_{\text{NSO}}$  of about 1% was found. Likewise, in  $a_1a_2$  domains, compressively strained in both in-plane directions, the film lattice has also relaxed in  $[001]_{\text{NSO}}$ , but not in  $[1\bar{1}0]_{\text{NSO}}$  direction valid even for the 52 nm film. This means, for the  $a_1a_2$  and  $M_c$  domains the strain relaxation along the  $[001]_{\text{NSO}}$  direction proceeds in opposite directions: For the compressively strained  $a_1a_2$  domains an increased in-plane lattice parameter (along  $[001]_{\text{NSO}}$ ) is achieved, while for the tensely strained  $M_c$  domains the strain relaxation leads to a reduced in-plane lattice parameter. This, eventually, leads to an effective reduction of strain energy.

On first sight, it is surprising, that the  $a_1a_2$  do not release strain in the thickness regime between 14 nm and 38 nm. However, for monoclinic  $a_1a_2$  domains with  $(100)_{\text{pc}}$  surface orientation an additional elastic strain relaxation mechanism has to be taken into account: For  $(100)_{\text{pc}}$  surface orientation the monoclinic distortion of the pseudocubic unit cell is located in-plane. The corresponding in-plane shearing angle  $\beta$  may continuously increase with increasing film thickness as has been observed for  $\text{NaNbO}_3$  thin films grown on  $(110)$   $\text{TbScO}_3$  [106] and  $(110)$   $\text{DyScO}_3$  [96] substrates. This strain relaxation effect is also observed for our samples. The experimental peak splitting  $\Delta Q_{1\bar{1}0}$  of the thin film reflection is related to the in-plane shear angle  $\beta$  via:

$$\tan(2\beta) = \frac{\Delta Q_{1\bar{1}0}}{Q_{001}} \quad (81)$$

In fig. 47b, the in-plane shear angle  $\beta$  is plotted as a function of the film thickness. It is obvious, that the monoclinic distortion increases monotonically with increasing film thickness indicating elastic strain relaxation. The increase of  $\beta$  leads to an effective reduction of the epitaxial stress induced by the underlying substrate, which exhibits a rectangular surface unit cell. However, this energy gain is exclusively attainable for  $a_1a_2$  domains with  $(100)_{pc}$  surface orientation. By contrast, for  $M_c$  domains with  $(001)_{pc}$  surface orientation the monoclinic shearing arises in a vertical lattice plane. Consequently, for  $M_c$  domains, the epitaxial stress cannot elastically be reduced by a variation of the shearing angle. This suggests that the  $a_1a_2$  domains preferentially release epitaxial strain via enlargement of the in-plane shear angle  $\beta$ , while the  $M_c$  domains have to release epitaxial strain via reduction of the in-plane lattice parameter along  $[001]_{NSO}$ . However, with increasing thickness the in-plane monoclinic shearing of the  $a_1a_2$  domains monotonically increases and, eventually, at a thickness of 52 nm the monoclinic angle of the  $a_1a_2$  domains has reached the bulk value for unstrained  $K_{0.90}Na_{0.10}NbO_3$  of  $\beta_{bulk} = 0.27^\circ$  (fig. 47b). At this point a further reduction of strain energy can be only achieved by an increase of the in-plane lattice parameter (along  $[001]_{NSO}$ ). This is exactly what we observe for the 52 nm film, where the in-plane lattice parameters of the  $a_1a_2$  domains start to relax (fig. 46e,f). A very similar 2-step relaxation process has been observed for a  $a_1a_2$  domains in  $NaNbO_3$  films grown on  $TbScO_3$  [106].

In conclusion, ferroelectric, monoclinic  $K_{0.90}Na_{0.10}NbO_3$  thin films grown epitaxially on  $(110)$   $NdScO_3$  substrates show a thickness dependence of the domain pattern as well as of the lateral size of the individual domains. At comparatively low thicknesses around 14 nm, the domain pattern shows a one-dimensional stripe like symmetry with predominate evolution of  $a_1a_2$  domains. For film thicknesses between 29 and 38 nm a complex, highly regular herringbone pattern consisting of alternating  $a_1a_2/M_c$  monoclinic domains is observed while the relative fraction of  $M_c$  domains is increasing with film thickness. At a thickness of 52 nm, the domain pattern transforms into a checkerboard-like arrangement with equal fractions of  $a_1a_2$  and  $M_c$  domains. The latter is not stable in tetragonal structures [142] proving the unique properties of monoclinic ferroelectric materials. The evolution of the domain pattern with film thickness strongly correlates with strain relaxation inside the film. For the  $a_1a_2$  domains, strain relaxation is achieved by a continuous increase of the in-plane shear angle with film thickness. Plastic strain relaxation starts at about 52 nm film thickness when the in-plane shear angle has reached the bulk value of  $K_{0.90}Na_{0.10}NbO_3$ . For the  $M_c$  domains,

this shear-relaxation mechanism is not accessible and epitaxial strain can be released in this plane exclusively through plastic lattice relaxation. Hence, for  $M_c$  domains, plastic strain relaxation occurs already at lower thicknesses well below 38 nm.

The presented systematic investigation enables to targeted adjust the film thickness in order to provoke one of the stable monoclinic multi-rank arrangements for a specified application.

# Part IV.

## Summary

Within this work a fundamental understanding of the relationship between incorporated lattice strain and ferroelectric phase has been gained for the aim of domain formation in a targeted way known as "domain engineering". The technologically relevant potassium sodium niobate ( $\text{K}_x\text{Na}_{1-x}\text{NbO}_3$ ) was chosen as film material. Although, it has promising piezo - and ferroelectric properties as bulk crystal, this thesis is the first detailed investigation of the thin film form both from a theoretical and experimental point of view.

As a starting point for a fundamental comprehension of strain-phase relations, the formalism to determine the preferred film unit cell orientation of  $\text{K}_x\text{Na}_{1-x}\text{NbO}_3$  under an applied mechanic stress was developed within the framework of the linear elasticity theory. In addition, this calculation was used to determine the resulting vertical strained lattice parameter which can be expected for fully strained films. The value was compared to the experimentally measured lattice parameter to obtain quantitative information about the strain state of the film. For the purpose of domain engineering, I calculated a close meshed misfit strain-misfit strain phase diagram in the framework of the Landau-Ginzburg-Devonshire theory. The result differs from the work of Bai and Ma [3] by significantly more detailed determination of the phase boundaries. Strictly spoken, the strain-phase diagram is valid for pure  $\text{KNbO}_3$ . However, due to the similar properties with  $\text{K}_x\text{Na}_{1-x}\text{NbO}_3$  for  $x \geq 0.5$ , it was successfully applied for this material system as well. On the basis of the misfit strain-phase diagram, targeted  $\text{K}_x\text{Na}_{1-x}\text{NbO}_3$  film compositions were grown epitaxially by liquid-delivery spin metal organic chemical vapor deposition.

As a proof of concept, two examples have been investigated in detail:

- (i) Uniaxial, compressive strain can be achieved when a  $\text{K}_{0.75}\text{Na}_{0.25}\text{NbO}_3$  film is deposited on a (110)  $\text{TbScO}_3$  substrate. The PFM measurements revealed periodic stripe domains running along the  $\pm[1\bar{1}2]_{\text{TbScO}_3}$  direction for several microns. In agreement with the structural data from x-ray measurements, the domain structure was explained as  $M_A$  formation. Moreover, a second  $90^\circ$  rotated variant of such  $M_A$  domains was observed via PFM, however with lower fraction. Indeed, the linear elastic strain energy density reveals only a slight difference for the two

90° rotated (001)<sub>pc</sub> orientations, which explains the occurrence of a preferred domain orientation. Reasons for the deviation from the theoretical prediction of M<sub>c</sub> domains was discussed: (i) too low growth temperature and (ii) deviations of the strain-phase diagram calculated for KNbO<sub>3</sub> to the case of 25% sodium in the reported film.

- (ii)** A point of degenerated strain energy densities for the (100)<sub>pc</sub> - and (001)<sub>pc</sub> orientations can be found according to the linear elasticity theory in K<sub>x</sub>Na<sub>1-x</sub>NbO<sub>3</sub> on (110) NdScO<sub>3</sub> for  $x \approx 0.90$ . The PFM and x-ray measurements depict a herringbone arrangement consisting of monoclinic a<sub>1</sub>a<sub>2</sub>/M<sub>c</sub> domains. The inclination angle  $\alpha$  between the herringbones and the [001]<sub>NSO</sub> direction amounts to  $\alpha = 75^\circ$  which differs significantly from commonly observed angles in materials with tetragonal, orthorhombic or rhombohedral symmetry. In a detailed study, I showed that  $\alpha$  can be systematically adjusted between  $\alpha = 49^\circ - 76^\circ$  with changing the potassium concentration from  $x = 0.80$  to  $0.95$ . This effect is attributed to the monoclinic symmetry and was explained within the model of Bokov and Ye [5]. This flexibility in domain arrangement has not been experimentally observed in thin films yet. Furthermore, the thickness dependent domain evolution evolving for  $x = 0.90$  on (110) NdScO<sub>3</sub> in the range of  $t = 7 - 52$  nm was studied for the first time. Although the elastic strain energy density is degenerated for both pseudocubic orientations, a hierarchy for the onset of each phase was found. The exclusively in-plane oriented a<sub>1</sub>a<sub>2</sub> domains form first, followed by M<sub>c</sub> domains with an inclined electric polarization vector. The reason is the lack of depolarization field energy in the case of pure in-plane domains favoring their prior appearance. In this context, a thickness dependent evolution from stripe domains to a herringbone pattern to a checkerboard-like structure could be observed. This sequence is in contrast to tetragonal systems where the latter is energetically forbidden [142]. Moreover, the domain periodicity P<sub>001</sub> in dependence of the film thickness  $t$  was fitted with  $P_{001} = t^\nu$  and  $\nu = 0.8$  for both the PFM and GIXD data. This exponent deviates from classical models [[137],[138]]. This is attributed to the more complex multi-domain pattern as well as the monoclinicity of the film enabling elastic and plastic lattice relaxation processes. Eventually, PFM measurements on a film with a SrRuO<sub>3</sub> bottom electrode yield a longitudinal piezoelectric coefficient of  $d'_{33} = 29 \frac{\text{pm}}{\text{V}}$ . This value is rather high compared to established ferroelectric materials [[6],[10]].

# Part V.

## Outlook

The described results clearly show a relationship between lattice strain and ferroelectric domain formation. This intense study is novel for  $K_xNa_{1-x}NbO_3$  epitaxial films and represents an important step regarding domain engineering in lead-free materials. However, this is just a first but essential step to grow thin films with adjusted functional properties. On the basis of these fundamental results and theoretical considerations, different approaches for a deeper understanding and/or practical application have been identified.

1. Depositions on  $SrRuO_3$  covered substrates is needed to have a defined potential and determination of macroscopic ferro-/piezoelectric properties.
2. The same strain energy density degeneration of the  $(100)_{pc}$  - and  $(001)_{pc}$  orientation observed in  $K_{0.90}Na_{0.10}NbO_3$  on  $(110) NdScO_3$  can be obtained in  $K_{0.57}Na_{0.43}NbO_3$  on  $SmScO_3$ . But film composition and strain state are different. With  $x$  nearly  $x \approx 0.5$ , a larger longitudinal piezoelectric coefficient  $d'_{33}$  is expected [93]. This may give the chance to enhance  $d'_{33}$ .
3. Rather less is known if the piezoelectric response can be increased with increasing strain. Therefore, a fixed composition could be deposited on various  $SrRuO_3$  covered substrates to study the strain dependent evolution of  $d'_{33}$ .
4. First, preliminary experiments have shown that the stripe domains as discussed for  $K_{0.75}Na_{0.25}NbO_3/TbScO_3$  ( $\varepsilon_{xx} = 0.0003$ ,  $\varepsilon_{yy} = -0.0147$ ) yield a large signal-to-noise ratio and promising Raleigh velocities in surface acoustic waves devices. However, open questions remain as: Do both  $90^\circ$  rotated domain variants lead to different Curie temperatures? Moreover, no fundamental investigation of the Raleigh velocity as a function of strain exists so far. Therefore, can this effect be enhanced in the system  $K_{0.66}Na_{0.34}NbO_3/GdScO_3$  with the same coexistence of both  $(001)_{pc}$  orientation but different strain state ( $\varepsilon_{xx} = 0.003$ ,  $\varepsilon_{yy} = -0.0103$ )?
5. For a more reliable "domain engineering" it would be highly desirable to calculate the misfit strain-misfit strain phase diagram for different sodium concentrations for an unfailing forecast. However, for that purpose, elastic constants of  $K_xNa_{1-x}NbO_3$  have to be determined as function of  $x$ .

## References

- [1] L. Egerton and D. M. Dillon. Piezoelectric and Dielectric Properties of Ceramics in the system Potassium Sodium Niobate. *Journal of the American Ceramic Society*, 42(9):438, 1959.
- [2] Y. Saito, H. Takao, T. Tani, T. Nonoyama, K. Takatori, T. Homma, T. Nagaya, and M. Nakamura. Lead-free piezoceramics. *Nature*, 432(7013):84, 2004.
- [3] G. Bai and W. Ma. Phenomenological analysis of phase transitions in epitaxial perovskite ferroelectric thin films. *Physica B - Condensed Matter*, 405(7):1901, 2010.
- [4] B. Noheda, D. E. Cox, G. Shirane, S. E. Park, L. E. Cross, and Z. Zhong. Polarization rotation via a monoclinic phase in the piezoelectric 92%  $\text{PbZn}_{1/3}\text{Nb}_{2/3}\text{O}_3$ -8%  $\text{PbTiO}_3$ . *Physical Review Letters*, 86(17):3891, 2001.
- [5] A. A. Bokov and Z.-G. Ye. Domain structure in the monoclinic Pm phase of  $\text{Pb}(\text{Mg}_{1/3}\text{Nb}_{2/3})\text{O}_3 - \text{PbTiO}_3$  single crystals. *Journal of Applied Physics*, 95(11, 1):6347, 2004.
- [6] L. Liang, Y. L. Li, S. Y. Hu, L.-Q. Chen, and G.-H. Lu. Piezoelectric anisotropy of a  $\text{KNbO}_3$  single crystal. *Journal of Applied Physics*, 108(9), 2010.
- [7] S. Wada, K. Muraoka, H. Kakemoto, T. Tsurumi, and H. Kumagai. Enhanced piezoelectric properties of potassium niobate single crystals by domain engineering. *Japanese Journal of Applied Physics*, 43(9B):6692, 2004.
- [8] M. Zgonik, R. Schliesser, I. Biaggio, E. Voit, J. Tscherry, and P. Gunter. Materials Constants of  $\text{KNbO}_3$  Relevant for Electrooptics and Acoustooptics. *Journal of Applied Physics*, 74(2):1287, 1993.
- [9] L. Liang, Y. L. Li, L.-Q. Chen, S. Y. Hu, and G.-H. Lu. Thermodynamics and ferroelectric properties of  $\text{KNbO}_3$ . *Journal of Applied Physics*, 106(10), 2009.
- [10] M. G. Cain, M. J. Lowe, A. Cuenat, M. Stewart, and J. Blackburn. volume 2. NSTI-Nanotech, 2005. 671-674, ISBN 0-9767985-1-4.
- [11] N. Setter, D. Damjanovic, L. Eng, G. Fox, S. Gevorgian, S. Hong, A. Kingon, H. Kohlstedt, N. Y. Park, G. B. Stephenson, I. Stolitchnov, A. K. Tagantsev,

- D. V. Taylor, T. Yamada, and S. Streiffer. Ferroelectric thin films: Review of materials, properties, and applications. *Journal of Applied Physics*, 100(5), 2006.
- [12] G. H. Haertling. Ferroelectric ceramics: History and technology. *Journal of the American Ceramic Society*, 82(4):797, 1999.
- [13] R. Ramesh, S. Aggarwal, and O. Auciello. Science and technology of ferroelectric films and heterostructures for non-volatile ferroelectric memories. *Material Science & Engineering R-Reports*, 32(6):191, 2001.
- [14] N. Izyumskaya, Ya. Alivov, S. J. Cho, H. Morkoc, H. Lee, and Y. S. Kang. Processing, structure, properties, and applications of PZT thin films. *Critical Reviews in Solid State and Materials Science*, 32(3-4):111, 2007.
- [15] M. Brazier, S. Mansour, and M. McElfresh. Ferroelectric fatigue of  $\text{Pb}(\text{Zr}, \text{Ti})\text{O}_3$  thin films measured in atmospheres of varying oxygen concentration. *Applied Physics Letters*, 74(26):4032, 1999.
- [16] M. D. Losego and J.-P. Maria. Reproducibility and Ferroelectric Fatigue of Lead Zirconate Titanate Thin Films Deposited Directly on Copper Via a Composite Gel Architecture. *Journal of the American Ceramic Society*, 93(12):3983, 2010.
- [17] E. Aksel and J. L. Jones. Advances in Lead-Free Piezoelectric Materials for Sensors and Actuators. *Sensors*, 10(3):1935, 2010.
- [18] B. Noheda and D. E. Cox. Bridging phases at the morphotropic boundaries of lead oxide solid solutions. *Phase Transitions*, 79(1-2):5, 2006.
- [19] H. X. Fu and R. E. Cohen. Polarization rotation mechanism for ultrahigh electromechanical response in single-crystal piezoelectrics. *Nature*, 403(6767):281, 2000.
- [20] R. Guo, L. E. Cross, S. E. Park, B. Noheda, D. E. Cox, and G. Shirane. Origin of the high piezoelectric response in  $\text{PbZr}_{1-x}\text{Ti}_x\text{O}_3$ . *Physical Review Letters*, 84(23):5423, 2000.
- [21] D. G. Schlom, L.-Q. Chen, C.-B. Eom, K. M. Rabe, S. K. Streiffer, and J.-M. Triscone. Strain tuning of ferroelectric thin films. *Annual Review of Material Research*, 37:589, 2007.

- 
- [22] O. Dieguez, K. M. Rabe, and D. Vanderbilt. First-principles study of epitaxial strain in perovskites. *Physical Review B*, 72(14), 2005.
- [23] Y. L. Li and L. Q. Chen. Temperature-strain phase diagram for BaTiO<sub>3</sub> thin films. *Applied Physics Letters*, 88(7), 2006.
- [24] N. A. Pertsev, A. G. Zembilgotov, and A. K. Tagantsev. Effect of mechanical boundary conditions on phase diagrams of epitaxial ferroelectric thin films. *Physical Review Letters*, 80(9):1988, 1998.
- [25] J. A. Hooton and W. J. Merz. Etch Pattern and Ferroelectric Domains in BaTiO<sub>3</sub> Single Crystals. *Physical Review*, 98(2):409–413, 1955.
- [26] S. N. Zhu and W. W. Cao. Direct observation of ferroelectric domains in LiTaO<sub>3</sub> using environmental scanning electron microscopy. *Physical Review Letters*, 79(13):2558, 1997.
- [27] W. J. Merz. Domain Formation and Domain Wall Motions in Ferroelectric BaTiO<sub>3</sub> Single Crystals. *Physical Review*, 95(3):690, 1954.
- [28] A. Gruverman, O. Auciello, and H. Tokumoto. Scanning force microscopy for the study of domain structure in ferroelectric thin films. *Journal of Vacuum Science & Technology B*, 14(2):602, 1996.
- [29] O. Auciello, A. Gruverman, H. Tokumoto, S. A. Prakash, S. Aggarwal, and R. Ramesh. Nanoscale scanning force imaging of polarization phenomena in ferroelectric thin films. *MRS Bulletin*, 23(1):33, 1998.
- [30] S. V. Kalinin and D. A. Bonnell. Imaging mechanism of piezoresponse force microscopy of ferroelectric surfaces. *Physical Review B*, 65(12), 2002.
- [31] S. V. Kalinin, S. Jesse, B. J. Rodriguez, J. Shin, A. P. Baddorf, H. N. Lee, A. Borisevich, and S. J. Pennycook. Spatial resolution, information limit, and contrast transfer in piezoresponse force microscopy. *Nanotechnology*, 17(14):3400, 2006.
- [32] A. Roelofs, I. Schneller, K. Szot, and R. Waser. Piezoresponse force microscopy of lead-titanate nanograins possibly reaching the limit of ferroelectricity. *Applied Physics Letters*, 81(27):5231, 2002.

- 
- [33] J. Curie and P. Curie. Development, via compression, of electric polarization in hemihedral crystals with inclined faces. *Bulletin De La Societe Mineralogique de France*, 3:90, 1880.
- [34] J. Valasek. Piezo-electric and allied phenomena in rochelle salt. *Physical Review*, 17(7):475, 1921.
- [35] W. Barlow. The symmetry of crystals. The real principle for the 32 classes of symmetry. *Zeitschrift fuer Krystallographie und Mineralogie*, 34(1):1, 1900.
- [36] W. Cao. Constructing Landau-Ginzburg-Devonshire Type Models for Ferroelectric Systems Based on Symmetry. *Ferroelectrics*, 375:28, 2008.
- [37] B. Winchester. *A phase-field investigation of domain structures in ferroelectric bitmuth ferrite thin films*. PhD thesis, The Pennsylvania State University, 2012.
- [38] M. Budimir. *Piezoelectric anisotropy and free energy instability in classic perovskites*. PhD thesis, Ecole Polytechnique Federale de Lausanne, 2006.
- [39] A. Duk. *Relationships between strain, ferro- and piezoelectric properties in functional oxide thin films*. PhD thesis, Humboldt-Universitaet zu Berlin, 2013.
- [40] A. M. Glass and M. E. Lines. *Principles and applications of ferroelectrics and related materials*. Oxford University Press, 1977.
- [41] C. Kittel. Physical Theory of Ferromagnetic Domains. *Review of Modern Physics*, 21(4):541, 1949.
- [42] Z-G. Ye, editor. *Handbook of Advanced Dielectric, Piezoelectric and Ferroelectric Materials*. Woodhead Publishing Limited, 2008.
- [43] J. Sellmann. *Impact of strain and composition on structural and piezo-/ferroelectric properties of epitaxial  $\text{NaNbO}_3$  and  $\text{K}_x\text{Na}_{1-x}\text{NbO}_3$  thin films and superlattices grown by PLD*. PhD thesis, Technische Universitaet Berlin, 2015.
- [44] V. M. Goldschmidt. Die Gesetze der Krystallochemie. *Die Naturwissenschaften*, 1926.
- [45] C. A. Randall, A. S. Bhalla, T. R. ShROUT, and L. E. Cross. Classification and consequences of complex lead perovskite ferroelectrics with regard to B-site cation order. *Journal of Materials Research*, 1990.

- 
- [46] H. G. Hahn. *Elastizitaetstheorie*. Vieweg+Teubner Verlag, 1985.
- [47] I. Haeusler. *Transmissionselektronenmikroskopische Untersuchungen niederdimensionaler Halbleiter zur Charakterisierung von Struktur und chemischer Zusammensetzung*. PhD thesis, Humboldt Universitaet zu Berlin, 2007.
- [48] J. H. Haeni, P. Irvin, W. Chang, R. Uecker, P. Reiche, Y. L. Li, S. Choudhury, W. Tian, M. E. Hawley, B. Craigo, A. K. Tagantsev, X. Q. Pan, S. K. Streiffer, L. Q. Chen, S. W. Kirchoefer, J. Levy, and D. G. Schlom. Room-temperature ferroelectricity in strained SrTiO<sub>3</sub>. *Nature*, 430(7001):758, 2004.
- [49] A. Vailionis, H. Boschker, W. Siemons, E. P. Houwman, D. H. A. Blank, G. Rijnders, and G. Koster. Misfit strain accommodation in epitaxial ABO(3) perovskites: Lattice rotations and lattice modulations. *Physical Review B*, 83(6), 2011.
- [50] M. Schmidbauer, A. Kwasniewski, and J. Schwarzkopf. High-precision absolute lattice parameter determination of SrTiO<sub>3</sub>, DyScO<sub>3</sub> and NdGaO<sub>3</sub> single crystals. *Acta Crystallographica Section B*, 68(1):8, 2012.
- [51] R. Uecker, B. Velickov, D. Klimm, R. Bertram, M. Bernhagen, M. Rabe, M. Albrecht, R. Fornari, and D. G. Schlom. Properties of rare-earth scandate single crystals (Re = Nd-Dy). *Journal of Crystal Growth*, 310(10):2649, 2008.
- [52] G. Shirane, R. Newnham, and R. Pepinsky. Dielectric Properties and Phase Transitions of NaNbO<sub>3</sub> and (Na,K)NbO<sub>3</sub>. *Physical Review*, 96:581, 1954.
- [53] M. Ahtee and A. M. Glazer. Lattice-Parameters and Tilted Octahedra in Sodium-Potassium Niobate Solid-Solution. *Acta Crystallographica Section A*, 32:434, 1976.
- [54] D. Alikin, A. Turygin, A. Kholkin, and V. Shur. Ferroelectric Domain Structure and Local Piezoelectric Properties of Lead-Free(K<sub>0.5</sub>Na<sub>0.5</sub>)NbO<sub>3</sub> and BiFeO<sub>3</sub>-Based Piezoelectric Ceramics. *Materials*, 10(1), 2017.
- [55] H. J. Trodahl, N. Klein, D. Damjanovic, N. Setter, B. Ludbrook, D. Rytz, and M. Kuball. Raman spectroscopy of (K, Na)NbO<sub>3</sub> and (K, Na)<sub>1-x</sub>Li<sub>x</sub>NbO<sub>3</sub>. *Applied Physics Letters*, 93(26), 2008.

- 
- [56] L.-Q. Cheng, K. Wang, J.-F. Li, Y. Liu, and J. Li. Piezoelectricity of lead-free (K,Na)NbO<sub>3</sub> nanoscale single crystals. *Journal of Materials Chemistry C*, 2(43):9091, 2014.
- [57] H. Kimura, H. Zhao, R. Tanahashi, L. Guo, T. Jia, Q. Yao, and Z. Cheng. Potential Advantage of Multiple Alkali Metal Doped KNbO<sub>3</sub> Single Crystals. *Crystals*, 4(3):190, 2014.
- [58] J. Ou-Yang, B. Zhu, Y. Zhang, S. Chen, X. Yang, and W. Wei. New KNN-based lead-free piezoelectric ceramic for high-frequency ultrasound transducer applications. *Applied Physics A*, 118(4):1177, 2015.
- [59] A. A. Esin, D. O. Alikin, A. P. Turygin, A. S. Abramov, J. Hrescak, J. Walker, T. Rojac, A. Bencan, B. Malic, A. L. Kholkin, and V. Ya. Shur. Dielectric relaxation and charged domain walls in (K,Na)NbO<sub>3</sub>-based ferroelectric ceramics. *Journal of Applied Physics*, 121(7), 2017.
- [60] I. Kanno, T. Mino, S. Kuwajima, T. Suzuki, H. Kotera, and K. Wasa. Piezoelectric properties of (K,Na)NbO<sub>3</sub> thin films deposited on (001)SrRuO<sub>3</sub>/Pt/MgO substrates. *IEEE Transactions on ultrasonic ferroelectrics and frequency control*, 54(12):2562, 2007.
- [61] Y. Wakasa, I. Kanno, R. Yokokawa, H. Kotera, K. Shibata, and T. Mishima. Piezoelectric properties of microfabricated (K,Na)NbO<sub>3</sub> thin films. *Sensors and Actuators A*, 171(2):223, 2011.
- [62] K. Shibata, F. Oka, A. Ohishi, T. Mishima, and Kanno. Piezoelectric Properties of (K,Na)NbO<sub>3</sub> Films Deposited by RF Magnetron Sputtering. *Applied Physics Express*, 1(1):011501, 2008.
- [63] T. Li, G. Wang, D. Remiens, and X Dong. Characteristics of highly (001) oriented (K,Na)NbO<sub>3</sub> films grown on LaNiO<sub>3</sub> bottom electrodes by RF magnetron sputtering. *Ceramics International*, 39(2):1359 – 1363, 2013.
- [64] T. Saito, T. Wada, H. Adachi, and I. Kanno. Pulsed Laser Deposition of High-Quality (K,Na)NbO<sub>3</sub> Thin Films on SrTiO<sub>3</sub> Substrate Using High-Density Ceramic Targets. *Japanese Journal of Applied Physics*, 43(9S):6627, 2004.

- 
- [65] N. T. Chua, L. You, J. Ma, and J. Wang. Properties of (K, Na)NbO<sub>3</sub>-based lead-free piezoelectric films prepared by pulsed laser deposition. *Thin Solid Films*, 518(23):6777–6780, 2010.
- [66] F. Lai and J-F. Li. Sol-Gel Processing and Characterization of (Na, K)NbO<sub>3</sub> Lead-Free Ferroelectric Films. *Ferroelectrics*, 358(1):181–187, 2007.
- [67] H. Brunckova, L. Medvecký, P. Hvizdos, and J. Durisin. Structural and nanomechanical properties of sol gel prepared (K, Na)NbO<sub>3</sub> thin films. *Surface and Interface Analysis*, 47(11):1063–1071, 2015.
- [68] J. Schwarzkopf, M. Schmidbauer, T. Remmele, A. Duk, A. Kwasniewski, S. Bin Anooz, A. Devi, and R. Fornari. Strain-induced phase transitions in epitaxial NaNbO<sub>3</sub> thin films grown by metal-organic chemical vapour deposition. *Journal of Applied Crystallography*, 45(5):1015, 2012.
- [69] B. Noheda, D. E. Cox, G. Shirane, J. A. Gonzalo, L. E. Cross, and S. E. Park. A monoclinic ferroelectric phase in the Pb(Zr<sub>1-x</sub>Ti<sub>x</sub>)O<sub>3</sub> solid solution. *Applied Physics Letters*, 74(14):2059, 1999.
- [70] M. H. S. Alrashdan, A. A. Hamzah, and B. Y. Majlis. RF Sputtered PZT Thin Film at MPB for Piezoelectric Harvester Devices. *RSM2015 Proc.*, 2015.
- [71] B. Noheda, J. A. Gonzalo, R. Guo, S.-E. Park, L. E. Cross, D. E. Cox, and G. Shirane. The monoclinic phase in PZT: new light on morphotropic phase boundaries. In *Fundamental Physics of Ferroelectrics*, 2000.
- [72] D. Damjanovic. Contributions to the piezoelectric effect in ferroelectric single crystals and ceramics. *Journal of the American Ceramic Society*, 88(10):2663, 2005.
- [73] M. Davis, M. Budimir, D. Damjanovic, and N. Setter. Rotator and extender ferroelectrics: Importance of the shear coefficient to the piezoelectric properties of domain-engineered crystals and ceramics. *Journal of Applied Physics*, 101(5), 2007.
- [74] B. Noheda, J. A. Gonzalo, L. E. Cross, R. Guo, S. E. Park, D. E. Cox, and G. Shirane. Tetragonal-to-monoclinic phase transition in a ferroelectric perovskite: The structure of PbZr<sub>0.52</sub>Ti<sub>0.48</sub>O<sub>3</sub>. *Physical Review B*, 61(13):8687, 2000.

- 
- [75] D. E. Cox, B. Noheda, G. Shirane, Y. Uesu, K. Fujishiro, and Y. Yamada. Universal phase diagram for high-piezoelectric perovskite systems. *Applied Physics Letters*, 79(3):400, 2001.
- [76] Z.-G. Ye, B. Noheda, M. Dong, D. Cox, and G. Shirane. Monoclinic phase in the relaxor-based piezoelectric/ferroelectric  $\text{Pb}(\text{Mg}_{1/3}\text{Nb}_{2/3})\text{O}_3 - \text{PbTiO}_3$  system. *Physical Review B*, 64(18), 2001.
- [77] M. J. Haun, Z. Q. Zhuang, E. Furman, S. J. Jang, and L. E. Cross. Thermodynamic Theory of the Lead Zirconate-Titanate Solid-Solution System III. *Ferroelectrics*, 99:45, 1989.
- [78] G. Binnig, C. F. Quate, and C. Gerber. Atomic Force Microscope. *Physical Review Letters*, 56(9):930, 1986.
- [79] A. Roelofs A. Gruverman A. Kholkin, S. Kalinin. *Scanning Probe Microscopy: Electrical and Electromechanical Phenomena at the Nanoscale*. Springer Science+Business Media, 2007.
- [80] S. Jesse, A. P. Baddorf, and S. V. Kalinin. Dynamic behaviour in piezoresponse force microscopy. *Nanotechnology*, 17(6):1615, 2006.
- [81] S. Hong, J. Woo, H. Shin, J. U. Jeon, Y. E. Pak, E. L. Colla, N. Setter, E. Kim, and K. No. Principle of ferroelectric domain imaging using atomic force microscope. *Journal of Applied Physics*, 89(2):1377, 2001.
- [82] S. V. Kalinin. *Nanoscale electric phenomena at oxide surfaces and interfaces by scanning probe microscopy*. PhD thesis, 2002.
- [83] B. J. Rodriguez, C. Callahan, S. V. Kalinin, and R. Proksch. Dual-frequency resonance-tracking atomic force microscopy. *Nanotechnology*, 18(47), 2007.
- [84] R. Proksch and S. V. Kalinin. *Piezoresponse force microscopy with asylum research AFMs*. app. note 10.
- [85] R. Garcia and R. Perez. Dynamic atomic force microscopy methods. *Surface Science Reports*, 47(6-8):197, 2002.
- [86] A. Gannepalli, D. G. Yablou, A. H. Tsou, and R. Proksch. Mapping nanoscale elasticity and dissipation using dual frequency contact resonance AFM (vol 22, 355705, 2011). *Nanotechnology*, 24(15), 2013.

- 
- [87] M. J. Higgins, R. Proksch, J. E. Sader, M. Polcik, S. Mc Endoo, J. P. Cleveland, and S. P. Jarvis. Noninvasive determination of optical lever sensitivity in atomic force microscopy. *Review of Scientific Instruments*, 77(1), 2006.
- [88] J. E. Sader, J. A. Sanelli, B. D. Adamson, J. P. Monty, X. Wei, S. A. Crawford, J. R. Friend, I. Marusic, P. Mulvaney, and E. J. Bieske. Spring constant calibration of atomic force microscope cantilevers of arbitrary shape. *Review of Scientific Instruments*, 83(10), 2012.
- [89] R. Proksch and J. Cleveland. *Quantifying Molecular Forces: Sensitivities and Spring Constants without Touching a Surface*.
- [90] M. Schmidbauer. *X-Ray Diffuse Scattering from Self-Organized Mesoscopic Semiconductor Structures*. Springer, 2004.
- [91] C. Feldt. Impact of sodium excess on electric and structural properties of compressively strained  $\text{NaNbO}_3$  thin films. Master's thesis, Technische Universitaet Berlin, 2016.
- [92] A. G. Kalinichev, J. D. Bass, C. S. Zha, P. D. Han, and D. A. Payne. Elastic Properties of Orthorhombic  $\text{KNbO}_3$  Single-Crystals by Brillouin-Scattering. *Journal of Applied Physics*, 74(11):6603, 1993.
- [93] L. Wu, J. L. Zhang, C. L. Wang, and J. C. Li. Influence of compositional ratio  $\text{K}/\text{Na}$  on physical properties in  $(\text{K}_x\text{Na}_{1-x})\text{NbO}_3$  ceramics. *Journal of Applied Physics*, 103(8), 2008.
- [94] G. Steude, B. K. Meyer, A. Goldner, A. Hoffmann, A. Kaschner, F. Bechstedt, H. Amano, and I. Akasaki. Strain modification of GaN in AlGa $\text{N}/\text{GaN}$  epitaxial films. *Japanese Journal of Applied Physics*, 38(5A):498, 1999.
- [95] I. B. Misirlioglu, S. P. Alpay, F. He, and B. O. Wells. Stress induced monoclinic phase in epitaxial  $\text{BaTiO}_3$  on MgO. *Journal of Applied Physics*, 99(10), 2006.
- [96] M. Schmidbauer, J. Sellmann, D. Braun, A. Kwasniewski, A. Duk, and J. Schwarzkopf. Ferroelectric domain structure of  $\text{NaNbO}_3$  epitaxial thin films grown on (110)  $\text{DyScO}_3$  substrates. *Physica Status Solidi - Rapid Research Letters*, 8(6):522, 2014.

- 
- [97] V. G. Koukhar, N. A. Pertsev, and R. Waser. Thermodynamic theory of epitaxial ferroelectric thin films with dense domain structures. *Physical Review B*, 64(21), 2001.
- [98] A. G. Zembilgotov, U. Boettger, and R. Waser. Effect of in-plane shear strain on phase states and dielectric properties of epitaxial ferroelectric thin films. *Journal of Applied Physics*, 104(5), 2008.
- [99] Y. M. Tao and Y. Z. Wu. Effects of anisotropic in-plane strains on the phase diagram of  $\text{Ba}_x\text{Sr}_{1-x}\text{TiO}_3$  thin film. *Journal of Applied Physics*, 101(2), 2007.
- [100] J. Schwarzkopf, D. Braun, M. Hanke, A. Kwasniewski, J. Sellmann, and M. Schmidbauer. Monoclinic  $M_A$  domains in anisotropically strained ferroelectric  $\text{K}_{0.75}\text{Na}_{0.25}\text{NbO}_3$  films on (110)  $\text{TbScO}_3$  grown by MOCVD. *Journal of Applied Crystallography*, 49(2):375, 2016.
- [101] D. Vanderbilt and M. H. Cohen. Monoclinic and triclinic phases in higher-order Devonshire theory. *Physical Review B*, 63(9), 2001.
- [102] L. J. McGilly, A. Schilling, and J. M. Gregg. Domain Bundle Boundaries in Single Crystal  $\text{BaTiO}_3$  Lamellae: Searching for Naturally Forming Dipole Flux-Closure/Quadrupole Chains. *Nano Letters*, 10(10):4200, 2010.
- [103] P. Mokry and T. Sluka. Identification of defect distribution at ferroelectric domain walls from evolution of nonlinear dielectric response during the aging process. *Physical Review B*, 93(6), 2016.
- [104] D. Lee, H. Xu, V. Dierolf, V. Gopalan, and S. R. Phillpot. Shape of ferroelectric domains in  $\text{LiNbO}_3$  and  $\text{LiTaO}_3$  from defect/domain-wall interactions. *Applied Physics Letters*, 98(9), 2011.
- [105] J. Sellmann, J. Schwarzkopf, A. Kwasniewski, M. Schmidbauer, D. Braun, and A. Duk. Strained ferroelectric  $\text{NaNbO}_3$  thin films: Impact of pulsed laser deposition growth conditions on structural properties. *Thin Solid Films*, 570(A):107, 2014.
- [106] A. Duk, M. Schmidbauer, and J. Schwarzkopf. Anisotropic one-dimensional domain pattern in  $\text{NaNbO}_3$  epitaxial thin films grown on (110)  $\text{TbScO}_3$ . *Applied Physics Letters*, 102(9):091903, 2013.

- 
- [107] H. Cao, F. M. Bai, N. G. Wang, J. F. Li, D. Viehland, G. Y. Xu, and G. Shirane. Intermediate ferroelectric orthorhombic and monoclinic  $M_B$  phases in [110] electric-field-cooled  $\text{Pb}(\text{Mg}_{1/3}\text{Nb}_{2/3})\text{O}_3 - 30\%\text{PbTiO}_3$  crystals. *Physical Review B*, 72(6), 2005.
- [108] T. Jungk, Á. Hoffmann, and E. Soergel. *New Insights into Ferroelectric Domain Imaging with Piezoresponse Force Microscopy*, pages 209–228. Springer Berlin Heidelberg, Berlin, Heidelberg, 2009.
- [109] X. Lu, H. Zhang, L. Zheng, and W. Cao. Phase coexistence in ferroelectric solid solutions: Formation of monoclinic phase with enhanced piezoelectricity. *AIP Advances*, 6(10), 2016.
- [110] J. Padilla, W. Zhong, and D. Vanderbilt. First-principles investigation of 180 degrees domain walls in  $\text{BaTiO}_3$ . *Physical Review B*, 53(10):5969, 1996.
- [111] B. Meyer and D. Vanderbilt. Ab initio study of ferroelectric domain walls in  $\text{PbTiO}_3$ . *Physical Review B*, 65(10), 2002.
- [112] S. Choudhury, Y. Li, N. Odagawa, A. Vasudevarao, L. Tian, P. Capek, V. Dierolf, A. N. Morozovska, E. A. Eliseev, S. Kalinin, Y. Cho, L.-Q. Chen, and V. Gopalan. The influence of 180 degrees ferroelectric domain wall width on the threshold field for wall motion. *Journal of Applied Physics*, 104(8), 2008.
- [113] M. Schmidbauer, D. Braun, T. Markurt, M. Hanke, and J. Schwarzkopf. Strain Engineering of Monoclinic Domains in  $\text{K}_x\text{Na}_{1-x}\text{NbO}_3$  Epitaxial Layers: A Pathway to Enhanced Piezoelectric Properties. *Nanotechnology*, 28:24LT02, 2017.
- [114] R. Hosemann. Roentgeninterferenzen an Stoffen mit Fluessigkeitsstatischen Gitterstoerungen. *Zeitschrift fuer Physik*, 128(1):1, 1950.
- [115] A. Roelofs, N. A. Pertsev, R. Waser, F. Schlaphof, L. M. Eng, C. Ganpule, V. Nagarajan, and R. Ramesh. Depolarizing-field-mediated 180 degrees switching in ferroelectric thin films with 90 degrees domains. *Applied Physics Letters*, 80(8):1424, 2002.
- [116] K. Kitamura, Y. Furukawa, K. Niwa, V. Gopalan, and T. E. Mitchell. Crystal growth and low coercive field 180 degrees domain switching characteristics of stoichiometric  $\text{LiTaO}_3$ . *Applied Physics Letters*, 73(21):3073, 1998.
-

- 
- [117] N. Balke, S. Choudhury, S. Jesse, M. Huijben, Y. H. Chu, A. P. Baddorf, L. Q. Chen, R. Ramesh, and S. V. Kalinin. Deterministic control of ferroelastic switching in multiferroic materials. *Nature Technology*, 4(12):868, 2009.
- [118] S. Matzen, O. Nesterov, G. Rispens, J. A. Heuver, M. Biegalski, H. M. Christen, and B. Noheda. Super switching and control of in-plane ferroelectric nanodomains in strained thin films. *Nature Communications*, 5, 2014.
- [119] J. H. Sung, W.-M. Lee, J. H. Lee, K. Chu, D. Lee, X. Moya, N. D. Mathur, C.-H. Yang, J.-H. Park, and M.-H. Jo. Single ferroelectric-domain photovoltaic switch based on lateral BiFeO<sub>3</sub> cells. *NPG Asia Materials*, 5, 2013.
- [120] N. T. Tsou and J. E. Huber. Domain Evolution of Herringbone Structures in Ferroelectric Single Crystals. *Proceedings of the ASME 2010 Conference on Smart Materials, Adaptive Structures and Intelligent Systems*, 1(2):285, 2010.
- [121] N. T. Tsou, J. E. Huber, and A. C. F. Cocks. Evolution of compatible laminate domain structures in ferroelectric single crystals. *Acta Materialia*, 61(2):670, 2013.
- [122] L. A. Schmitt, K. A. Schoenau, R. Theissmann, H. Fuess, H. Kungl, and M. J. Hoffmann. Composition dependence of the domain configuration and size in Pb(Zr<sub>1-x</sub>Ti<sub>x</sub>)O<sub>3</sub> ceramics. *Journal of Applied Physics*, 101(7), 2007.
- [123] T. Asada and Y. Koyama. Ferroelectric domain structures around the morphotropic phase boundary of the piezoelectric material PbZr<sub>1-x</sub>Ti<sub>x</sub>O<sub>3</sub>. *Physical Review B*, 75(21), 2007.
- [124] G. Catalan, A. Lubk, A. H. G. Vlooswijk, E. Snoeck, C. Magen, A. Janssens, G. Rispens, G. Rijnders, D. H. A. Blank, and B. Noheda. Flexoelectric rotation of polarization in ferroelectric thin films. *Nature Materials*, 10(12):963, 2011.
- [125] D. Lee and T. W. Noh. Giant flexoelectric effect through interfacial strain relaxation. *Philosophical Transactions of the Royal Society A - Mathematical, Physical and Engineering Science*, 370(1977):4944, 2012.
- [126] C. M. Wu, W. J. Chen, Yue Zheng, D. C. Ma, B. Wang, J. Y. Liu, and C. H. Woo. Controllability of Vortex Domain Structure in Ferroelectric Nanodot: Fruitful Domain Patterns and Transformation. *Scientific Reports*, 4, 2014.

- 
- [127] R. Xu, S. Liu, I. Grinberg, J. Karthik, A. R. Damodaran, A. M. Rappe, and L. W. Martin. Ferroelectric polarization reversal via successive ferroelastic transitions. *Nature Materials*, 14(1):79, 2015.
- [128] D. Braun, M. Schmidbauer, M. Hanke, A. Kwasniewski, and J. Schwarzkopf. Tunable ferroelectric domain wall alignment in strained monoclinic  $K_xNa_{1-x}NbO_3$  epitaxial films. *Applied Physics Letters*, 110:232903, 2017.
- [129] A. S. Everhardt, S. Matzen, N. Domingo, G. Catalan, and B. Noheda. Ferroelectric Domain Structures in Low-Strain  $BaTiO_3$ . *Advances Electronic Materials*, 2(1), 2016.
- [130] A. Lubk, S. Gemming, and N. A. Spaldin. First-principles study of ferroelectric domain walls in multiferroic bismuth ferrite. *Physical Review B*, 80:104110, 2009.
- [131] P. Marton, I. Rychetsky, and J. Hlinka. Domain walls of ferroelectric  $BaTiO_3$  within the Ginzburg-Landau-Devonshire phenomenological model. *Physical Review B*, 81:144125, 2010.
- [132] J. Fousek and V. Janovec. Orientation of Domain Wall in Twinned Ferroelectric Crystals. *Journal of Applied Physics*, 40(1):135, 1969.
- [133] J. Sapriel. Domain-Wall Orientation in Ferroelastics. *Physical Review B*, 12(11):5128, 1975.
- [134] K. Aizu. Determination of State Parameter and Formulation of Spontaneous Strain for Ferroelastics. *Journal of the Physical Society of Japan*, 28(3):706, 1970.
- [135] P. Mokry and J. Fousek. Elastic aspects of domain quadruplets in ferroics. *Journal of Applied Physics*, 97(11), 2005.
- [136] D. Braun, M. Schmidbauer, M. Hanke, and J. Schwarzkopf. Hierarchy and scaling behaviour of ferroelectric multi-rank domain patterns in strained  $K_{0.9}Na_{0.1}NbO_3$  epitaxial films. *submitted to Nanotechnology*, 2017.
- [137] A. L. Roitburg. Equilibrium Structure of Epitaxial Layers. *Physica Status Solidi A*, 37(1):329, 1976.

- 
- [138] N. A. Pertsev and A. G. Zembilgotov. Energetics and Geometry of 90-Degrees Domain-Structures in Epitaxial Ferroelectric and Ferroelastic Films. *Journal of Applied Physics*, 78(10):6170, 1995.
- [139] N. A. Pertsev and A. Yu. Emelyanov. Domainâ“wall contribution to the piezoelectric response of epitaxial ferroelectric thin films. *Applied Physics Letters*, 71(25):3646, 1997.
- [140] J. E. Garcia, J. D. S. Guerra, E. B. Araujo, and R. Perez. Domain wall contribution to dielectric and piezoelectric responses in  $0.65\text{Pb}(\text{Mg}_{1/3}\text{Nb}_{2/3})0.35\text{PbTiO}_3$  ferroelectric ceramics. *Journal of Physics D: Applied Physics*, 42(11):115421, 2009.
- [141] P. R. Potnis, N.-T. Tsou, and J. E. Huber. A Review of Domain Modelling and Domain Imaging Techniques in Ferroelectric Crystals. *Materials*, 4(2):417, 2011.
- [142] A. R. Balakrishna and J. E. Huber. Nanoscale domain patterns and a concept for an energy harvester. *Smart Materials and Structures*, 25(10), 2016.
- [143] S. V. Kalinin, B. J. Rodriguez, S. Jesse, J. Shin, A. P. Baddorf, P. Gupta, H. Jain, D. B. Williams, and A. Gruverman. Vector piezoresponse force microscopy. *Microscopy and Microanalysis*, 12(3):206, 2006.

# Acknowledgement

Ich möchte Herrn Prof. Dr. Roberto Fornari dafür danken, dass er mich als Doktorandin am Leibniz-Institut für Kristallzüchtung angenommen hat. Im weiteren Verlauf der Arbeit übernahm Herr Prof. Günther Tränkle die Leitung des Institutes und ich danke ihm für diese Tätigkeit und die aufbauenden Worte in der Instituts- und Doktorandenversammlung.

Des Weiteren möchte ich Herrn Prof. Dr.-Ing. Matthias Bickermann meinen Dank aussprechen, dass er diese Doktorarbeit als Hauptgutachter übernommen hat und mir in organisatorischen und rechtlichen Fragen jederzeit zur Seite stand.

Ganz besonders möchte ich mich bei der Gruppenleiterin "Ferroelektrische Oxidschichten" Dr. Jutta Schwarzkopf bedanken. Sie hat mich als meine direkte Betreuerin angeleitet und mich herausgefordert, weiter und anders zu denken. Sie hat unermüdlich an der Interpretation der Ergebnisse mitgewirkt und zahlreiche Texte mit viel Geduld konstruktiv verbessert. Ich danke ihr für alles, was ich in den Jahren lernen durfte.

Ebenso möchte ich PD Dr. Martin Schmidbauer danken für sein Interesse und Durchhaltevermögen, die Kristallstruktur unserer Filme zu verstehen und in Korrelation mit der ferroelektrischen Anordnung zu bringen. Ich danke ihm für die vielen Modelle, die zahlreichen Röntgenmessungen und sein offenes Ohr für Unverstandenes. In diesem Rahmen möchte ich auch PD Dr. Michael Hanke meinen Dank aussprechen für seine beharrliche Unterstützung bei Röntgenmessungen und Perfektionierung von Veröffentlichungen.

Darüber hinaus wäre diese Arbeit nicht möglich gewesen ohne den unermüdlichen Einsatz von Michaela Klann und Sebastian Marksches an der MOCVD-Anlage. Vielen Dank hierbei ebenso an Raimund Grüneberg, der als helfende Hand fortwährend zur Verfügung stand.

Den Start in diese Arbeit hat mir Dr. Andreas Duk sehr erleichtert, indem er mir einen fundierten Einblick ins PFM gegeben hat. Vielen Dank für die exzellente Einführung! Ich möchte mich ebenso bei Prof. Roger Wördenweber bedanken, der sich nicht nur als Gutachter dieser Arbeit bereiterklärt hat, sondern mich mit seinem Optimismus und zahlreichen Ideen für Anwendungen fasziniert hat.

Die gewonnenen Erkenntnisse fußen auf zahlreichen Diskussionen und weiterführenden Messungen. Ich danke Albert Kwasniewski, Christoph Feldt, Jan Sellmann, Philipp Kehne und Leonard von Helden für Röntgenbeugungsmessungen. Zudem möchte ich

meine Dankbarkeit an Philipp Müller, Dr. Toni Markurt und Dr. Martin Albrecht für die Präparation, Durchführung und Interpretation von TEM-Messungen zum Ausdruck bringen.

Die Grundlage dieser Arbeit waren im wahrsten Sinne des Wortes Oxidsubstrate aus der AG "Oxide und Fluoride". Für diese herausragende Arbeit möchte ich mich bei allen Mitgliedern dieser Gruppe bedanken. Besonders seien hier Dr. Reinhard Uecker und Isabelle Schulze-Jonack erwähnt.

Für die elektrischen Messungen unverzichtbar waren leitfähige SrRuO<sub>3</sub>-Schichten von Dr. Arnoud Everhardt von der Universität Groningen. Vielen Dank für die Abscheidung.

Als wichtige Messplätze möchte ich Bessy II in Berlin und die ESRF in Grenoble dankend erwähnen. Vielen Dank für die Möglichkeit, dort zu experimentieren und die vielen helfenden Mitarbeiter, die zu jeder Uhrzeit zur Verfügung standen.

Abschließend möchte ich mich beim Abteilungsleiter Dr. Günter Wagner für seine fröhliche Art, unsere Abteilung und so auch meine Arbeit zu leiten, bedanken.

Grundsätzlich möchte ich allen für die schöne Zeit danken und freue mich, dass es so viel zu lachen gab.

Letztlich wäre ich ohne meine Familie nie so weit gekommen. Ich danke meinem Vater für die Liebe zur Wissenschaft und meiner Mutter für das unerschütterliche Vertrauen, dass ich es so weit schaffen kann. Mein größter Dank gilt meinem Mann Johannes, der jedes Hoch und Tief dieser Arbeit miterleben musste und dennoch nie die Ruhe verloren hat.

# **Selbstständigkeitserklärung**

Hiermit erkläre ich, dass ich die vorliegende Arbeit selbstständig verfasst und nur die angegebene Literatur und Hilfsmittel verwendet habe. Ich habe mich an keiner anderen Universität um einen Doktorgrad beworben und besitze keinen entsprechenden Doktorgrad. Ich habe Kenntnis von der dem Verfahren zugrunde liegenden Promotionsordnung der Fakultät II - Mathematik und Naturwissenschaften der Technischen Universität Berlin.

Berlin, 26. Juni 2017